WEARABLE BIOMEDICAL SENSORS

by

WENYUAN SHI

DISSERTATION

Submitted in partial fulfillment of the requirements

for the degree of Doctor of Philosophy at

The University of Texas at Arlington

May 2019

Arlington, Texas

Supervising Committee:

J.-C Chiao, Supervising Professor
Jonathan Bredow
Wei-Jen Lee
William E. Dillon
Yuan B Peng

ACKNOWLEDGEMENTS

I would like to give my sincere gratitude to my mentor and supervising Professor Dr. Jung-Chih Chiao for the opportunity to work with him and without his unending support and guidance, I would not have achieved this milestone in my research career. I really appreciate his suggestions and guidance throughout my academic career. I am also thankful to him for providing financial assistance during my graduate study. I am very fortunate to have support and access to the iMEMS laboratory's resources and funding to explore various areas of research interests.

I would like to give my thanks to Dr. Jonathan Bredow, Dr. Wei-Jen Lee, Dr. Yuan B Peng, and Dr. William E Dillon for taking interest in my research work and agree to be part of my supervising committee. Thank you very much for your valuable feedback during this period of my research career and helped steered my research in the right direction.

I would like to give my thanks to the Texas Scottish Rite Hospital for Children, especially Dr. Sucato Daniel J MD and Patty Rampsay to teach me about the scoliosis surgery and for their cooperation to allow me to participate in the scoliosis surgery and gather data for my Ph.D. research.

I would like to thank all the engineers at NeoScBio for cooperating with our group to work on a new generation of the wireless IONM (intraoperative neurophysiological monitoring) module.

I would like to thank Tige Kelley who taught me to use different types of equipment in EE Maker Space for sensor fabrication.

I would like to thank the department of EE at the University of Texas at Arlington and its faculty during my academic career. At the school, I have earned a lot of technical knowledge that helped me to be where I am today. A special thanks to all colleges in the iMEMS group. Thank you for your support and kindness you have shown me.

I would like to thank my parents for bringing me to this world, and supporting me to pursue my dreams.

April 22, 2019

TABLE OF CONTENTS

LIST OF ILLUSTRATIONS

Figure Page

LIST OF TABLES

LIST OF ABBREVIATIONS

BP	Blood Pressure
BSN	Body Sensor Networks
CMRR	Common Mode Rejection Ratio
DI	Deionized
ECG	Electrocardiogram;
EDA	Electrodermal Activity
EEG	Electroencephalographic
EIA	Electronics Industry Association
EMG	Electromyography Sensor
EMI	Electromagnetic Interference
FES	Finite Element Simulation
FR	Frequency Response
GPMF	Generalized Poisson Moment Function
GSR	Galvanic Skin Response
IONM	Intraoperative Neuromonitoring
IOT	Internet of Things
ISM	Industrial, Scientific and Medical
LAN	Local Area Network
MCU	Microcontroller Unit
MEMS	Micro-Electro-Mechanic System
MICS	Medical Implant Communications Service
NFC	Near Field Communication
NTSC	National Television System Committee
PAN	Personal Area Network
PCG	Phonocardiogram
PHD	Personal Health Device

PPG	Photoplethysmogram
OSA	Obstructive Sleep Apnea
PCB	Printed Circuit Board
QRS	QRS complex of ECG wave
RF	Radio Frequency
RFID	Radio Frequency Identification
RMSE	Root Mean Square Error
SNR	Signal to Noise Ratio
SpO2	Oxygen Saturation
SRD	Short Range Device
SVF	State-Variable Filter
TcMEP	Transcranial Motor Evoked Potential
TF	Transfer Function
WBAN	Wireless Body Area Networks
WSN	Wireless Sensor Network

ABSTRACT

WEARABLE BIOMEDICAL SENSORS

WENYUAN SHI, Ph.D.

The University of Texas at Arlington, 2019

Supervising Professor(s): Jung-Chih Chiao

Focusing on current major research interests about the wearable biomedical sensors, numerous achievements contributed by researchers and engineers are reviewed in chapter 1. Development and research trends, as well as challenges of the wearable technologies are discussed. In chapter 2, a new double-resonance sensor was presented for monitoring body dehydration with two resonant frequencies. Using the waveguide method and the finite-element simulations, the sensor was designed with optimal parameters. Electromagnetic field distributions, *Q* factors, and sensitivities of the sensor are analyzed. The sensor's equivalent circuit was deduced. The finite-element model and the equivalent circuit model were simulated for identifying various materials by the resonant frequencies. The sensor was experimentally validated by identifying pork humidity. With a wireless body network, this new wearable biomedical sensor can monitor body dehydration, and potentially used for identification of abnormal or cancerous tissues. In chapter 3, implantable biomedical sensors with wireless body area network (WBAN) are presented for Intraoperative Neuromonitoring (IONM). The wireless system was implemented with advantages of small size, low cost, high sample rate, maximum communication range over 10 *m*, battery life over 10 hours, and isolated electromagnetic interference from power lines and surrounding electrical equipment. Because the new WBAN system has a different frequency response from the IONM system used in hospital, a system identification method was used to find the transfer function between the two systems and was used to convert the wireless recordings to the equivalent IONM waveforms. In order to verify the WBAN performance, the muscular action signals from 20 patients were recorded by the WBAN

during scoliosis correction surgeries at the Texas Scottish Rite Hospital for Children. The signals were converted and evaluated by the goodness of fit, Pearson's correlation, and root mean square errors methods. It has been demonstrated that the converted wireless recordings should be fully acceptable by the doctors.

CHAPTER 1

A REVIEW OF WEARABLE BIOMEDICAL SENSORS

1.1 Introduction

Wearable technologies have wide application ranges in medical, sport, and fitness fields [1]. Our lifestyle has been revolutionized by the rapid emerging of wearable technologies. Modern wearable devices have been embedded with sensors, electronics, computer software, and networking capabilities. They can be used to monitor and record human physiological activities as well as health status in real time [2, 3]. Sensors play a critical role in acquiring signals of physical activities while the electronics enable mobility. Utilizing MEMS and Nanotechnologies, miniature sensors can be implemented using advanced low-power electronics to be worn on a person's body or clothes. Modern microcontrollers can implement high accuracy, up to 24-bit resolution, and high speed, up to 2 million samples per second, analog to digital signal conversion, which enable various digital communication protocols with multi-channel interfaces. Sensor signals then can be efficiently managed in real-time operation. With the emerging IOT (Internet of Things) applications and ubiquitous wireless networks, wearable technologies are more easily integrated into daily life. The software also has become more important with digital signal processing technologies to extract vital information for remote monitoring and analysis of one's health status. Cloud computing and big data analysis can further provide the distribution of data about diseases in a large population for analysis.

Modern wearable technologies include wireless communication, energy harvesting, body area networking, and various sensor techniques. In this chapter, current developments are introduced. Then the status of wearable devices, their costs, power consumptions, components, functions, and signal usages are summarized. Various application conditions requiring specific radio-frequency (RF) techniques and standards such as Bluetooth, Wifi, ZigBee and WBAN (Wireless Body Area Networks) are compared. As an alternative to battery power sources, various energy harvesting methods for the wearables are reviewed. Based on published literature,

wearable sensors are classified according to their locations placed on the body, purposes, and developing stages, in section 1.3. The trends and challenges of wearable technology development are discussed in section 1.4. It is quite clear that in the near future more and more biomedical wearable devices will be developed and supported by fast-progressing advances in integrated MEMS, Nano-scale sensors, flexible electronics, miniaturized low-power transducers, energy harvesting integrated circuits (ICs), efficient data processing, and intelligent control with decision-making functions.

1.2 Wearable Devices

A. Developments of Wearable Devices

Compared to the existing self-monitoring systems used in clinical practice, wearable devices can provide more advantages as they do not restrict a person's mobility and daily activities. They are also inconspicuous which provides accessibility, reliability, and accuracy of diagnosis data. Wearable devices can be broadly classified based on their intended applications as (1) wearable consumer electronic devices, which are oriented to entertainment, security, and personal information exchanges; (2) wearable wellness devices, which encompass fitness and wellness tracking; and (3) wearable healthcare devices, which are used for monitoring of specific symptoms and collecting personal physiological signals. The commercially available devices for fitness and wellness tracking include Basis, Nike FuelBand, Withings Pulse, LG LifeBand, Samsung Gear Fit, Garmin VivoFit, Misfit Flash, FitBit, HTC Grip and many others. Almost all of these devices offer functions like step counting, pulse rate, and sleep position monitoring. Some provide calculated blood pressure information. Together with a companion application in a smart-phone, these devices offer flexible, easy and convenient options for the users to track wellness and fitness. These devices adhere to the IEEE 11073 Personal Health Device (PHD) Family of Standards [4]. While the devices targeting wellness provided daily activity tracking, the wearables for health monitoring have more rigorous challenges in acquiring the physiologically relevant signals which are important for the diagnosis of a disease.

Table 1.1 Comparison with the developing levels, cost, power supplies, components, functions, and signal usages.

Level	Cost	Power	Components	Functions	Signal usages
1	Low	Battery	Sensors, Electronics	Alarm and Monitor	Sound and light
2	Medium	Battery	Sensors, Microcontroller, Software	Alarm, Monitor, and record	Sound, light, screen display, record, and analysis
3	High	Battery	Sensors, Microcontroller, Mobile terminals, Software	Alarm, Monitor, record, calculation, edit, and wired communication	Sound, light, display, record, real time share and analysis
4	Higher	Battery	Sensors, Microcontroller, Wireless, Internet network, Cloud Server, Software	Alarm, Monitor, record, digital signal processing, edit, and wireless connectivity	Sound, light, cloud servers, big data, IOT, and cloud computing
5	Highest	Battery-free	MEMS sensors, Nano sensors, ASIC, Energy-harvesting	Intelligent monitor and wireless connectivity	Cloud servers, big data, IOT, and cloud computing

MEMS: Micro-Electro-Mechanic System; ASIC: application-specific integrated circuit; IOT: Internet of things.

Summarized the sensor development history and trends, we proposed five usage levels of wearable devices based on their intended applications and costs from low to high. On level 1, the wearables have the lowest costs, which consist of sensors and electronic devices for only sensing and alarming. An example is the wristwatch type that senses pulse signals and alarms in real time with LED light and sound. On level 2, the wearables have medium costs, which add recording and display functions. The wearables with more functionalities utilize a microprocessor and software controller to process and record signals. On level 3, the wearables have higher costs but communicate with mobile terminals, such as a cell phone, computing tablet or personal computer. Wired and/or wireless communication methods may be implemented for the acquired signals and among other wearable devices. Hence, the sensor signals may be calculated, edited, plotted, recorded, and retransmitted to different nodes for analysis or collection. On level 4, wearable devices have higher costs, which come from more complex functionalities such as wireless communication to a data cloud servers with IOT technologies. In recent years, with advances by battery-free ultra-low power sensors, on level 5, the wearables encompass the characteristics of MEMS sensors, Nano-scale sensing principles, and Nano-watt-class power consumption. These sensing techniques enable battery-free operations with potential power sources by harvesting electromagnetic energy, solar energy, temperature-gradient thermal

energy, vibration energy, and acoustic energy. The big data and cloud computing techniques can be applied to process the signals collected from large population groups. The classes are summarized in Table 1.1.

B. Wireless Protocols

There are a few wireless protocols in practical applications. Most of the devices implement Bluetooth, WiFi, ZigBee, and WBAN (wireless body area network). They are mainly considered according to the operating frequency, bandwidth and data rates, as shown in Table 1.2. For example, the Bluetooth 4.0 operating at 2.4 – 2.485 GHz has a maximum bit rate of 24 Mbps while WiFi Direct provides up to 250 Mbps [5].

The multitude of sensors embedded in the compact, low power, and wireless devices have led the international WBAN standard as IEEE 802.15.6 [5], which refers to the interconnecting devices used in close proximity around the body [6]. Some also refer to WBAN as body area networks (BAN) or body sensor networks (BSN) [7]. The development is driven by wearable sensing technologies and personal area networking technologies so it is expected to evolve quickly with time. With increasing applications, vast amounts of health data will require WBAN to support real-time reporting, decision making, and potentially therapeutic treatment. It will be also possible that specialized WBAN nodes are ingested or implanted inside the human

Table 1.2 Summary of Bluetooth, WiFi, ZigBee, and WBAN.

Technology	Standards	Type	Frequency	Data rate	Range	Transmitter power	Power Consumption	Cost
WiFi	IEEE 802.11 b/g/n	LAN	2.4 GHz 5 GHz	11 Mbps - 250 Mbps	120m - 250m	High	High	High
Bluetooth	IEEE 802.15.1	PAN	2.4 GHz	3 Mbps - 24Mbps	class 1: 100m class 2: 10m class 3: 1m	Low	Low	Low
ZigBee	IEEE 802.15.4	PAN	868 MHz 915 MHz 2.4 GHz	40kbps - 250 kbps	75m	Low	Low	Low
WBAN	IEEE 802.15.6	BAN	402MHz - 4GHz	57.5kbps - 85.7kbps	10m	Lowest	Lowest	Low

LAN: Local area network; PAN: Personal area network; BAN: Body area network; WBAN: Wireless body area network [5]

body [7]. Thus the integration and relevant standards of wearable and implantable devices around and across body tissues will be important for advanced applications.

Commercially WBAN devices have found success owing to the increasing interest and functionality needs. Currently available devices can sense, monitor, and report blood pressures, heart rates, blood oxygenation levels, exercise intensity, calories burnt, step counts, cadences and more. They offer ubiquitous and, more importantly, unmindful monitoring. For example, it has been shown that blood pressure can be elevated in patients in the presence of medical personnel or in a clinical environment [8]. Continuous and unhindered monitoring through wireless communication becomes attractive for those patients and for who want to maintain a regular lifestyle without restriction. The same advantages can be readily applied in senior care facilities, rehabilitation, diagnosis and therapy [2, 9, 10].

Advantages and disadvantages of these popular wireless technologies are listed in Table 1.2. Working ranges of wireless devices are dependent on transmitter power levels, receiver sensitivity, antenna size, local environment characteristics, and so on. Five examples of the commercial device from Texas Instruments, Inc. for each different wireless technology are summarized in Table 1.3 to illustrate such comparison in transmission speed and power, receiver sensitivity, power consumption, and chip costs.

Table 1.3 Examples: specifications of five wireless devices.

Device Name	Technology	Standards	Transmission speed	Transmitter power	Receiver Sensitivity	Power Consumption	Chip Cost
CC3200 [11] Wireless MCU	WiFi	IEEE 802.11 b/g/n	54Mbps	+14.5 dBm	–74dBm	229 mA	$8
CC2640 [12] Wireless MCU	Bluetooth	IEEE 802.15.1	1 Mbps	+5 dBm	–97 dBm	9.1 mA	$2.5
CC2630 [13] Wireless MCU	ZigBee	IEEE 802.15.4	250 kbps	+5 dBm	–100 dBm	9.1 mA	$2.5
CC2500 [14] RF Transceiver	Low-power wireless	2.4 GHz ISM/SRD	500 kbps	+1 dBm	-104 dBm	21.5 mA	$1.5
CC1101 [15] RF Transceiver	Low-power wireless	433/868/915 MHz ISM/SRD bands	500 kbps	+11 dBm	-116 dBm	33.4 mA	$1.9

MCU: Microcontroller unit; ISM: Industrial, Scientific and Medical; SRD: Short Range Device.

C. Energy Harvesting

Table 1.4 Methods of wearable energy harvesting.

Source	Device	Author (First)	Years	Harvester parameters	Description	Generated power
Kinetic energy from human hand motion	Electromagnetic induction converter for kinetic energy to electrical energy	Samad, F.A. [19]	2016	Coil: 1000 turns Long: 210 mm Diameter: 15mm Weight 140g	A curved wearable electromagnetic harvester on the human hand while walking or running	5.185 mW
Kinetic energy from bending the finger Joints	piezoelectric transducers PIC252	Pasquale, G.De. [20]	2016	61mm× 35 mm ×0.4mm	A glove harvest the power generated by bending the finger joints	31.9 μW
Kinetic energy from foot strikes on the ground	Gear driving generator	Xie, L. [21]	2015	80 mm× 47 mm ×22 mm, 137 g	An in-shoe energy harvester	1 W
Kinetic energy from body motion	Generator of triboelectric effect and electrostatic effect	Cui, N. [22]	2015	2.1 cm×28 cm×0.045 mm	A wearable triboelectric generator made of nylon and Dacron fabric	0.1W
Thermoelectric energy from body heat	Thermal semiconductor and piezoelectric film	Misra, V. [23]	2015	1 cm ×1 cm	Wearable nanostructured energy harvesters for body heat and body motion harvesting	500 μW
Thermoelectric energy from body heat	256 thermocouples from Thermix	Leonov, V. [24]	2013	3×3×3 cm	Thermoelectric energy harvester in a shirt	5mW
Acoustic Energy	Triboelectric nanogenerator	Fan, X. [25]	2015	Custom design size	A nanogenerator of harvesting sound wave energy	121 mW/m^2
Electromagnetic energy from radio frequency	E-fielddipole antenna, H-field helical coilantenna	Bito, J. [26]	2015	E-fieldantenna: dipole 150mm×5mm H-field antenna: four loops 77.6×40mm	Wearable radio-frequency energy harvesters for two-way talk radios	E-field 43.2mW H-field 146.9mW
Electromagnetic energy from 2.4GHz Wi-Fi	Inverted F antenna	Talla, V. [27]	2015	25.7 mm x 7.5 mm	A wearable temperature sensor, which harvests energy from Wi-Fi transmissions and transmits data back to an access point.	2.5 μW
Electromagnetic energy from NFC	Coil on finger ring	Gummeson J. [28]	2014	Coil 10 turns Diameter 1.5 cm	A wearable ring to harvest energy from a NFC-enabled phone	18 mW
Electromagnetic energy from mobile phone	Printed dipole antenna	Visser, H. J. [29]	2008	50×50 mm	A single GSM telephone delivers energy for wirelessly applications	1.9mW
Electromagnetic energy from RFID	Rectifying antenna	Monti, G. [30]	2012	Layout of the antenna is 101.8×99.6 mm	Uses a receiving antenna and a voltage multiplier rectifier	43 μW/cm2
Light and Thermoelectric energy from body heat	16 photovoltaic (PV) cells, 12 thermoelectric Generators (TEG)	Brogan Q. [31]	2014	Each PV cell is 31×31×3.0 mm	A wearable energy harvesting jacket, which harvests energy from solar and body heat	PV: 500 mW TEG: 1.25μW

Low-power sensors and application-specific integrated circuit (ASIC) chips have reduced the battery capacity requirement and enable energy harvesting from additional power sources to operate the devices [16]. The energy harvesting techniques can provide a perpetual operation for wearable devices [17]. Without batteries, the cost, size, and weight of the devices may be reduced. When the devices are implanted inside the body, the troubles of depleted battery replacement will be exempted with the right energy harvesting methods. Some electrical wastes such as dead batteries can be avoided [18]. A common drawback is that the current energy harvesting can only produce a limited amount of energy [18]. It is possible that the energy harvesting techniques will be applied to the next-generation wearable devices for medical monitoring with safety operations.

Up-to-date information about recent energy harvesting methods for kinetic energy, acoustic energy, electromagnetic energy, and light energy is summarized in Table 1.4.

1.3 Wearable Biomedical Sensors

Many wearable sensors for medical diagnosis have been reported and some of them are used in clinical applications. From the application points of view, the devices can be classified based on their developing stages, purposes, sensing modalities, and uses on the body. For a technical point of view, they can be categorized by their communication methods, frequency bands, network types, and power sources.

Table 1.5 summaries the development of such biomedical sensors according to the placement location on the body, which often is determined by the clinical needs. Because of the practical concerns in long-term wearability, the locations are typically on chest, wrist, finger, hand, arm, waist, head, ear, eye, neck, leg, foot, and skin. Implants are also included in the table. The implant location often is directly related to a specific organ or tissues. The purposes are classified as number 1 for fitness, 2 for physiological parameter monitoring, 3 for monitoring senior care, 4 for monitoring children, 5 for applications of a specific disease. The stage of development is classified as number 1 for the research stage, 2 for the prototype stage, and 3 for commercial product stage. With respect to the device networking capability, they are classified as numbers: 1

for wireless point-to-point communication between specific devices, such as ZigBee; 2 for wireless point-to-point communication to a common device that can act as a gateway, such as a smartphone; 3 for wireless WiFi or Bluetooth connection to any device including gateway routers; 4 for wired communication only; and 5 for without communication capability.

1). *Sensors placed on chest*

Wireless and wired communication devices have been placed on the chest to measure and transmit ECG (or EKG, electrocardiogram) signals by wet electrodes [34-36, 38-51, 59-60, 63-66], dry electrodes [33], and capacitive sensors [41, 57]. Advantages of the dry sensors are inexpensive, comfort, and less skin irritation. The weakness of the dry sensor is the ECG signal with higher noise while moving [33]. The wireless communication has also be used to record heart sounds by microphones [52, 54], to measure surface temperatures by thermometers [45, 49, 50, 56, 59, 61], and to measure dielectric permittivities by the bio-impedance sensors [43]. Respiration is monitored by Doppler radar [54], accelerometer [43, 47, 50], and inductive sensor [37]. It can also be monitored with strain signals by piezoelectric sensors [55, 59] and knitted conductive yarns [32]. These sensors can be readily integrated with wireless communication. When the devices are placed on the chest, the physiological signals, such as ECG, heart sound, respiration, cardiovascular, body surface temperatures, and dielectric permittivities, can be directly detected with a higher signal to noise ratio (SNR). However, the devices attached on the chest may limit the body motion and cause inconvenience and discomfort for the patient during long-term monitoring.

Table 1.5. Description of various sensors

Sensor location	Purpose	Develop stage	Author (First)	Year	Communication method	Frequency band	Sensors or device	System description	Power source	Network
Chest	2	2	Patron D. [32]	2016	RFID	870–915 MHz	Knitted strain sensor	Baby breathing monitoring	RFID	1
Chest	2	2	Yokus M. A. [33]	2016	Wired	Sample rate 1000 Hz	ECG dry electrodes	Body surface biopotential Recording	Wired power	4
Chest	2	2	Pani D. [34]	2016	Wired USB	Sample rate 512 Hz	ECG sensor	Textile electrodes for wearable ECG monitoring	Wired power	4
Chest ear	2	2	Da He D. [35]	2015	Wireless		ECG sensor	58 nW ECG ASIC wearable cardiovascular monitoring	0.7 mAh Battery	1
Chest	2	2	Izumi S. [36]	2015	NFC tag IC		ECG and acceleration sensor	Low-power ECG processor for wearable healthcare system	Battery	1
Chest	2	2	Ojarand J. [37]	2015	Wi-Fi	2.4GHz	LDC1000 sensor	Respiration monitoring	Battery	1
Chest	2	3	Zhang X. [38]	2014	WBSN wireless		ECG sensor	Real-Time QRS detection of wearable ECG sensors	Battery	1
Chest	2	2	Thotahewa K.M. [39]	2014	ISM wireless	433MHz	ECG sensor	Low-Power Dual-Band Wireless WBAN applications	Battery	1
Chest	2	2	Ieong C. [40]	2012	TI CC2500 wireless	4kbps	ECG sensor	Wavelet transform for wireless ECG	Battery	1
Chest	2	2	Nemati E. [41]	2012	ANT AP2 RF trans-ceiver	307kbps at 2.4GHz	Capacitive ECG sensor	Long-term wireless wearable ECG sensor on T-shirt	Battery	1
Chest	2	3	Dilmaghani R. S. [42]	2011	eZ430-RF2500	250kbps at 2.4GHz	ECG sensor	WSN monitoring multiple patients using cc2500 chip	Battery	1
Chest	2	2	Vuorela T. [43]	2010	USB	Sample rate at 512 Hz	ECG, bioimpedance, acceleration sensor	Portable physiological signal recorder	Battery	1
Chest	2	2	Jin Z. [44]	2009	Blue-tooth	2.4GHz	ECG sensor	Cardiovascular disease prevention	Battery	3
Chest	2	3	Chen S. [45]	2009	WBAN wireless	1Mbps at 2.4 GHz	ECG and temperature sensor	Low-Power WBSN for biometrics and healthcare	Battery	1
Chest head wrist finger	2	2	Monton E. [46]	2008	CC2420 ZigBee	250kbps at 2.4GHz	ECG, EEG, EOG, and EMG sensor	BAN patient monitoring	Battery	1

Table 1.5. (continues) Description of various sensors

Sensor location	Purpose	Develop stage	Author (First)	Year	Communication method	Frequency band	Sensors or device	System description	Power source	Network
Chest	2	2	Di Rienzo M. [47]	2007	Bluetooth	2.4GHz	Textile ECG electrodes, accelerometer	'MagIC' vest for measuring ECG, respiratory, and movement	Battery	3
Chest	2	2	Pawar T. [48]	2007	Wired	N/A	ECG sensor	Body activity recognition	Wired power	4
Chest, arm, leg	2	2	Chien J. C. [49]	2005	Bluetooth	115.2 kbps at 2.4GHz	ECG, PCG, and temperature sensor	ECG, PCG, and body temperature measurements	Battery	3
Chest, wrist	2	2	Knight F. [50]	2005	Wired	N/A	ECG sensor, accelerometer, and temperature sensor	'SensVest'	Battery	4
Chest, head, wrist, shoe	2	2	Jovanov E. [51]	2003	Wireless	33.6 kbps at 900MHz	EEG, ECG, breathing, GSR, and movement sensor	Wireless intelligent sensors for distributed stress monitoring	Battery	3
Chest	2	2	Sa-ngasoongsong A. [52]	2010	CC2420 Zigbee	250 kbps at 2.4GHZ	Microphone	Wireless stethoscope and phonocardiology	Battery	1
Chest	2	3	Mandal S. [53]	2010	Wireless	N/A	Microphones	Battery-free tag for heart monitoring based on body sensor networks	Wireless power	1
Chest	2	3	Lu G. [54]	2010	Wired	N/A	Doppler radar	Heart rate monitoring	Wired power	4
Chest	2	2	Lanatà A. [55]	2010	Wireless	1Mbps	Multimodal piezoelectric sensor	Wearable system for monitor breathing signal and heart-rate	Battery	1
Chest	2	3	Popovic Z. [56]	2014	Wireless		Microwave thermometer	Wireless thermometers	Battery	1
Chest	2	3	Zheng Y. L. [57]	2014	Wireless		PPG and capacitive wearable sensors	Unobtrusive wearable sensors		3
Chest	2	2	Salman S. [58]	2014	Bluetooth ZigBee	2.4 GHz	Electrode sensor	Monitor lung's dielectric permittivity in non-invasive	Battery	3
Chest, arm, wrist, neck, waist, shoe	2	2	Curone D. [59]	2010	ZigBee WiFi	2.4GHz	ECG, temperature, heat flux, CO2,accelerometer, piezoelectric, and SPO2 ensor	'ProeTEX' smart garment	Battery	3

Table 1.5. (continues) Description of various sensors

Sensor location	Purpose	Develop stage	Author (First)	Year	Communication method	Frequency band	Sensors or device	System description	Power source	Network
Chest, arm	2	3	Xiao S. [60]	2009	CC2420 ZigBee	250 kbps at 2.4GHz	ECG, Heartbeat, pH, glucose, mobility, and walking sensor	'MicaZ' mote based system	Battery	1
Chest	1	2	Gaura E. I. [61]	2009	Blue-tooth	2.4GHz	Accelerometer and temperature sensor	BSN based skin temperature monitor for bomb disposal	Battery	3
Chest	2	2	Luprano J. [62]	2006	Wireless		Accelerometer, temperature, and strain sensor	Mermoth clothes	Battery	1
Chest	2	3	Labati R. D. [63]	2014	Wired	N/A	ECG sensor	ECG Biometric recognition	Wired power	4
Chest	2	3	Safie S. [64]	2013	Wired	N/A	ECG sensor	biometric authentication	Wired power	4
Chest	2	3	Kaul A. [65]	2012	Wired	N/A	ECG sensor	ECG authentication	Wired power	4
Chest	2	3	Coutinho D. P. [66]	2011	Wired	N/A	ECG sensor	ECG Authentication	Wired power	4
Wrist, head	1	2	Abbasi-Kesbi R. [67]	2017	Wireless	2.45 GHz	MEMS gyroscope	Estimate human reaction time	Battery	1
Wrist	2	2	Shi W.Y. [68]	2016	Blue-tooth	2.4 GHz	Microphone	Heart Sound Monitor	Battery	3
Wrist	2	2	Motoyama H. [69]	2016	Wired	20–500 Hz	EMG sensor	Wearable EMG sensors to estimate joint angles of wrist	Battery	1
Wrist, finger	2	1	Mukhopad hyay S. [2]	2015	ZigBee, Blue-tooth WiFi, WiMax	500kbps - 75Mbps, at 2.3-5GHz	Temperature, heart-rate, accelerometer, ECG sensors	Human Activity Monitor	Battery	3
Wrist, finger	1	2	Friedman N. [70]	2014	Micro-USB		magnetometers	measuring wrist & finger rotary	Battery	1
Wrist	2	2	An Y. J. [71]	2014	Wireless	2.4 GHz	Radio Frequency sensor	Wrist Pulse Detection	Battery	1
Wrist	2	2	Pang G. [72]	2014	Wireless		Pulse oximeter	Wrist LEDs Pulse Oximeter	Battery	3
Wrist	1	2	Texas Instrument s [73]	2009	Wireless	433/868 /915 MHz	Accelerometer, pressure, and temperature sensor	A integrated wearable wireless sport watch	Battery	1

Table 1.5. (continues) Description of various sensors

Sensor location	Purpose	Develop stage	Author (First)	Year	Communication method	Frequency band	Sensors or device	System description	Power source	Network
Wrist, finger	2	2	Guo D. G. [74]	2009	ZigBee	250kbps at 2.4GHz	ECG and SpO2 sensor	BSN based system	Battery	1
Wrist chest	2	2	Volmer A. [75]	2008	Zigbee	250kbps at 2.4GHz	ECG, PCG, and PPG sensor	WBSN for vital sign	Battery	1
Wrist chest	2	2	Chung W. Y. [76]	2008	ZigBee	250kbps at 2.4GHz	ECG and blood pressure sensor	A u-healthcare system	Battery	1
Wrist finger	2	2	Buford, R. J. [77]	2008	Wired	Wired	Microwave sensor	Noninvasive measurement of blood glucose levels	Wired power	4
Wrist	2	3	Tapia E. M. [78]	2006	ISM wireless	250kbps at 2.4GHz	Acceleration, heart rate, ultra-violet exposure, RFID, and location beacon sensor	Portable kit of wireless sensors for pervasive computing	Battery	1
Wrist	2	1	Anliker U. [79]	2004	GSM/ UMTS wireless		ECG, SpO2, blood pressure, acceleration, and temperature	'Amon' portable tele-monitor	Battery	2
Finger	2	2	Cohen Z. [80]	2017	Wired	Wired	PPG sensor	Monitoring of the Blood Pressure	Wired power	4
Finger	2	2	Joshi A. [81]	2011	eZ430-RF2500	250kbps at 2.4GHz	ECG sensor	Heart-Rate Monitor using MSP430 Launch Pad	Battery	1
Finger	2	2	Wu Y. C. [82]	2009	Bluetooth	921.6 kbps	RFID ring-type pulse sensor	Heart rate monitor	Battery	3
Finger	2	2	Jang I. -H. [83]	2008	Zigbee	sample rate 40 Hz	ring-type heart rate and pulse oximeter sensors	Heart rate and pulse oxygen monitor	Battery	3
Finger	2	2	Oliver N. [84]	2006	Bluetooth	2.4 GHz	Pulse oximetry sensor	Medical monitoring system	Battery	3
Finger wrist, chest	2	2	Shnayder V. [85]	2005	ZigBee	250kbps at 2.4GHz	ECG, pulse oximeter, EMG, and motion-activity sensor	CodeBlue' mote based system	Battery	1
Finger chest arm	2	2	Mundt C. W. [86]	2005	Bluetooth	9600bps at 2.4GHz	ECG, accelerometers, pulse oximetry, temperature, respiration, heart rate, and BP	'Lifeguard' multiparameter wearable physiologic monitoring	Battery	3

Table 1.5. (continues) Description of various sensors

Sensor location	Purpose	Develop stage	Author (First)	Year	Communication method	Frequency band	Sensors or device	System description	Power source	Network
Finger hand glove	1	2	Borghetti M. [87]	2013	MAX1472 wireless	10kbps at 433MHz	Strain sensors	Measuring finger flexion for Rehabilitation Purposes	Battery	1
Hand, glove	5	3	Niazman d K. [88]	2011	ISM wireless	2Mbps at 2.4GHz	3D-accelerometer and force sensor	Smart glove for assessment of Parkinson's Disease	Battery	1
Hand, chest	2	2	Lam S. C. K. [89]	2009	Bluetooth	2.4GHz	PPG, Pulse rate, Breathing rate, SpO2, and OSA prediction	wearable biosensor and mobile phone monitoring	Battery	3
Hand, glove	2	2	Simone L. K. [90]	2007	ZigBee	250kbps at 2.4GHz	Bend sensor	Glove	Battery	1
Hand, glove	2	2	Lorussi F. [91]	2005	N/A	N/A	Strain fabric sensor	Sensorized glove	Battery	4
Hand, glove	5	2	Prochaz ka A. [92]	1997	N/A	N/A	Stimulated electrodes and position sensor	Stimulator garment (glove)	Battery	4
Arm	2	2	Jauregi I. [93]	2017	RFID	860-960 MHz	Temperature sensor	Measures the skin temperature	RFID	1
Arm, eye, tooth	2	2	Matzeu G. [94]	2015	WBAN wireless		Optical pH, conductivity, sodium, temperature, Tattoo, and graphene	Wearable chemical sensor for monitoring biological fluids	Battery	1
Arm	2	2	Giorgino T. [95]	2009	Blue-tooth	2.4GHz	Strain sensors	Sensorized shirt	Battery	3
Arm	2	2	Miwa H. [96]	2007	N/A	N/A	Accelerometer and temperature sensor	Sleep Roll-over Detection and Sleep Quality Measurement		4
Waist, chest	2	2	Yi W. J. [97]	2013	CC2560 Bluetooth	2.4GHz	ECG, PCG, accelerometer, and temperature sensor	FPGA real-time acquiring fetal ECG/PCG signals	Battery	3
Waist, wrist	1	2	Mo L. [98]	2012	ZigBee	38.4kbps at 2.4GHz	Accelerometers and displacement sensors	Multisensor monitoring human physical activity	Battery	1
Waist	4	2	Borges L. M. [99]	2008	WSAN, Wi-Fi, GSM	2.4GHz	ECG and flex piezoelectric pressure sensor	Monitor fetal movement and ECG signals	Battery	3

Table 1.5. (continues) Description of various sensors

Sensor location	Purpose	Develop stage	Author (First)	Year	Communication method	Frequency band	Sensors or device	System description	Power source	Network
Waist	3	2	Akay M. [100]	2003	Wired	N/A	Accelerometer	Monitor hemiplegic Patients	Battery	4
Head	2	2	Matiko J. W. [101]	2015	Atmel ZigBee	2.4 GHz	EEG sensor	A self-powered wearable headband for EEG detection	Solar energy	1
Head	1	2	Gruebler A. [102]	2014	Wireless		EMG sensor	Recognize facial expressions	Battery	1
Head	5	2	Lin C. T. [103]	2014	Bluetooth	921kbps at 2.4GHz	EEG sensor	Dry EEG sensor to monitor driver's vigilance status	Battery	3
Head	5	1	Duvinage M. [104]	2013	Bluetooth	2.4GHz	EEG sensor	Emotiv Epoc headset	Battery	3
Head	3	2	Kim J. [105]	2012	CC2510 wireless	4kbps at 2.4GHz	Magnetic sensors	Wearable headset with tongue drive wheelchair navigation	Battery	1
Head, chest, leg, wrist	2	2	Chávez-Santiago R. [106]	2012	WBAN wireless	528MHz	EEG, SpO2, and EMG sensor	Medical ultra wideband BAN	Battery	2
Head, wrist	2	3	Riera A. [107]	2008	ENOBIO ZigBee		EEG and ECG sensor	ENOBIO device	Battery	1
Head, chest, glove	2	3	Katsis C. D. [108]	2006	Bluetooth	721kbps at 2.4GHz	ECG , EMG, and EDA sensor	Assessment of affective physiological states	Battery	3
Ear	2	2	Nakamura T. [109]	2017	Wired	1200 Hz	EEG sensors	Automatic sleep monitoring	Wired	4
Ear	2	2	Da He D. [110]	2015	CC2500 wireless	2.4 GHz	ECG, PPG, and accelerometer	Wearable vital signs monitor at the ear	Battery	1
Ear	2	2	Kollmann D. [111]	2013	CC2540 Bluetooth	2.4GHz	Pulse oximeter	Pulse oximeter using Vertical Cavity Surface Emitting Laser	Battery	3
Ear, hand, finger, wrist	2	2	Li K. [112]	2012	ZigBee	2.4GHz	Reflectance pulse oximeter	Wireless reflectance pulse oximeter	Battery	1

Table 1.5. (continues) Description of various sensors

Sensor location	Purpose	Develop stage	Author (First)	Year	Communication method	Frequency band	Sensors or device	System description	Power source	Network
Ear	2	2	Patterson J. A. C. [113]	2009	N/A	N/A	PPG sensor	Ear-worn reflective PPG sensor for Heart Rate Monitoring	Wired	4
Ear	2	3	Aziz O. [114]	2007	CC2420 ZigBee	250kbps at 2.4GHz	Pulse oximeter and accelerometer sensor	BSN monitoring postoperative recovery at home	Battery	1
Eye	5	3	Qusba A. [115]	2014	Wireless	100 kbps at 4MHz	Artificial Retina	Microfluidic implant flexible coil	Wireless power	1
Eye	5	2	Huang Y. C. [116]	2013	Wireless		Contact lens micro-capacitor sensor	Wireless intraocular pressure monitoring	Wireless power	1
Eye	5	2	Cheng H. W. [117]	2013	Wireless		Contact Lens Sensor Artificial Retina	Wireless intraocular pressure monitoring	Wireless power	1
Eye	5	2	Liao Y. T. [118]	2012	wireless	1.8 GHZ	Contact Lens Sensor	Wireless glucose monitoring	Wireless power	1
Eye	5	3	Miura Y. [119]	2011	N/A	N/A	Artificial Retina	Wireless power artificial retina	Wireless power	4
Neck	2	3	Fontana J. M. [120]	2014	RN-42 Bluetooth	125kbps at 2.4GHz	Jaw motion sensor, gesture, and accelerometer	Wearable monitor of ingestive behavior	Battery	3
Leg, arm	2	2	To G. [121]	2013	A2500R2 4 wireless	4kbps at 2.4GHz	Accelerometers and gyroscopes sensor	Robotic and Human Motion Tracking	Battery	1
Leg	1	2	Stupar D. Z. [122]	2012	XBee-PRO ZigBee	250kbps at 2.4 GHz	Fiber-optic curvature sensor	Human joint moving monitor	Battery	1
Leg, arm, chest	2	2	Milenković A. [123]	2006	CC2420 ZigBee	250kbps at 2.4 GHz	Accelerometer and ECG sensor	BAN based accelerometer and ECG monitoring	Battery	1
Foot	2	2	Bamberg S. J. M. [124]	2008	DR3000-1 wireless	115.2 kbps at 916 MHz	Accelerometers , gyroscopes, force, bend, and pressure	Shoe	Battery	1
Foot	4	2	Rimet Y. [125]	2007	Wireless		SpO2 and actimeter	Infants multiparameter monitor	Battery	1

Table 1.5. (continues) Description of various sensors

Sensor location	Purpose	Develop stage	Author (First)	Year	Communication method	Frequency band	Sensors or device	System description	Power source	Network
Foot	2	2	Benbasat A. Y. [126]	2003	TDMA wireless	922kbps at 916 MHz	Accelerometer, gyroscopes, and pressure sensor	Wireless on-shoe gait analysis	Battery	1
Skin	2	2	Chen Y. [127]	2016	N/A	N/A	Biocompatible strain sensor	Long-term health monitoring	Battery	4
Skin	1	3	Castillejo P. [128]	2013	Bluetooth	115kbps at 2.4GHz	Temperature sensor	Physiological monitor of sportsman, fireman, woman.	Battery	3
Skin	2	3	Lee S. [129]	2013	WBAN	20 Mbps	Electrodes	Continuous bio-signal monitor	Battery	1
Skin	2	2	Kim D. H. [130]	2011	N/A	N/A	Strain, Photodetector, and temperature sensor	Electronic second skin	Battery	4
Skin	1	2	Coyle S. [131]	2009	wireless		Textile and pH sensor	Textile-based sensor (‘Biotex’)	Battery	1
Skin	2	2	Haahr R. G. [132]	2008	PAN wireless	4kpbs at 2.4GHz	EMG and SpO2 sensor	Electronic patch	Battery	2
Skin	2	3	Dolgov A. B. [133]	2006	nRF2401 wireless	1Mbps at 2.4GHz	Temperature, acceleration, and GSR sensor	Wireless medical and sport monitoring	Battery	1
Implant	5	1	Farra R. [134]	2012	MICS wireless		Release drug	Wirelessly controlled drug delivery	Battery	1
Implant	2	2	Ahmadi M. M. [135]	2009	wireless	13.56 MHz	Glucose sensor	Continuous blood glucose monitoring	Wireless power	1
Implant	5	3	Wang J. [136]	2008	N/A	N/A	Cochlear	MEMS Cochlear Prosthesis	Wireless power	4
Implant	5	3	Gómez E. J. [137]	2008	GPRS, WAN wireless		Glucose sensor, insulin pump	Intelligent control assistant for diabetes	Battery	3
Implant	2	3	DeHennis A. D. [138]	2006	AM	30 kHz bandwidth	Multisite pressure sensor	A fully integrated sensing system for the detection of arterial stenosis	Wireless power	1

Table 1.5. (continues) Description of various sensors

Sensor location	Purpose	Develop stage	Author (First)	Year	Communication method	Frequency band	Sensors or device	System description	Power source	Network
Implant	2	3	Valdastri P. [139]	2004	wireless	40kbps at 433.92MHz	Pressure sensor	Implant telemetry system	Battery	1
Implant	2	1	Adler D. G. [140]	2003	M2A Given imaging		Capsule Endoscopy	Wireless capsule for small bowel image	Battery	1
Implant	2	2	Poscia A. [141]	2003	RS232	1200 baud	Glucose sensor	In vivo micro-pump to record glucose level	Battery	1
Implant	2	2	Beach R. D. [142]	2001	EIA /NTSC TV format		CCD camera	Video telemetry system in vivo	Battery	1
Implant	1	2	Santini J. T. [143]	1999	N/A	N/A	Release drug	A controlled-release microchip	Micro battery	4

Indication by numbers in the table

Purpose: 1. Fitness. 2. Physiological parameter monitoring. 3. Senior monitoring. 4. Children monitoring. 5. Application for a specific disease.

Developing stage: 1. Research stage. 2. Prototype stage. 3. Commercial product stage.

Network types: 1. Wireless point to point communication between specific devices, include ZigBee. 2. Wireless point to point communication to a common device such as smartphone. 3. Wireless Wi-Fi or Bluetooth connects to a gateway device. 4. Wired communication. 5. No communication.

Abbreviation

ANT: A network protocol; WSN: wireless sensor network; EMG: Electromyography sensor; PCG: Phonocardiogram; ECG: Electrocardiogram; EEG: Electroencephalographic; EDA: Electrodermal activity; PPG: Photoplethysmogram; QRS: QRS complex of ECG wave; BP: Blood pressure; SpO2: Oxygen saturation; OSA: Obstructive sleep apnea; GSR: Galvanic skin response; MICS: Medical Implant communications service; NFC: Near field communication; EIA: Electronics industry association; NTSC: National television system committee; RF: Radio frequency; RFID: Radio frequency identification; ISM: Industrial, Scientific, and Medical.

2). *Sensors Worn on Wrist*

With wireless and wired communications, electrical devices worn on the wrist can be used to monitor and record the wrist joint rotary angles by EMG (electromyography) sensors [69]; the electrical signals generated by muscles; the wrist movements by accelerometer [2, 59, 73, 78, 79]; pulses from the ulnar artery at the wrist by radio frequency sensor [71] or piezoelectric sensor [71]; the slight strain variation under the skin; the heart/pulse rates by using ECG electrodes [2, 74, 75, 76, 79]; the blood pressure status by a WSN based mobile blood pressure device [76] or a portable telemedical monitor (AMON) device [79]; the temperature by thermometers [2, 73, 79]; and the blood glucose levels by microwave sensors [77]. The sensing modalities can also be other than electrical ones such as to detect PPG (photoplethysmogram) signals by infrared LED and detectors; blood oxygen saturation levels (SpO2) by pulse oximeters [72, 74, 79]; ultra-violet light exposure by optical sensors [78], human reaction time estimation by MEMS gyroscope sensors [67], and heart sounds by acoustic sensors at the wrist [68].

The wrist is a perfect location for the wearables as people are used to wearing wrist watches so that the acceptance for such devices encounters fewer obstacles for both consumers and markets. However, the devices at wrists also suffer from arm motions during daily activities and so the signals inherently contain a high level of noises. Thus signal processing techniques and multiple sensors including accelerometers are needed to detect the motions and eliminate the noises. The attachment or contact of sensors on skins is also a concern in practical uses. The small gaps between the sensor surface and skin can create higher impedance to attenuate RF signal magnitudes or a complex scattering issue for reflectance or transmittance measurements.

3). *Sensors Placed on Finger*

Sensors placed on fingers can monitor blood pressures by PPG sensor [80], ECG signals by electrodes [81, 85, 86], ring-type pulse rates by optical sensors [82, 83], and SpO2 by pulse oximetry [84, 85, 86]. Finger position and flexion of a patient can be detected by strain sensors [87] for rehabilitation purposes.

Fingers are another location to get acceptance from patients or markets for wireless sensors, however, allow fewer physiological parameters to be measured than on the wrist. The size of the wearable device becomes a major challenge for comfort and appearance.

4). *Sensor Gloves Worn on Hand*

A pair of gloves worn on hands can be used to monitor and record finger postures, movements, flexion to assess Parkinson's disease symptoms by position sensors [92], strain fabric sensors [91], bent sensors [87, 90], force sensors [88], and accelerometers [88], while optical sensors [89] are used to monitor PPG and pulse rates. The glove solutions are suitable for clinical uses as the environments are well controlled. Wireless communication, reduces burdens from patients who suffer from tremors as compared to a wired system, from the gloves to a computer can be a line-of-sight link and will not encounter variables in the daily activities, thus networking issue rarely exist.

5). *Sensors Placed on Arm*

Sensors have been placed on arms to measure the skin temperature by an RFID temperature sensor [93], body sweat conditions by an optical pH sensor [94], and upper limb postures by strain sensors [95]. Sleep quality can be assessed by recording the turn frequency and occurrences at night by accelerometers and body temperatures by thermometers [96]. Wearables on arms require fewer constraints in device designs as there are sufficient spaces for comfortable wearability. The motions of arms and skin contact also contain signal and noise issues.

6). *Sensors Placed on Waist*

Sensors can be placed on the waist of a pregnant woman to acquire fetal ECG and phonocardiogram (PCG) signals by electrodes and microphones [97, 99]. The fetal movements can be detected by flexible piezoelectric pressure sensors [99]. Routine human physical activities

can be recorded by accelerometer and displacement sensors for motions and postures [98]. They have also been used specifically to monitor post-stroke hemiplegic patients by accelerometers [100]. This type of monitoring functions usually requires a long period of time for recording and it is better to be conducted at home or therapy clinics. Thus wireless communication provides advantages over a wired system. As a smartphone or data transceiver can also be placed on the waist, the communication link requires a very short distance.

7). *Sensors Placed on Head*

Many studies have placed electroencephalogram (EEG) electrodes [101, 104, 106, 107, 108] on the head to measure brain waves. High counts of EEG electrodes can reveal brain activities. However, they are mostly wired systems due to system complexity. Wireless EEG systems provide mobility so brain waves can be recorded while one conducts daily activities. However, EEG signals are prone to contain interference signals generated by motions and activities that are not related to the target behaviors. It is also not practical to wear a high-count EEG cap while the patient resumes normal daily activities. Therefore, wireless EEG systems face tremendous technical challenges in signal integrity, noise filtering, spatial specificity, and power sources. Some examples are an EEG system with solar energy harvesters [101]; one with EMG sensors to recognize facial expressions [102]; one to monitor driver's vigilance status with dry EEG electrodes [103]. Some combine with other sensors such as the one allows to drive wheelchair navigation by magnetic sensors on the tongue [105]; the one to monitor effective physiological states by electrodes and magnetic sensors [108].

8). *Sensors Placed on Ear*

As placing electrodes on the head may not be comfortable, ears may be a good candidate location as the sensors can be shaped like an earplug. Signal acquisitions are demonstrated with electrocardiogram signals by ECG electrodes locally near the ear [110]; ballistocardiogram (BCG) signals with accelerometers to detect body motions [110]; pulse rates

by PPG sensors [110, 113] and SpO2 signals by pulse oximeters [110, 111, 112, 114]. As compared to the excessive motion in hands and fingers, ears provide more reliable signals. Sleep patterns of brain waves have been acquired by EEG sensors for sleep apnea diagnosis [109]. A wireless system provides less constraint in wire management during the studies.

9)*. Sensors Placed on Eye*

Monitoring eyes are critical for glaucoma patients. Currently, patients receive examination only during clinical visits which the intraocular pressures are not continuously monitored. There are many technical challenges to design wearables, such as contact lens and glasses, or implants, such as intraocular lenses. The main issue is due to the limited space thus the electronics for sensing and communications, as well as the battery or power source, have to be miniaturized. Thus designs often include considerations in both wireless communication and wireless power harvesting. Coils acting as antennas are used for power and signal transmission in eyes [116, 117, 118, 119]. Another example is a microfluidic implant that incorporates a flexible coil for the contour of the eyes [115]. The intraocular pressure can be detected by the microscale capacitive sensors which consume low powers [116]. New techniques are also emerging. An electrochemical sensor is proposed to detect glucose levels in tears for diabetic patients [118]. As implants, artificial retina, consisting of a thin-film transistor matrix on a flexible substrate to stimulate retinal neurons with inductive coupling to transfer power and data, are being clinically tested [119]. The system requires visual image data to be transferred from a wearable, such as a pair of glasses, to the implant. The technical challenges to maintain signal integrity and reliable power transfer become complex as the component size constraints are tight.

10)*. Sensors Placed on Neck*

A wearable device for monitoring of ingestive behaviors has been demonstrated with a jaw motion sensor on the neck to monitor chewing [120]. A hand gesture sensor to monitor hand-to-mouth gestures and an accelerometer to monitor body motion are also included. All sensors

are wirelessly interfaced to a smartphone with Bluetooth communication in order to enhance accuracy.

11). *Sensors Placed on Leg*

Accelerometers [121, 123] and gyroscope sensors [121] are used on legs to monitor motions and gestures. While wire communication among sensors to processors is an option, wireless communication provides pervasive means without mobility limitation. Other sensor modalities can also be incorporated such as monitoring joint motions by fiber-optic curvature sensors [122] and recording EMG signals by electrodes [123].

12). *Sensors Placed on Foot*

Sensors have been placed directly on foot for quantitative gait analysis including accelerometers, gyroscopes, force sensors, strain sensors, pressure sensors, piezoelectric sensors, and capacitive sensors [124, 126]. With the multi-modalities, sensors are integrated within a wireless network. SpO2 and pulses by oximetry, locomotor activities by an infrared actimeter to record the activities, and the prone position of infants by actimeter are wirelessly monitored on foot [125] without the constraint of wires that impose risks for infants.

13). *Sensors Placed on Skin*

Although almost all sensors are in contact with skin, this type of sensors is classified for skin health detection or vital sign monitoring in which sensors adhere to the skin for a long period of time. As skins can be easily agitated, long-term monitoring requires rigorous biocompatibility such as flexible strain sensors [127, 130] to conform onto skins and medical/sport applications for temperature, galvanic skin response (GSR) sensor and electrodes [128, 129, 130, 133]. Such sensors often are based on flexible substrates thus the electronics and packaging, particularly antenna designs, under possible mechanical deformation require special considerations. The skin and tissue conditions also affect wireless signal propagation and antenna radiation patterns. An

example of such integration is the electronic second skins [131, 132] which consist of strain sensors, photodetectors, temperature sensors, textile sensors, pH sensors, SpO2 sensors, and EMG electrodes to obtain signals in multiple modalities that mimic human skins.

14). *Implantable Sensors*

Implantable sensors are implemented in the body for applications such as drug delivery [134, 143], continuous blood glucose monitoring [135, 137, 141], artery blood pressure monitoring [138] and cochlear prosthesis [136]. Some of them are discussed as in vivo telemetry in [142]. Temporary implants such as in vivo imaging capsules for GI tracts including colon, small bowel, stomach, and esophagus also utilize high data rate communication to transmit images from the capsule to a wearable receiver [139, 140]. In such temporary in-vivo devices, the battery is designed to be consumed by the end of diagnosis. To keep the capsule small for passing small GI tracts, battery size and capacity is limited.

For long-term implants, the power source to operate the device in which wireless communication consumes a high percentage of energy becomes critically challenging. Many systems for wireless data acquisition require a wearable module to communicate with the implants and control functions. The power consumption constraint is more stringent for deep body implants than for transcutaneous signal transduction due to RF energy absorption and scattering in tissues for both wireless communication and power transfer.

1.4 Trends and Challenges of Wearable Technology Developments

With rapid developments and market needs for wearable technologies, more advanced wearable devices are expected. Miniature sensors and new sensing modalities enhanced by MEMS and Nanotechnologies will empower the low-power wireless and smart electronics that have more computing capability to achieve better accuracy, reliability, and efficiency. High-density sensor array or matrix, providing multiple parameters in vivo and in situ continuously, will

enable new research tools for medical applications. Eventually, they will be utilized in clinical settings for the advantages in diagnosis.

With developments of new substrate material and fabrication techniques, the next generation of wearables will have the features of flexibility, biocompatibility, low power consumption, long-term usages, and reliable connectivity. The device will integrate energy harvesting mechanisms for batteryless or infrequent-charging operations. To avoid any discomfort, flexible, soft and stretchable substrates are preferred when in touch with skin; or even the sensing modality can be implemented with contactless means. The wearable device should be able to be personalized for an individual's conditions given flexibility in signal processing and data communication capacities that can be expanded to adapt classification, pattern recognition, and artificial intelligence algorithms. With current wireless communication protocols, the device can already be connected to cloud servers and analyzed by big data and cloud computing techniques. Further enhancement in data rates, power consumption, and communication distances for different types of physiological parameters will be needed to realize efficient radio spectrum uses. Future trends in protocols and standardization efforts should also focus on data security, signal encryption, and protection of devices against power surge, strong field interferences in environments and induced thermal effects by wireless energy, as well as long-term effects on tissues by RF signals.

CHAPTER 2

WEARABLE DOUBLE-RESONANCE SENSORS FOR MONITORING DEHYDRATION

Nomenclature

In following symbols, subscript "*a"* notes the outer ring (circular loop) parameters and subscript "*b"* notes inner ring (split ring) parameters.

l_a, l_b the ring perimeters,

r_a, r_b the ring radiuses,

g_a, g_b the ring-port gaps,

λ_a, λ_b the wavelengths,

n the number of the waveguide-mode resonance in harmonic order

ε the relative permittivity

c_0 the light speed in free space

f_{a0}, f_{b0} the resonance frequencies when the ring is in free space

f_a, f_b the S_{11} resonant frequencies of the outer ring and inner ring

ω_a, ω_b the resonant angular frequency

ε_{a_eff}, ε_{b_eff} the effective relative permittivity on the outer ring and inner ring

C_1, C_2, equivalent capacitances of the outer ring

R_1, R_2, equivalent resistances of the outer ring

L_1, and L_2 equivalent inductances of the outer ring

L_a total equivalent inductance of the outer ring

C_b equivalent capacitance of the inner-ring

R_b equivalent resistance of the inner-ring

L_3, L_4 equivalent inductances of the inner-ring

L_b total equivalent inductance of the inner-ring

L_{m1}, L_{m2} the mutual inductances between the two rings

L_m the total mutual inductance between the two rings

k the coupling coefficient

S_{11} is the return loss, a scattering parameter

Z is the impendence of the equivalent circuit

2.1 Introduction

Athletes should intake minimum 250 mL of fluid every 20 minutes during exercises for maintaining a euhydrated state [144]. Significant loss of body water will result in dehydration that harms normal body functions. Hence, using a wearable biomedical sensor to quickly identify dehydration levels of the human body is important for athletes, workers, and soldiers.

An impedance sensor has been reported for measuring skin hydration [145]. However, the impedance sensor can only monitor the epidermal hydration. Using radio-frequency sensors to analyze the dielectric properties of biological tissues has the advantages of being non-invasive, potentially contactless and fast [146 - 148]. The electronics can also be cost-effective owing to the recent advances of high speed integrated circuits. Additionally, microwave sensing mechanism based on tissue dielectric properties can significantly identify the large difference of hydration levels in tissues [149 - 150]. Measuring the scattering parameters and monitoring the resonant frequency change can identify and calculate the permittivity of targets [151, 152]. Monitoring resonant frequency is more reliable and has higher accuracy than monitoring the amplitude variations, such as measuring the resonant frequency of split-ring sensors to monitor the blood glucose levels [153, 154]. Recently, a split-ring sensor has been proposed to identify water and other liquids using the resonant frequency [155]. A split-ring resonator was used to measure the concentration of heparin in water by the resonant frequency [156]. A simulation study was presented to detect the spurious material by the multi-resonant split rings [157].

Due to the complex tissue composition, the dielectric properties of biological tissues, however, vary at different frequencies [158, 159] making identification of tissues to be difficult. Hence, a double-resonance sensor is proposed to identify dehydration of tissue with two distinguishable resonant frequencies to enhance the data signatures. In order to obtain a larger frequency span between the two resonances, two different types of resonators were employed. One is the circular-loop resonator and another is the split-ring resonator. Dehydration in biological tissues will change the dielectric properties of the tissues and the capacitance of the sensor circuit, which will result in changing the sensor-resonance frequencies.

2.2 Electromagnetic Analysis of the Double-ring Resonator

The double-ring resonator has a circular loop (used as the outer ring) and a split ring (used as the inner ring). Because the circular loop and the split ring have different resonant wavelengths, the resonator has two distinguishable resonant frequencies. Firstly, the double-ring resonator is analyzed and designed by waveguide method and the electromagnetic finite-element simulation. Secondly, resonant frequencies and wavelengths of the outer ring and inner ring are deduced. Then, the effective relative permittivity, *Q* factor, frequency sensitivity, power radiation patterns, *E*-field distributions, surface current distributions and *H*-field distributions of the double-ring resonator are presented, respectively.

A. Circular-Loop Resonator

A circular-loop resonator consists of a copper-foil ring with a feed port and the port excitation is set as the lumped type with 50 Ω port impedance. 3-D finite-element simulation model of the circular-loop resonator is shown in Figure 2.1. To find the design parameters, the simulation results were carried out by the electromagnetic finite-element method and demonstrated an infinite periodic resonant waveform of S_{11} (input port reflection coefficient) with an attenuation amplitude as shown in Figure 2.2.

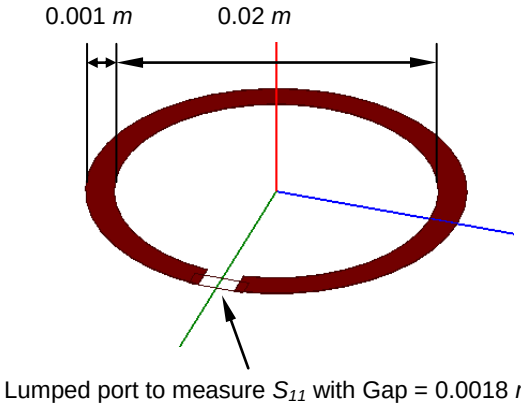

Figure 2.1. 3-D finite-element simulation model of the circular-loop resonator.

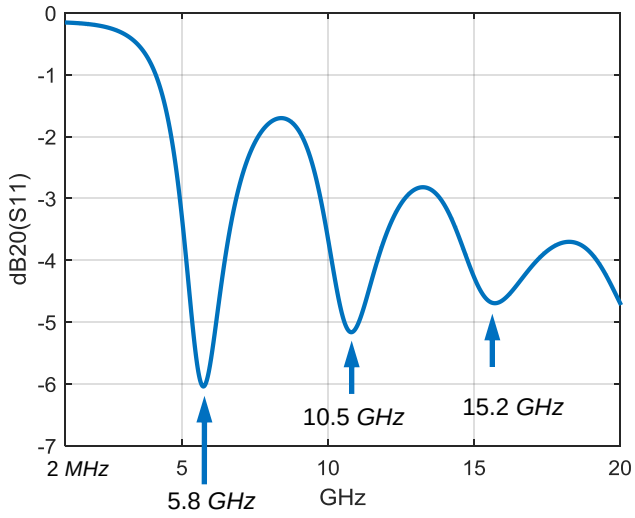

The S_{11} resonant frequency f_n is 5.8 *GHz*, 10.5 *GHz*, and 15.2 *GHz*, respectively.

Figure 2.2. Simulation results by the electromagnetic finite-element method.

Employing the waveguide analysis method [160], the infinite resonant frequencies and the perimeter of the ring may be expressed as an integer multiple of wavelength adding 1/4 wavelength, that is,

$$l_a = n\lambda_a + \lambda_a/4 \tag{2.1}$$

where $l_a = 2\pi r_a - g_a$

In Eq.(2.1), l_a is the perimeter of the ring, r_a is the ring radius, g_a is the gap of split port, λ_a is the resonant wavelength, and n is the number of waveguide-mode resonance in harmonic order. The length of the circular ring l_a equals the perimeter of the ring minus the port gap. The wavelength equation has an infinite periodic expression and the wavelength can be expressed as follows [160].

$$\lambda_a = \frac{c_0}{f_n\sqrt{\varepsilon}} \tag{2.2}$$

where c_0 is the light speed in free space, ε is the relative permittivity, f_n is the resonant frequency, and λ_a is the resonant wavelength.

Substituted Eq.(2.2) into Eq.(2.1), the waveguide-mode resonant frequencies of S_{11} may be expressed as,

$$f_n = \frac{c_0(n+1/4)}{(2\pi r_a - g_a)\sqrt{\varepsilon}} \tag{2.3}$$

Eq.(2.3) shows that the resonant frequencies depend on the ring size, the light speed, and the relative permittivity. When the average radius of the ring r_a = 0.0105 *m* as shown in Figure 2.1 and the relative permittivity ε = 1 (in free space), the resonant frequency f_n equals 5.8 *GHz*, 10.5 *GHz*, and 15.2 *GHz*, according to Eq.(2.3), which was verified by the simulation results in Figure 2.2. As the harmonic order *n* of the resonant frequency increases, the amplitude of the S_{11} attenuates as shown in Figure 2.2. Therefore the frequency range for this sensor is limited within the first harmonic order of the resonant frequency within 6GHz. The resonant frequency of 1+1/4 wavelength is 5.8*GHz* and is chosen for the double-ring resonator.

When *n* = 1, the S_{11} resonant frequency in Eq.(2.3) of the circular ring is,

$$f_a = \frac{c_0\left(1+\frac{1}{4}\right)}{(2\pi r_a - g_a)\sqrt{\varepsilon}} \tag{2.4}$$

where f_a is S_{11} resonant frequency when *n* = 1.

B. Double-rings Resonator and sensitivity

In order to obtain two distinguishable resonant frequencies, a split ring is placed into the circular loop as shown in Figure 2.3, where the split ring is named as the inner ring and the

circular loop is named as the outer ring. The resonant frequency of the inner ring follows the half wavelength expression [161, 162] and the perimeter of the split ring equals 1/2 guided wavelength at the resonant frequency, that is,

$$l_b = \lambda_b/2 \tag{2.5}$$

where $l_b = 2\pi r_b - g_b$

where l_b is the perimeter of the split ring, r_b is the split radius, g_b is the gap of the split ring, and λ_b is the wavelength.

S_{11} resonant frequency of the inner ring may be expressed as,

$$f_b = \frac{c_0}{2(2\pi r_b - g_b)\sqrt{\varepsilon}} \tag{2.6}$$

where f_b is the resonant frequency of the inner ring.

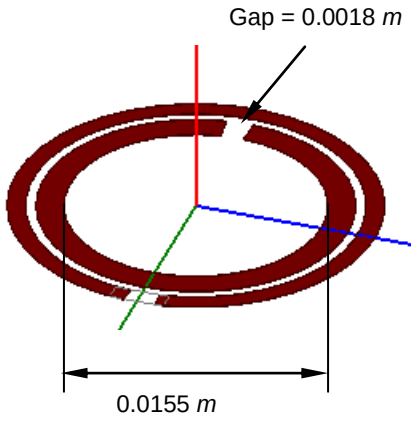

Figure 2.3. 3-D finite-element simulation model of the resonator with an outer ring and an inner ring.

Using Eq.(2.4) and Eq.(2.6) as well as the ring's dimension, r_a = 0.0105 *m*, g_a = 0.0018 *m*, r_b = 0.0085 *m*, and g_b = 0.0018 *m*, two resonant frequencies can be calculated as 5.8 *GHz* and f_b

2.9 *GHz*, respectively. The electromagnetic finite-element simulation results confirmed that the resonant frequency f_a of the outer ring is 5.8 *GHz* and f_b of the inner ring is 2.9 *GHz*, as shown in Figure 2.4. When there is only the outer ring, the S_{11} coefficient is plotted by the blue line. When there are the outer ring and the inner ring, the S_{11} coefficient is plotted by the red line.

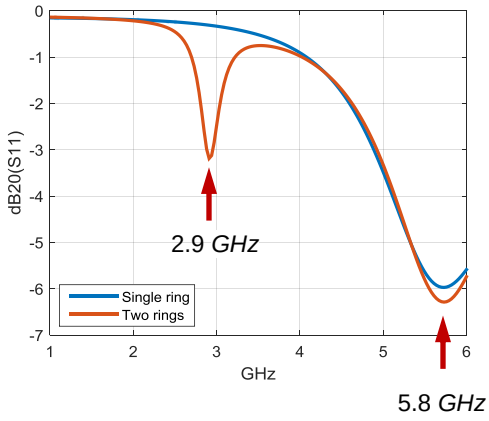

Resonant frequency of the outer ring f_a is 5.8 *GHz* and resonant frequency of the inner f_b is 2.9 *GHz*.

Figure 2.4. The electromagnetic finite-element simulation results.

A frequency sensitivity function of the outer ring by the relative permittivity can be defined by the derivative of the function f_a of the variable ε from Eq.(2.4) as follow.

$$\frac{df_a}{d\varepsilon} = -\frac{c_0}{(8/5)(2\pi r_a - g_a)}\varepsilon^{-3/2} \tag{2.7}$$

Substituted ra = 0.0105 *m* and g_a = 0.0018 *m* into Eq.(2.7), the frequency sensitivity function of the outer ring is,

$$\frac{df_a}{d\varepsilon} = -9.7c_0\varepsilon^{-3/2} \tag{2.8}$$

The frequency sensitivity function of the inner ring by the relative permittivity is a derivative of the function f_b of the variable ε from Eq.(2.6) as follow.

$$\frac{df_b}{d\varepsilon} = -\frac{c_0}{4(2\pi r_b - g_b)}\varepsilon^{-3/2} \tag{2.9}$$

Substituted rb = 0.0085 *m* and g_b = 0.0018 *m* into Eq.(2.9), the frequency sensitivity function of the inner ring is,

$$\frac{df_b}{d\varepsilon} = -4.8c_0\varepsilon^{-3/2} \tag{2.10}$$

The frequency sensitivity functions by the relative-permittivity at the resonant frequencies, f_a and f_b, show that the circular loop (outer ring) is more sensitive than the split ring (inner ring) after compared Eq.(2.8) and Eq(2.10).

C. Double-ring Resonator Mounted on PCB

To build a practical sensor as shown in Figure 2.5, the double-ring resonator was mounted on a printed circuit board (PCB) and a copper film pad was added in the resonator center to construct the completed double-ring resonator, where the copper pad with radius 6.5 mm is placed in the resonator center to boost the circuit *Q* values by matching the load impedance to the 50 Ω port impedance. Geometric sizes of the double-ring resonator are listed in Table 2.1.

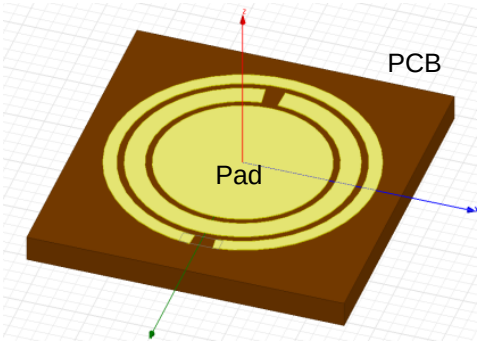

Figure 2.5. 3-D finite-element simulation model of the double-ring resonator mounted on a printed circuit board (PCB) with a copper film pad.

Table 2.1. Geometric sizes of the double-ring resonator.

Outer-ring dimension (*m*)				Inner-ring dimension (*m*)				Pad (*m*)	
r_a	g_a	w_a	h_a	r_b	g_b	w_b	h_b	r_p	h_p
0.0105	0.0018	0.001	0.000025	0.0085	0.0018	0.0015	0.000025	0.0065	0.000025

Notes: Outer-ring size: r_a is the average radius, g_a is the gap, w_a is the strip width, and h_a is the strip thickness. Inner-ring size: r_b is the average radius, g_b is the gap, w_b is the strip width, and h_b is the strip thickness. Pad size: r_p is the radius and h_p is the pad thickness.

The PCB dielectric layer and the copper pad will change the space relative permittivity of the resonator. The non-uniform dielectrics can be accounted by the effective relative permittivity, ε_{eff} , [146, 162, 163]. Due to the difference in distance between the copper pad and the rings, the copper pad has different effects for the outer and inner rings. Thus, the effective relative permittivities of the outer and inner rings will also be different. The effective relative permittivity ε_{a_eff} is used for the outer ring and ε_{b_eff} is used for the inner ring. Replaced ε in Eq.(2.4) by ε_{a_eff}, the outer-ring resonant frequency becomes,

$$f_a = \frac{c_0(1+1/4)}{(2\pi r_a - g_a)\sqrt{\varepsilon_{a\_eff}}} \tag{2.11}$$

Replaced ε in Eq.(2.6) by ε_{b_eff} , the inner-ring resonant frequency becomes,

$$f_b = \frac{c_0}{2(2\pi r_b - g_b)\sqrt{\varepsilon_{b\_eff}}} \tag{2.12}$$

Eq.(2.11) and Eq.(2.12) show that the resonant frequencies of the two rings, f_a and f_b, depend only on the two ring's dimensions and the effective relative permittivities, ε_{a_eff} and ε_{b_eff}, which are affected by the PCB dielectric layer, the copper pad, and medium above the resonator.

The effective relative permittivity of the outer ring can be obtained from Eq.(2.11) as follows.

$$\varepsilon_{a\_eff} = \left(\frac{c_0(1+1/4)}{(2\pi r_a - g_a)f_a}\right)^2 \quad (2.13)$$

Eq.(2.13) expresses the relationship between the effective relative permittivity ε_{a_eff} and the resonant frequency f_a.

The effective relative permittivity of the inner ring can be obtained from Eq.(2.12) as follows.

$$\varepsilon_{b\_eff} = \left(\frac{c_0}{2(2\pi r_b - g_b)f_b}\right)^2 \quad (2.14)$$

Eq.(2.14) expresses the relationship between the effective relative permittivity ε_{b_eff} and the resonant frequency f_b.

Combining Eq.(2.4) with Eq.(2.11), when free space ε = 1, the effective relative permittivity of the outer ring can be obtained as follow.

$$\varepsilon_{a\_eff} = \left(\frac{f_{a0}}{f_a}\right)^2 \quad (2.15)$$

where f_{a0} is the resonant frequency when the outer ring is in free space, f_a is the resonant frequency when the ring is in non-uniform dielectrics,

Combining Eq.(2.5) with Eq.(2.12), when free space ε = 1, the effective relative permittivity of the inner ring can be obtained as follow.

$$\varepsilon_{b\_eff} = \left(\frac{f_{b0}}{f_b}\right)^2 \quad (2.16)$$

where f_{b0} is the resonance frequency when the inner ring is in free space, f_b is the resonance frequency when the ring is in non-uniform dielectrics.

Replaced the relative permittivity ε in Eq.(2.8) by ε_{a_eff} , the frequency sensitivity function of the outer ring is,

$$\frac{df_a}{d\varepsilon_{a\_eff}} = -9.7c_0{\varepsilon_{a\_eff}}^{-3/2} \tag{2.17}$$

Replaced the relative permittivity ε in Eq.(2.10) by ε_{b_eff} , the frequency sensitivity function of the outer ring is,

$$\frac{df_b}{d\varepsilon_{b\_eff}} = -4.8c_0{\varepsilon_{b\_eff}}^{-3/2} \tag{2.18}$$

Using the electromagnetic finite-element model of the double-ring resonator with and without a center pad, the simulation results of S_{11} parameter are shown in Figure 2.6. The pad radius in the finite-element model is 6.5 *mm* and thickness is 0.025 *mm*.

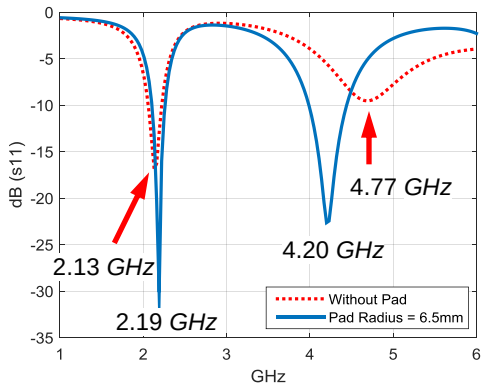

Figure 2.6. Electromagnetic finite-element simulation results of the double-ring resonator with the pad (blue solid line) and without the pad (red dot line).

As shown in Figure 2.6, when pad radius of the resonator is 6.5 *mm* and thickness is 0.025 *mm*, the resonant frequency of the inner-ring (split-ring type) is 2.19 *GHz* and the resonant frequency of the outer-ring (circular-loop type) is 4.20 *GHz*. Without the pad, the inner-ring

resonant frequency is 2.13 *GHz* and the outer-ring resonant frequency is 4.77 *GHz*. With the pad, the two resonant frequencies of the outer ring and inner ring become sharper than without the pad. The circuit's Q factors at the two resonant frequencies are boosted. The two different rings can contribute a larger resonant-frequency span over 2 GHz to the resonator.

D. Matching the Port Impedance by the Center Pad

The copper pad placed inside the inner ring as shown in Figure 2.5 was used to boost the circuit *Q* factors by matching the load impedance to the 50 Ω port impedance. With various pad radiuses, the double-ring resonator was simulated by the electromagnetic finite-element method, while the load impedances at the resonant frequencies are listed in Table 2.2. By increasing the pad radius, the load impedance at the resonant frequency f_a decreases and the load impedance at resonant frequency f_b increases.

Table 2.2. Various pad radiuses, resonant frequencies, and load impedances.

Pad radius (*mm*)	Resonant frequency f_a (*GHz*)	Load impedance at f_a (Ω)	Resonant frequency f_b (*GHz*)	Load impedance at f_b (Ω)
0 or no Pad	4.77	102	2.13	37
1	4.75	101	2.13	38
2	4.71	98	2.14	38
3	4.65	96	2.14	39
4	4.52	93	2.16	41
5	4.50	87	2.16	42
6	4.32	74	2.16	46
6.5	4.20	57	2.19	50

In order to analyze the load impedance changes when the resonator with a 6.5 *mm* pad and without a pad, the *S11* Smith chart is plotted in Figure 2.7 by the electromagnetic finite-element simulation, where the prime center of the Smith chart is assigned as 50 Ω.

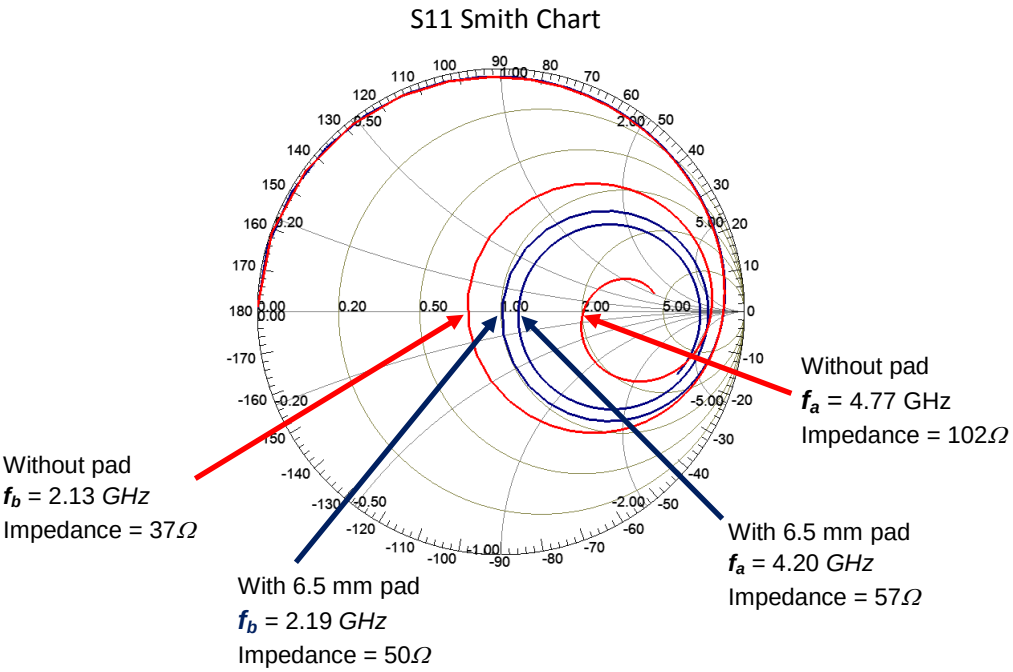

Figure 2.7. S_{11} Smith chart of the double-ring resonator is plotted by the electromagnetic finite-element simulation, where the blue line is S_{11} parameter plot with the pad and red line is S_{11} parameter plot without the pad.

The resonator without the pad compared with the resonator with the 6.5 *mm* pad, as shown in Figure 2.7, the outer-ring resonant frequency f_a shifts from 4.77 GHz to 4.20 GHz and the load impedance at the frequencies changes from 102 Ω *to* 57 Ω, while the outer-ring resonant frequency f_b shifts from 2.13 *GHz* to 2.19 *GHz* and the load impedance at the frequencies changes from 37 Ω *to* 50 Ω . The S_{11} Smith chart demonstrates that the load impedance of the resonator can match near 50 Ω port impedance using the center pad and the resonator circuit's *Q* factor is boosted.

E. Electromagnetic field distribution patterns of the resonator

To verify the design of the double-ring resonator, the power radiation distribution, the electrical field distribution, the surface-current distribution, and the magnetic field strength distribution of the resonator are presented, respectively.

The power radiation pattern of the double-ring resonator is shown in Figure 2.8, when the resonant frequency is 2.19 *GHz*.

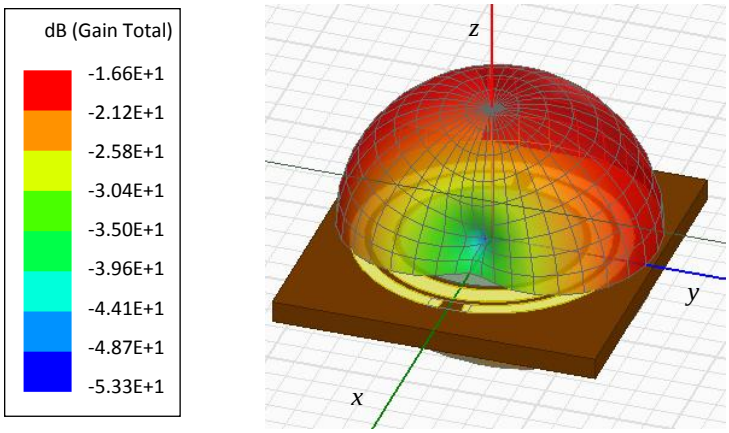

Figure 2.8. Power radiation pattern at the resonant frequency, f_b = 2.19 *GHz*.

As shown in Figure 2.8, when the resonance is at 2.19 *GHz*, the power radiation is directly overhead the resonator, and there is very little power transmitted along the *x*-axis.

The Power radiation pattern of the double-ring resonator is shown in Figure 2.9, when the resonant frequency is 4.20 *GHz*.

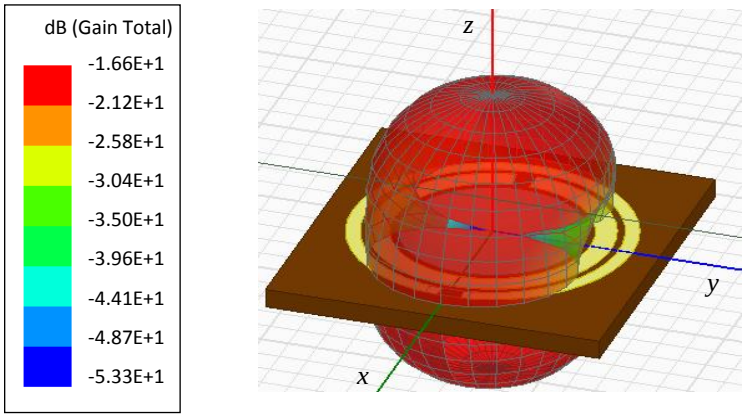

Figure 2.9. Power radiation pattern at the resonant frequency, f_b = 4.20 *GHz*.

As shown in Figure 2.9, when the resonance is at 4.20 *GHz*, the power radiation is directly overhead the resonator, and there is very little power transmitted along the *y*-axis.

At different resonant frequencies, the two power radiations spread normally to ensure the sample above the resonator can be sensed as shown in Figure 2.8 and Figure 2.9.

Electrical field (E-filed) distribution patterns on the resonator are shown in Figure 2.10, where the resonance frequency f_b = 2.19 *GHz*.

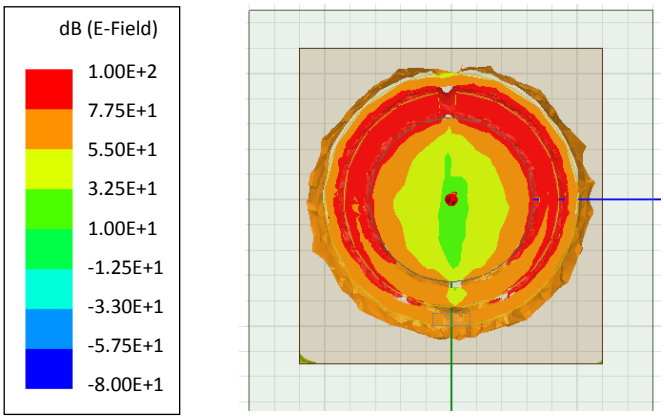

Figure 2.10. Electrical field (E-field) distribution on the resonator when the resonant frequency f_b = 2.19 *GHz* and the electrical field concentrated on the inner ring.

As shown in Figure 2.10, the electrical field distribution concentrated mainly on the inner-ring (split ring) at the resonant frequency, f_b = 2.19 *GHz*.

Electrical field (E-filed) distribution patterns on the resonator are shown in Figure 2.11, where the resonance frequency f_a = 4.20 *GHz*.

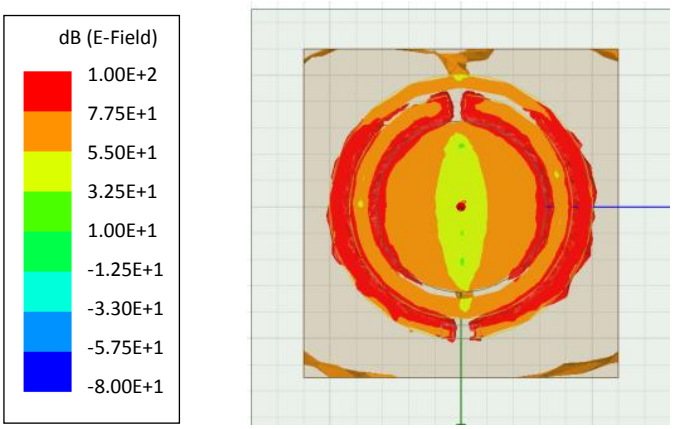

Figure 2.11. Electrical field (E-field) distribution on the resonator when the resonant at frequency f_a = 4.20 *GHz* and the electrical field concentrated on the outer ring.

As shown in Figure 2.11, the primary E-field distribution concentrated mainly on outer-ring (circular loop) at the resonant frequency, f_a = 4.20 *GHz*.

Surface-current (J-surf) distribution patterns of the double-ring resonator are shown in Figure 2.12, where the resonance frequency equals 2.19 *GHz*.

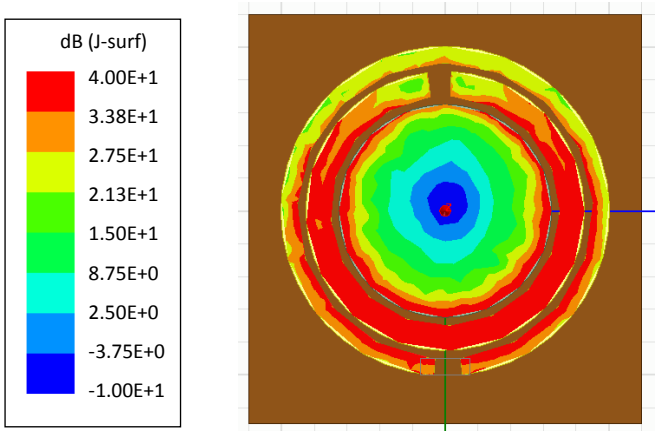

Figure 2.12. Surface-current (J-surf) distribution pattern when the resonant at frequency f_b = 2.19 *GHz* and the surface current concentrated on the inner ring.

As shown in Figure 2.12, the surface-current distribution concentrated mainly on the inner-ring (split ring) at f_b = 2.19 *GHz*.

The surface-current (J-surf) distribution patterns of the double-ring resonator are shown in Figure 2.13, where the resonance frequency equals 4.20 *GHz*.

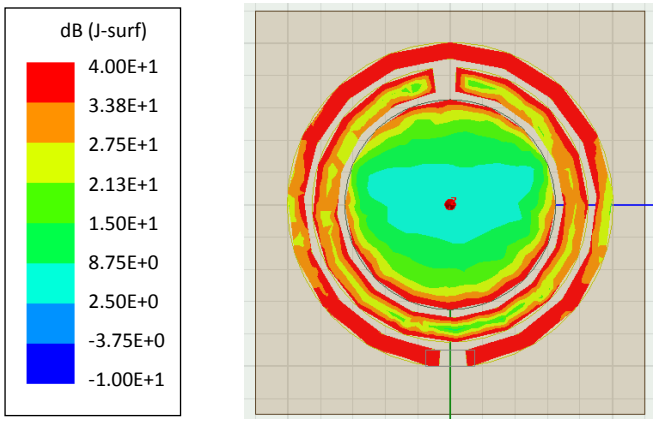

Figure 2.13. Surface-current (J-surf) distribution pattern when the resonant at frequency f_b = 4.20 *GHz* and the surface current concentrated on the outer ring.

As shown in Figure 2.13 the primary E-field distribution concentrated mainly on outer-ring (circular loop) at f_a = 4.20 *GHz*.

Magnetic field strength (H-field) distribution patterns of the double-ring resonator are shown in Figure 2.14, where the resonance frequency equals 2.19 *GHz*.

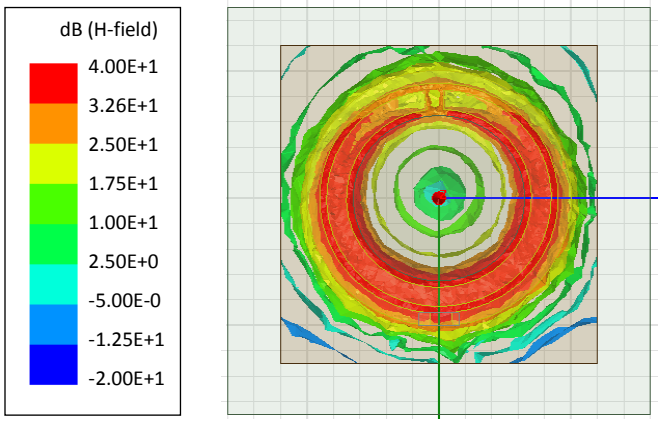

Figure 2.14. Magnetic field strength (H-field) distribution pattern when the resonant at frequency f_b = 2.19 *GHz* and the magnetic field concentrated on the inner ring.

As shown in Figure 2.14, the magnetic field distribution concentrated mainly on the inner-ring (split ring) at f_b = 2.19 *GHz*.

The magnetic field strength (H-field) distribution patterns of the resonator are shown in Figure 2.15, where the resonance frequency equals 4.20 *GHz*.

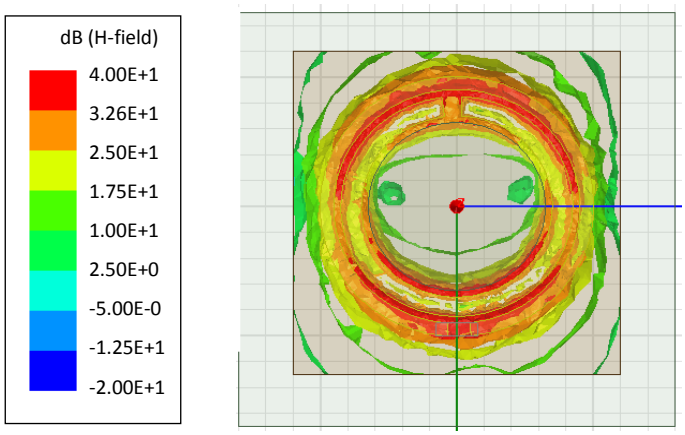

Figure 2.15. Magnetic field strength (H-field) distribution pattern when the resonant at frequency f_b = 4.20 *GHz* and the magnetic field concentrated on the outer ring.

As shown in Figure 2.15, the magnetic field distribution concentrated mainly on outer-ring (circular loop) at f_a = 4.20 *GHz*.

The electrical field, the surface-current, and the magnetic field strength have complicated distribution patterns. However, all electromagnetic field distributions concentrated mainly on the inner ring at the resonant frequency at 2.19 *GHz* and concentrated mainly on the outer ring at the resonant frequency at 4.20 *GHz*. Electromagnetic field distribution patterns demonstrate that the resonator can be used as a sensitive sensor with two resonant frequencies for measurements when samples are placed on top of the sensor.

F. Frequency Characteristics of the Double-ring Resonator

Substituted the resonant frequency (f_a=4.2 *GHz*) of the outer ring in the non-uniform dielectrics and the resonant frequency (f_{a0}=5.8 *GHz*) in free space into Eq.(2.15), the effective relative permittivity is calculated to be ε_{a_eff} = 1.91. Substituted the resonant frequency (f_b=2.19 *GHz*) of the inner ring in the non-uniform dielectrics and the resonant frequency (f_{b0}=2.9 *GHz*) in free space into Eq.(2.16), the effective relative permittivity is calculated to be ε_{b_eff} = 1.75.

The circuit *Q* factor of the resonator is defined [162] as follows.

$$Q = \frac{f}{BW} \tag{2.19}$$

where Q is the quality factor of the sensor circuit, f is resonant frequency, BW is 3dB bandwidth.

The simulation results by the electromagnetic finite-element method have shown the resonant frequency of the outer ring is 4.20 *GHz* and the resonant frequency of the inner ring is 2.19 *GHz*. At the two resonant frequencies, the return loss S_{11}, and 3dB bandwidth are obtained from the simulation results, and Q factor of the double-ring resonator are compared and listed in Table 2.3.

Table 2.3. Effective relative permittivity, frequency sensitivity, 3dB bandwidth, and Q factor of the double-ring resonator.

Double-ring resonator	Resonant frequency (*GHz*)	Effective relative permittivity	Frequency sensitivity $d(f)/d(\varepsilon_{eff})$ (*GHz*)	S_{11} (dB)	3dB bandwidth (*GHz*)	Q factor
Outer ring	f_a =4.2	ε_{a_eff} = 1.91	-9.7c0$\varepsilon_{a_eff}^{(-3/2)}$	-22.7	1.44	2.9
Inner ring	f_b =2.19	ε_{b_eff} = 1.75	-4.8c0$\varepsilon_{b_eff}^{(-3/2)}$	-31.1	0.51	4.3

As listed in Table 2.3 and shown in Figure 2.6, the circuit's Q factor at the inner ring resonance is higher than at the outer ring. However, the frequency sensitivity of the outer ring resonance is more sensitive to the effective relative permittivity than the inner ring. Because relative permittivity of the human body will change with hydration loss, the double-ring resonator can be used as a double-resonance sensor for monitoring human-body dehydration. Following will analyze the double-resonance sensor by the equivalent circuit method.

2.3 S_{11} Equivalent Circuit of the Double-Resonance Sensor

Using the equivalent circuit method [164 - 166], the double-resonance sensor can be described as an electrical circuit. In this section, the equivalent circuit of the sensor is modeled.

The circuit parameters and the resonant frequencies of the sensor are deduced. Simulation result of the equivalent circuit by the Matlab/Simulink software is compared with the electromagnetic finite-element simulation and experiment result.

A. S_{11} Equivalent circuit model

The Resonant frequency of the double-resonance sensor in the lumped-element electromagnetic model has an infinite periodic expression. The Matlab/Simulink software can be used to construct an equivalent circuit model of the double-resonance sensor when the frequency range is set within 6 *GHz*. It should be emphasized that the equivalent circuit is only valid in the frequency range of 6 *GHz* to simulate the double-resonance sensor. A Simulink equivalent circuit model of the sensor is shown in Figure 2.16.

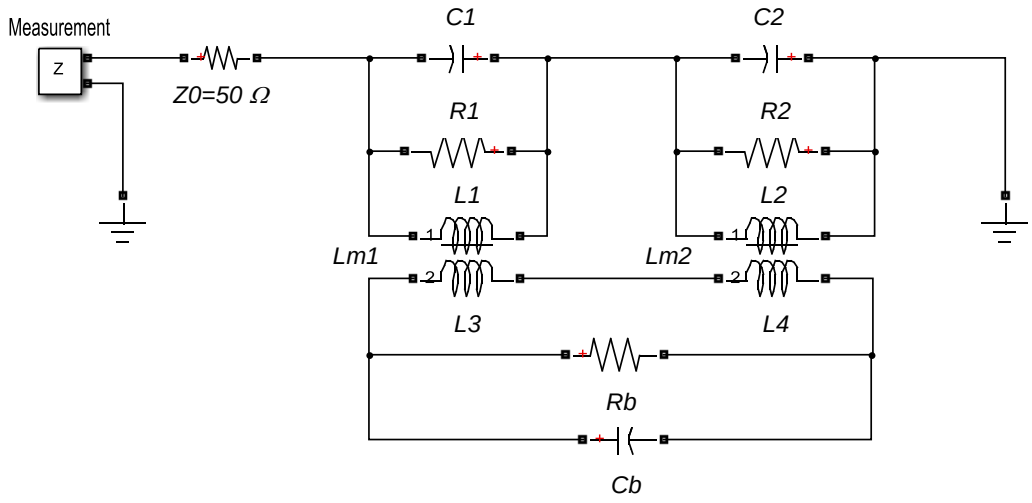

Figure 2.16. Equivalent circuit model of the double-resonance sensor in Matlab/Simulink window.

In the equivalent circuit model, L_1, L_2, C_1, C_2, R_1, and R_2, are the outer ring parameters. L_3, L_4, and C_b, R_b are the inner-ring parameters. Induced voltages in the two rings of the sensor

are magnetically coupled by mutual inductances. Hence, the magnetic couplings between the rings are modeled by the mutual inductances, L_{m1} and L_{m2}. In the model, Z_0 is reference impedance. The block "z" in the model is a measurement unit in the Matlab/Simulink software which is used to measure the impendence of the circuit. Due to only simulating the resonant frequencies within the measurement range of 6 *GHz* and the outer ring's dimension is $\lambda+\lambda/4$ as described in Eq.(2.1), the space dimension of the outer ring is reasonably divided into two sections by the wavelength ratio, i.e., $\lambda : \lambda/4 = 0.8 : 0.2$. According to the divided ratio of ring dimension, the inductances and mutual inductances in the equivalent circuit model are listed in Table 2.4.

Table 2.4. Inductances and mutual inductances of the equivalent circuit model.

L_1:L_2 = $\lambda : \lambda/4$	L_{m1}:L_{m2} = $\lambda : \lambda/4$	L_3:L_4 = $\lambda : \lambda/4$
L_1=0.8 L_a	L_{m1}=0.8 L_m	L_3=0.8L_b
L_2=0.2 L_a	L_{m2}=0.2 L_m	L_4=0.2L_b

where L_a is the inductance of the outer ring, L_b is the inductance of the inner ring, L_{m1} and L_{m2} are the mutual inductances between the outer ring and the inner ring.

B. Resonant frequencies of the equivalent circuit

To find the S_{11} resonant frequencies of the equivalent circuit, set $R_1 = R_2 = R_b = \infty$, because various resistors in the equivalent circuit do not affect the resonant frequencies. Substituted $L_1 = 0.8L_a$, $L_2 = 0.2L_a$, $L_{m1} = 0.8L_m$, $L_{m2} = 0.2L_m$, $L_3 = 0.8L_b$, $L_4 = 0.2L_b$, and $L_m = k$ sqrt(L_aL_b) into the equivalent circuit, where k is the coupling coefficient and ω is angular frequency. Using the Symbolic Math Toolbox of Matlab, impendence Z of the equivalent circuit as shown in Figure 2.16 is expressed as follows.

$$Z = Z_0 + \frac{25j\omega L_a\left(25-4(C_1+C_2)L_a\omega^2\right)\left(1-C_bL_b\omega^2+C_bL_bk^2\omega^2\right)}{B} \qquad (2.20)$$

where

$$B = 16C_bL_b(C_1+C_2)^2L_a^2k^2\omega^6 - 16C_bL_b(C_1+C_2)^2L_a^2\omega^6 + 16(C_1+C_2)^2L_a^2\omega^4 - 325(C_1+C_2)C_bL_aL_bk^2\omega^4 + 425(C_1+C_2)C_bL_aL_b\omega^4 - 425(C_1+C_2)L_a\omega^2 - 625C_bL_b\omega^2 + 625$$

Transfer the impendence Z into the return loss S_{11} by the following equation.

$$S11 = \frac{Z-50}{Z+50} \tag{2.21}$$

Substituted the measurement reference impedance Z_0 = 50 into Eq.(2.20) and let S_{11} = 0 in Eq.(2.21), the angular frequency ω has two symbolic solutions as follows.

$$\omega_a = \frac{5}{2\sqrt{(C_1+C_2)L_a}} \tag{2.22}$$

$$\omega_b = \frac{1}{\sqrt{C_bL_b(1-k^2)}} \tag{2.23}$$

where ω_a is the resonant angular frequency of the outer ring and ω_b is the resonant angular frequency of the inner ring.

Let equivalent capacitor $C_a = C_1 + C_2$ and $\omega_a = 2\pi f_a$ and $\omega_b = 2\pi f_b$ in Eq.(2.22) and Eq.(2.23), the resonant frequency f_a and f_b are as follows.

$$f_a = \frac{5}{4\pi\sqrt{C_aL_a}} \tag{2.24}$$

$$f_b = \frac{1}{2\pi\sqrt{C_bL_b(1-k^2)}} \tag{2.25}$$

where k is set as 0.8 in this circuit, the capacitor C_a is an outer-ring equivalent capacitor in the equivalent circuit, and C_b is an inner-ring equivalent capacitor.

C. Calculating the inductances and the equivalent capacitances of the equivalent circuit

Inductances of the two rings can be calculated [167] as follows.

$$L = \mu_0 r\left[ln\left(\frac{8r}{w+h}\right) - 1/2\right] \tag{2.26}$$

where L is the ring inductance, r is the radius of the ring, w is the strip width, h is the strip thickness, μ_0 is the free-space permeability.

Substituted the average radius of outer ring r = 0.0105 m, the strip width w = 0.001 m, the strip thickness h = 0.000025 m, and the free-space permeability μ_0=4π×1e-7 H/m into Eq.(2.26), the inductance of outer ring equals L_a = 5.15e-08 H. Substituted the average radius of inner ring r = 0.0085 m, the strip width w = 0.0015 m and the strip thickness h = 0.000025 m into Eq(2.26), the inductance of inner ring equals L_b = 3.52e-08 H.

Employing the frequency expressions of the lumped-element electromagnetic model in section II and the frequency expressions of the equivalent circuit model, capacitances of the two rings can be inferred as follows.

Let Eq.(2.11) equals Eq.(2.22) and, the following equation is obtained.

$$\frac{c_0(1+1/4)}{(2\pi r_a - g_a)\sqrt{\varepsilon_{a\_eff}}} = \frac{5}{4\pi\sqrt{C_a L_a}} \tag{2.27}$$

The capacitance, C_a in Eq.(2.27) has the following solution.

$$C_a = \frac{\varepsilon_{a\_eff}\left(\frac{2\pi r_a - g_a}{\pi c_0}\right)^2}{L_a} \tag{2.28}$$

The capacitance C_a of the outer ring can be calculated by the ring dimension and relative permittivity, where L_a is the function of the ring dimension as expressed in Eq.(2.26). Substituted the effective relative permittivity ε_{a_eff} = 1.91 as listed in Table 2.3 and the outer-ring dimension as listed in Table 2.1 into Eq.(2.28), the outer-ring capacitance in the equivalent circuit C_a = 1.72e-13 F.

Let Eq.(2.12) equals Eq.(2.23), the following equation is obtained.

$$\frac{c_0}{2(2\pi r_b - g_b)\sqrt{\varepsilon_{b\_eff}}} = \frac{1}{2\pi\sqrt{C_b L_b(1-k^2)}} \tag{2.29}$$

The capacitance, C_b in Eq.(2.29) has the following solution.

$$C_b = \frac{\varepsilon_{b\_eff}\left(\frac{(2\pi r_b - g_b)}{\pi c_0}\right)^2}{L_b(1-k^2)} \quad (2.30)$$

The capacitance C_b of the inner ring can be calculated only by the ring dimension and relative permittivity.

Substituted the effective relative permittivity ε_{b_eff} = 1.75 as listed in Table 2.3 and the inner-ring dimensions as listed in Table 2.1 into Eq.(2.30), the inner-ring capacitance in the equivalent circuit C_b = 4.15e-13 *F*.

D. Simulations and experiment results of the double-resonance sensor

Following parameters in the equivalent circuit model are used for the simulation studies.

L_a = 5.15e-08 *H*

L_b = 3.52e-08 *H*

$L_1 = 0.8L_a$

$L_2 = 0.2L_a$

$L_3 = 0.8L_b$

$L_4 = 0.2L_b$

C_a = 1.72e-13 *F*

C_b = 4.15e-13 *F*

$C_1 = 0.9C_a$

$C_2 = 0.1C_a$

R_a = 1e5 Ω

R_b = 5e4 Ω

$R_1 = 0.2R_a$

$R_2 = 0.8R_a$

Z_0 = 50 Ω

The mutual inductances used in the equivalent circuit model are,

$L_{m1} = k\ \mathrm{sqrt}(L_1 L_3) = 3.4086\text{e-}08\ H$

$L_{m2} = k\ \mathrm{sqrt}(L_2 L_4) = 8.5214\text{e-}09\ H$

$k = 0.8$

The prototype of the double-resonance sensor is connected to an SMA straight mounting subminiature coaxial microwave connector as shown in Figure 2.17, where SMA is the abbreviation of SubMiniature version A.

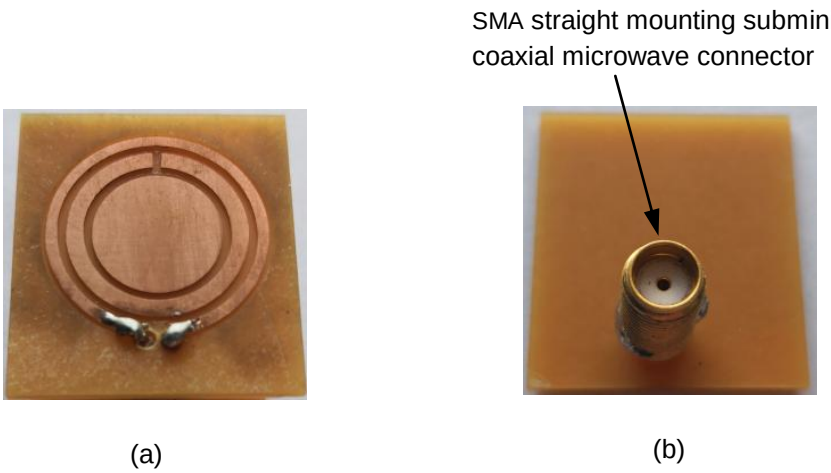

Figure 2.17. The prototype of the double-resonance sensor. (a) Topside of the sensor and (b) the backside of the sensor.

Return loss S_{11} of the double-resonance sensor was measured by a vector network analyzer (FieldFox N9923A). The measurement results are shown in Figure 2.18, where the sensor has an inner-ring resonance at 2.25 *GHz* and an outer-ring resonance at 4.17 *GHz*. The equivalent circuit model was simulated by Matlab software and the sensor has an inner-ring resonance at 2.19 *GHz* and an outer-ring resonance at 4.20 *GHz*. The lumped-element electromagnetic model was simulated by the finite-element method, which is shown in Figure

2.18 and the sensor has an inner-ring resonance at 2.19 *GHz* and an outer-ring resonance at 4.20 *GHz*.

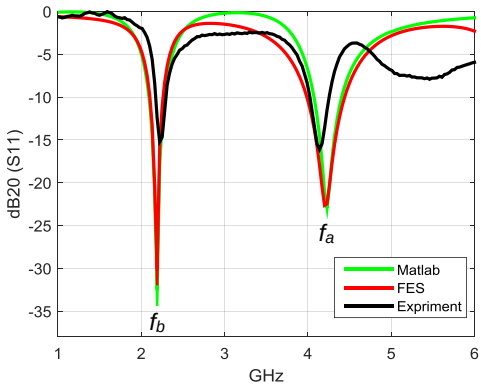

Matlab simulation result
f_b = 2.19 *GHz*
f_a = 4.20 *GHz*

Finite-element simulation result
f_b = 2.19 *GHz*
f_a = 4.20 *GHz*

Expriment results
f_b = 2.25 *GHz*
f_a = 4.17 *GHz*

Figure 2.18. The Matlab simulation result of the equivalent circuit (green line), the simulation result of the finite-element simulation (FES) (red line), and the experiment result (black line).

The simulation result of the equivalent circuit model by Matlab software is almost the same as the lumped-element electromagnetic model by the finite-element method. The two simulation results are close to the experiment result as shown in Figure 2.18. Hence, the electromagnetic finite-element model and the equivalent circuit model can be used for further simulation studies.

2.4 Simulation Studies of Identifying Various Materials

To show that the double-frequency sensor can measure and identify the materials with various relative permittivities, a 3-D finite-element sample component was placed on the sensor as shown in Figure 2.19. Assigned the sample component with various relative permittivities, the measurement and identification were simulated by the electromagnetic finite-element model as described in section 2.2 and was simulated by the equivalent circuit model as described in section 2.3. The sample diameter is 60 *mm*, high is 15 *mm*, and the gap between the sample and

the sensor is 0.5 *mm*. Four materials were selected for the simulation studies. They are Teflon with relative permittivity as 2.1, silicon dioxide with relative permittivity as 4, the human muscle with relative permittivity as 57.7 [168], and water with relative permittivity as 81.

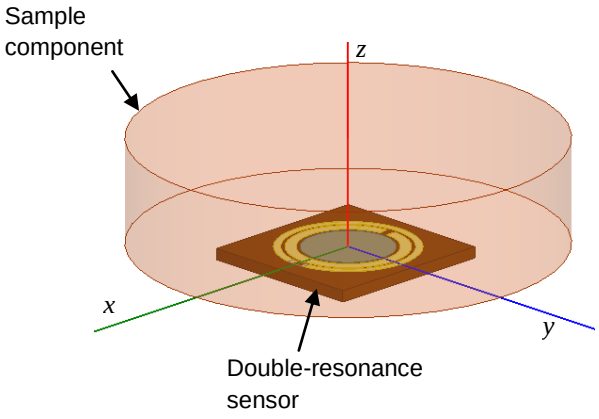

Figure 2.19. A 3-D finite-element simulation model for measuring and identifying various materials. The sample component was placed on the sensor with 60 mm diameter, 15 mm height, and 0.5mm gap between the sample and the sensor.

The simulation results of various materials on the sensor by the electromagnetic finite-element method are shown in Figure 2.20.

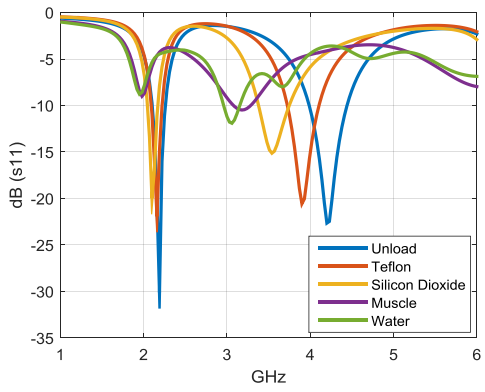

Material	Resonant frequency (*GHz*)	
	f_a	f_b
Unload	4.20	2.19
Teflon	3.90	2.16
Silicon dioxide	3.54	2.10
Muscle	3.16	1.98
Water	3.06	1.95

Figure 2.20. The sensor simulation results by the electromagnetic finite-element method.

Using the resonant frequencies obtained from the simulation results, the effective relative permittivities of various material samples can be obtained by Eq.(2.15) and Eq.(2.16). Using the effective relative permittivities, the equivalent capacitances, C_a and C_b, can be obtained by Eq.(2.28) and (2.30), respectively. Substituted the capacitances into the equivalent circuit model, the simulation results of various materials on the sensor by Matlab/Simulink software are shown in Figure 2.21. The resonant frequencies obtained by the equivalent circuit model are the same as the electromagnetic finite-element model.

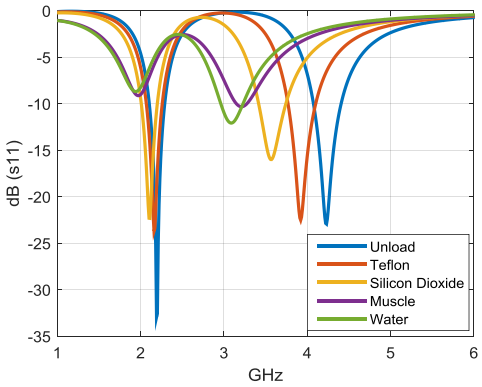

Material	Resonant frequency (*GHz*)	
	f_a	f_b
Unload	4.20	2.19
Teflon	3.90	2.16
Silicon dioxide	3.54	2.10
Muscle	3.16	1.98
Water	3.06	1.95

Figure 2.21. The sensor simulation results by the Matlab/Simulink equivalent circuit.

The material name, relative permittivity, and the resonant frequencies from the simulation studies are listed in Table 2.5.

Table 2.5. Various material samples, relative permittivity, and resonant frequencies.

Material samples	Relative permittivity ε	Resonant frequency (*GHz*)	
		f_a	f_b
Unload	1.0	4.20	2.19
Teflon	2.1	3.90	2.16
Silicon dioxide	4.0	3.54	2.10
Muscle	57.7	3.16	1.98
Water	81.0	3.06	1.95

As relative permittivity of the sample increases, the two resonant frequencies decrease as listed in Table 2.5.

For data classification and material identification, the two resonant frequencies for each measurement are projected in a 2-D space with a clear expression as shown in Figure 2.22.

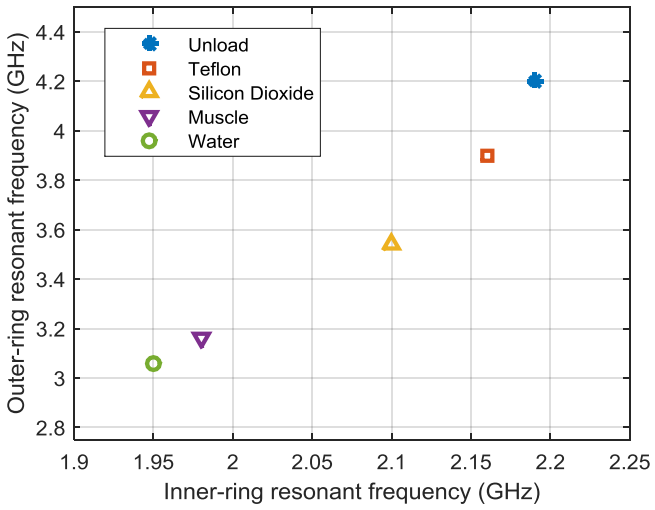

Figure 2.22. Resonant frequencies of inner and outer rings are projected in a 2-D space.

Employing the simulation results as listed in Table 2.5, the relative permittivities of various samples can be plotted by the two resonant frequencies. As shown in Figure 2.23, the outer-ring resonant frequency is more sensitive to the relative permittivity of the material than the inner ring. However, the resonant curves of the inner ring are shaper than the outer ring as shown in Figure 2.21.

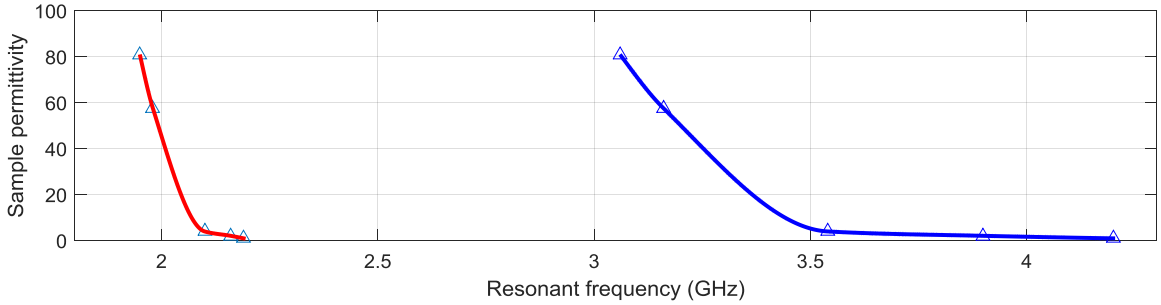

Figure 2.23. The relative permittivities of various samples are plotted by the resonant frequencies of the inner (red line) and the outer rings (blue line).

In practical applications of material identification, if a similar relationship as shown in Figure 2.23 can be found by experiments, the relative permittivities of various samples can be identified by the resonant frequencies of the double-resonance sensor.

2.5 Temperature Dependences of the Sensor

Temperature dependences of the relative permittivity have been reported in the literature [169 - 171]. For different materials, some experiments showed the complexity that the relative permittivity may increase or may decrease with increasing temperature [169 - 171]. When temperature changed, the relative permittivity of the printed circuit board (PCB) material will change and the effective relative permittivity of the double-resonance sensor will change. Due to the resonant frequencies depending on the effective relative permittivity as shown in Eq.(2.11) and Eq.(2.12), the double-resonance sensor is sensitive to the temperature changes. The temperature dependence of the sensor was investigated.

The sensor was fixed on a support and in unloading condition. A hot air blower was used to heat the sensor and an infrared thermometer was used to monitor the surface temperature of the sensor. When the sensor was heated from 25 C° to 50 C°, the two resonant frequencies f_a and f_b of the double-resonance sensor were measured by a vector network analyzer (FieldFox N9923A). The measurement results are summarized in Table 2.6.

Table 2.6. Temperature dependence of the sensor.

Temperature (C°)	f_b **(*GHz*)**	f_a **(*GHz*)**
25	4.18	2.26
30	4.15	2.24
35	4.13	2.22
40	4.12	2.21
45	4.11	2.20
50	4.10	2.19

In 25 C° - 50 C° range, the resonant frequencies depend on the temperature of the sensor has been investigated. For precise measurement, the relationship of the temperature and resonant frequencies may be used to compensate the measurement results when the ambient temperature changed. However, the relative permittivity of the measured object such as meat may change with temperature varies [172], which will reduce the measurement accuracy. Hence, the temperature is a complex factor for the sensor and measured object in a more accurate measurement.

When the double-resonance sensor is placed on the human body as a wearable biomedical sensor, the temperature of the sensor changes only in a limited range, because humans can maintain a relatively constant temperature. In this case, the measurement accuracy is less dependent on the temperature. In order to verify the validity and practicality of sensor, meat humidity levels were identified by the sensor prototype. For simplifying the test conditions, the temperature was a constant in the following experiments.

2.6 Double-resonance Sensor Experiments for Identifying Meat Humidity

To demonstrate the dehydration-related applications of the double-resonance sensor, meat humidity was to be identified. The pork meat was wrapped in plastic film and was placed under the sensor. The meat dimension is about 180 *mm* $\times$ 100 *mm* $\times$ 40 *mm*. As shown in Figure 2.24, a transparent film with 0.2 *mm* thickness was placed between the sensor and the meat for electrical isolation. Deionized (DI) water was injected in a region of the meat. Approximate radius and height of the region are 15 *mm* and 10 *mm*, respectively, and volume of the region is about 7069 mm^3. DI water was injected into the region to simulate various humidity levels of the meat. Measurements are taken after injecting 0.1 *ml* of DI water each time. The amount of DI water with respect to the meat's total volume within that region will increase about 1.4% after each injection. Because the relative permittivity of meat is 57.7 [168] and the relative permittivity of water is 81, with the injected water, the relative permittivity in the sensing region will increase. Consequently, the effective capacitances of the sensor will increase and the two resonant frequencies of the

sensor will decrease. Monitoring the resonant frequencies of the sensor, the meat humidity levels can be identified.

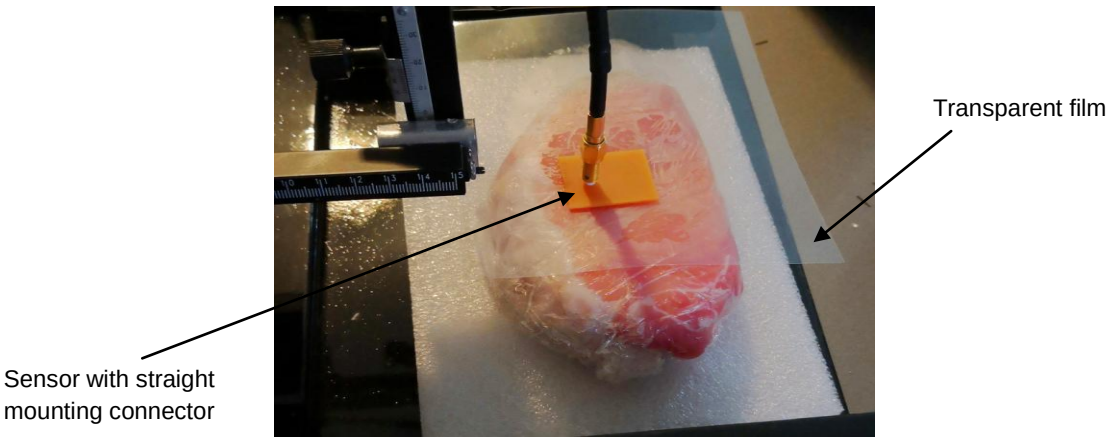

Figure 2.24. A strip of pork meat was wrapped in plastic film and isolated by a transparent film then placed under the sensor.

With the ambient temperature as 28 C°, the experiment results of measuring various humidity levels of the pork meat are shown in Figure 2.25 and the detail data is listed in Table 2.7.

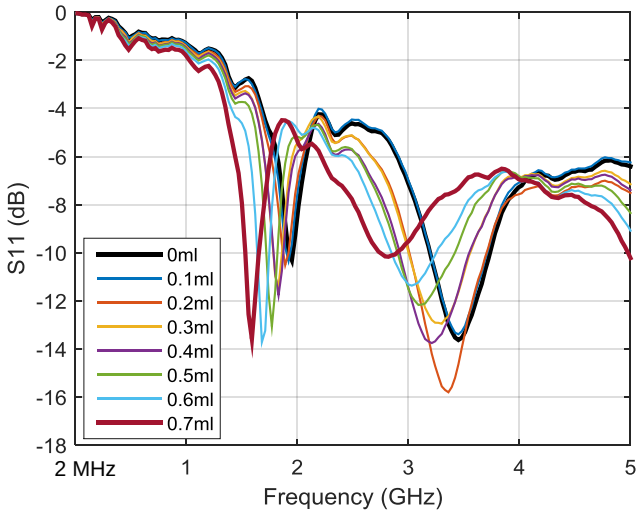

Figure 2.25. Various humidity levels of the pork meat and the S_{11} resonant frequencies.

With injecting water into the meat, the meat humidity increases and the two resonant frequencies clearly shifted from high to low.

Table 2.7. Experiment results with injected DI water in the meat region.

Injecting DI water	**DI water content in meat**	f_b **(*GHz*)**	f_a **(*GHz*)**
0 *ml* DI in meat	0.000 (0%)	1.95	3.45
0.1 *ml* DI in meat	0.014 (1.4%)	1.92	3.45
0.2 *ml* DI in meat	0.028 (2.8%)	1.89	3.36
0.3 *ml* DI in meat	0.042 (4.2%)	1.83	3.27
0.4 *ml* DI in meat	0.057 (5.7%)	1.83	3.21
0.5 *ml* DI in meat	0.071 (7.1%)	1.77	3.12
0.6 *ml* DI in meat	0.085 (8.5%)	1.68	3.03
0.7 *ml* DI in meat	0.099 (10%)	1.59	2.82

For clearly expressing the humidity levels of the meat, the two resonant frequencies for each measurement are projected in 2-D space as shown in Figure 2.26.

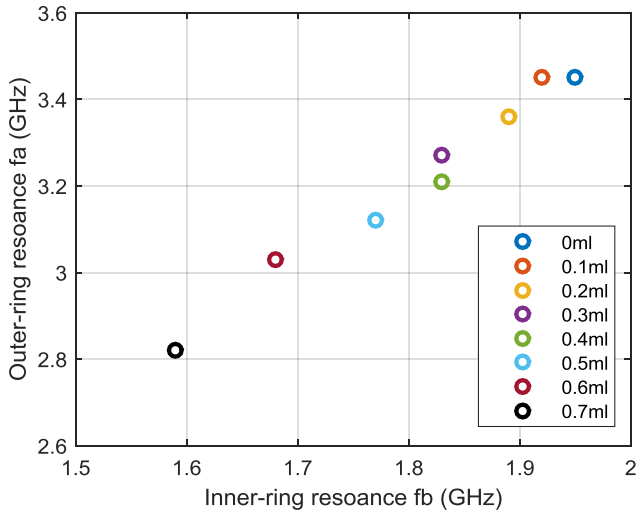

Figure 2.26. Humidity levels in the meat are expressed in 2-D space by the two resonant frequencies.

At inner-ring resonance, the maximum shift of the resonant frequency was 0.36 *GHz* when DI water was injected in the meat from 0 *ml* to 0.7 *ml*. At outer-ring resonance, the maximum shift of the resonant frequency was 0.63 *GHz* when DI water was injected in the meat from 0 *ml* to 0.7 *ml*. The experiment results demonstrate that the new double-resonance sensor is available for identifying humidity in meat and may be developed for a wearable sensor to monitor human body dehydration.

2.7 Experiments with Extended Connection Lines for Identifying Meat Humidity

More experiment results are investigated for identifying meat humidity using extended connection lines to the double-resonance sensor. For connecting to an SMA edge mounting subminiature coaxial microwave connector, the double-resonance sensor was extended by 15 *mm* connection lines to the edge mounting connector as shown in Figure 2.27(a). The extended connection lines contribute the additional inductance and capacitance to the double-resonance sensor, which will reduce the resonant frequencies of the double-resonance sensor. Simulation result of the electromagnetic finite-element simulation (FES) and the experiment result as shown in Figure 2.27(b).

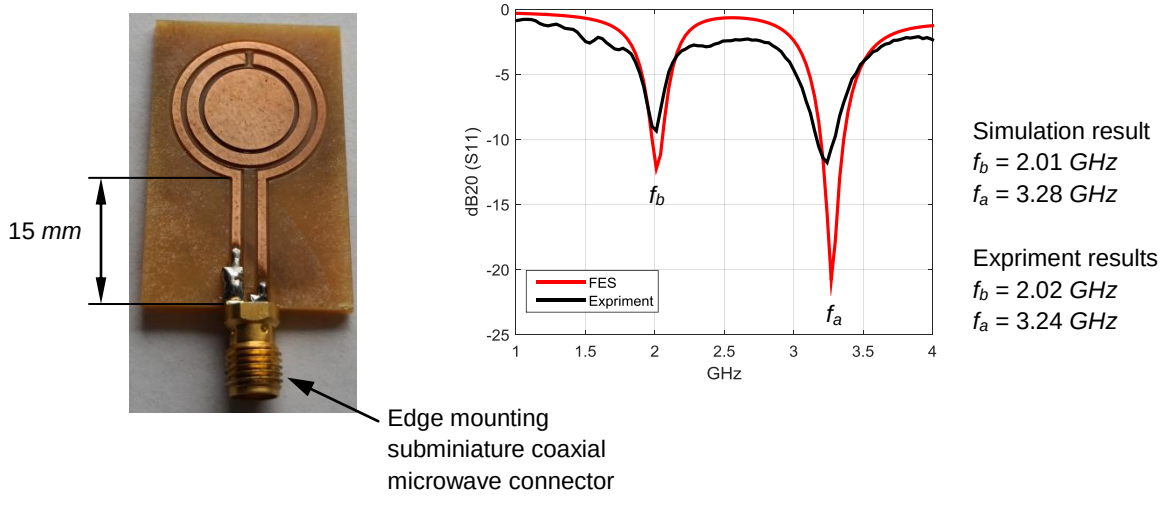

(a) (b)

Figure 2.27 (a) Double-resonance sensor was extended by 15 *mm* connection lines for connecting to an edge mounting subminiature coaxial microwave edge mounting connector. (b) Results of the finite-element simulation (FES) (red line) and the experiment results (black line).

In Figure 2.27 (b), the experiment result shows the inner-ring resonance at 2.02 *GHz* and the outer-ring resonance at 3.24 *GHz*, while the finite-element simulation result shows the inner-ring resonance at 2.01 *GHz* and the outer-ring resonance at 3.28 *GHz*. Hence, the experiment result is close to the simulation result.

In order to analyze the load impedances when the sensor resonances at the two resonant frequencies, the S_{11} Smith chart was plotted in Figure 2.28 by the electromagnetic finite-element simulation and the prime center of the Smith chart is assigned with a value of 50 Ω.

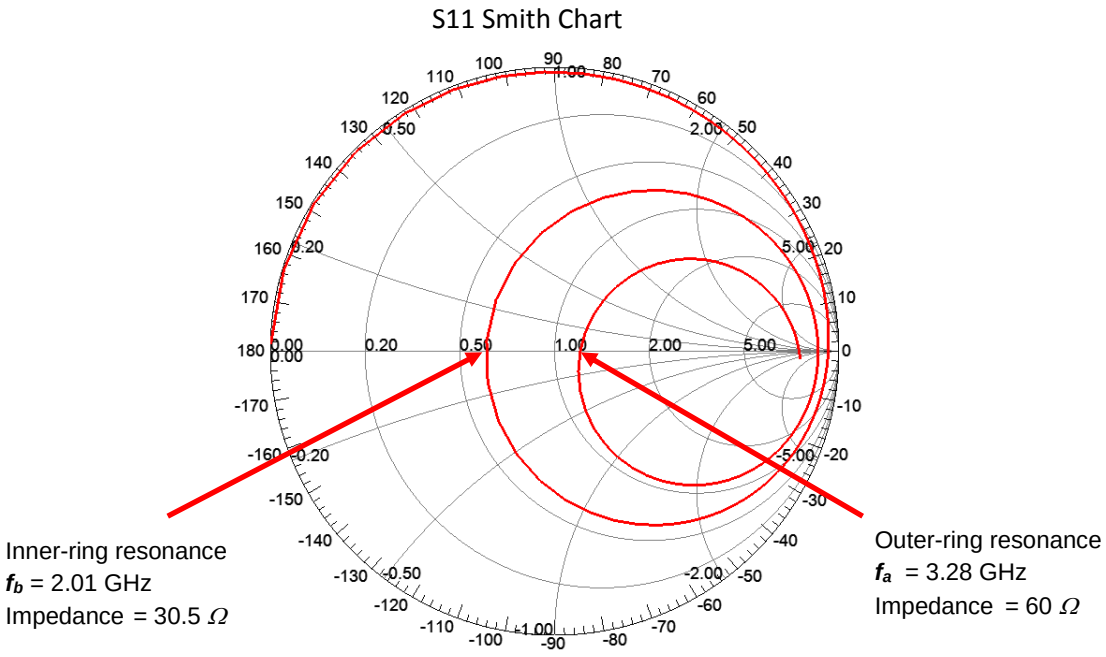

Figure 2.28. S_{11} Smith chart plots by the electromagnetic finite-element simulation, where f_a is the outer-ring resonant frequency; f_b is the inner-ring resonant frequency.

As shown in Figure 2.28, the outer-ring resonant frequency f_a is 3.28 *GHz* and the load impedance at the frequency is 60 Ω, while the inner-ring resonant frequency f_b is 2.01 *GHz* and the load impedance at the frequency is 30.5 Ω.

The pork meat was wrapped in plastic film and was placed on the sensor. The meat size is about 200 *mm* $\times$ 100 *mm* $\times$ 40 *mm*. As shown in Figure 2.29, a transparent film with 0.2 *mm* thickness was placed between the sensor and the meat. Deionized (DI) water was injected into a region of the meat. Approximate radius and height of the region are 15 *mm* and 10 *mm*, respectively, and the region volume is about 7069 mm^3. The region simulates various humidity levels of the meat. Measurements are taken after injecting 0.1 *ml* of DI water each time. The amount of DI water with respect to the meat's total volume within that region will increase about about 1.4% after each injection.

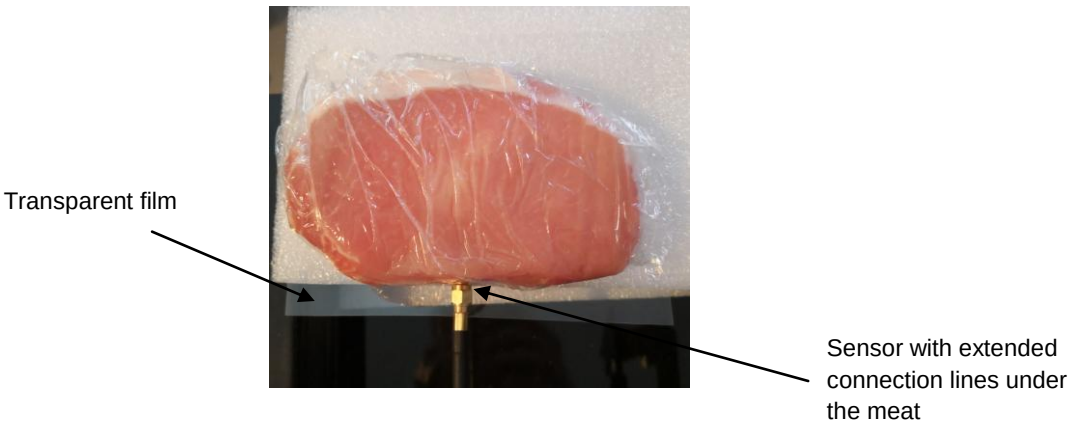

Figure 2.29. A strip of pork meat was wrapped in plastic film and was isolated by a transparent film then placed on the sensor with extended connection lines.

Using the double-resonant sensor with extended connection lines, the experiment results of measuring various humidity levels of the pork meat are shown in Figure 2.30 and the ambient temperature as 28 C°.

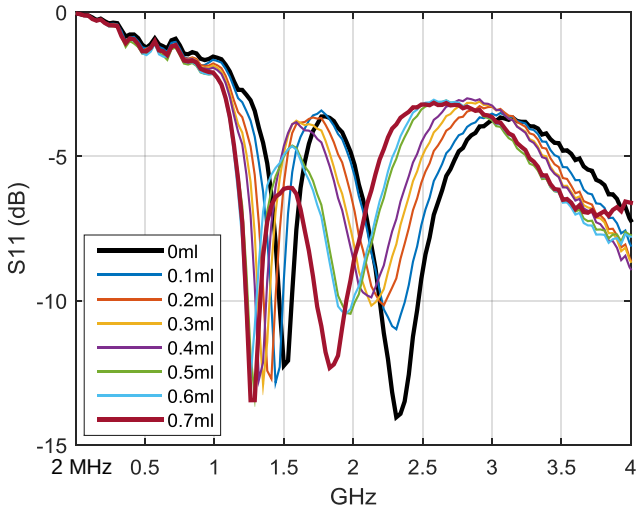

Figure 2.30. The humidity of the pork meat and the S_{11} resonant frequencies by the double-resonant sensor with extended connection lines.

With injecting water into the meat, the meat humidity increases and the two resonant frequencies shifted from high to low as shown in Figure 2.30. The detailed data is listed in Table 2.8.

Table 2.8. Using the sensor with extended connection lines, the experiment results with injected DI water in the meat region.

Injecting DI water	**DI water content in meat**	f_b **(*GHz*)**	f_a **(*GHz*)**
0 *ml* DI in meat	0.000 (0%)	1.50	2.31
0.1 *ml* DI in meat	0.014 (1.4%)	1.44	2.31
0.2 *ml* DI in meat	0.028 (2.8%)	1.41	2.22
0.3 *ml* DI in meat	0.042 (4.2%)	1.35	2.13
0.4 *ml* DI in meat	0.057 (5.7%)	1.32	2.13
0.5 *ml* DI in meat	0.071 (7.1%)	1.29	1.98
0.6 *ml* DI in meat	0.085 (8.5%)	1.26	1.95
0.7 *ml* DI in meat	0.099 (10%)	1.26	1.83

For clearly expressing the humidity levels of the meat, the two resonant frequencies for each measurement are projected in a 2-D space as shown in Figure 2.31.

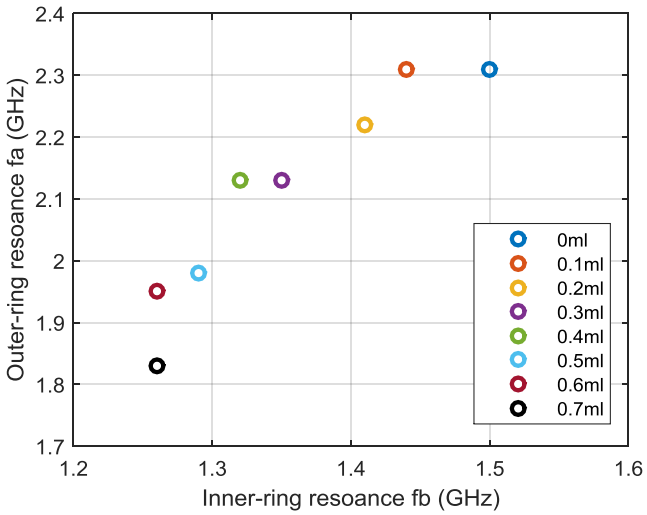

Figure 2.31. Humidity levels in the meat are expressed in 2-D space by the two resonant frequencies.

Comparing the two experimental results as listed in Table 2.7 and listed in Table 2.8, the original double-resonance sensor has a larger frequency shift than the sensor with the extended connection lines.

At inner-ring resonance of the original double-resonance sensor, the maximum shift of the resonant frequency is 0.36 *GHz* when DI water was injected in the meat from 0ml to 0.7 *ml*, while it is 0.24 *GHz* by the sensor with the extended connection lines. At outer-ring resonance of the original double-resonance sensor, the maximum shift of the resonant frequency is 0.63 *GHz* when DI water was injected in the meat from 0 *ml* to 0.7 *ml*, while it is 0.36 *GHz* by the sensor with the extended connection lines. The comparisons demonstrate that the original double-resonance sensor is more sensitive to the meat humidity changing than the sensor with the extended connection lines.

2.8 Conclusions

A new double-resonance sensor was designed and fabricated. The sensor has two type rings and a center pad. The outer ring was designed as the circular-loop type and the inner ring was designed as the split-ring type. The two different rings contribute to a larger resonant-frequency span over 2 *GHz* for the sensor. A center pad is added with suitable dimension, the port impedance can approach to 50 Ω, hence boosting the *Q* factor of the circuit. The waveguide method and the electromagnetic finite-element simulation were used to design the sensor. The equivalent circuit was deduced and was simulated by Matlab/Simulink software to reveal the electrical parameters of the sensor. Various electromagnetic field distribution patterns show that the resonator is available for use as a sensor. Experiments of identifying pork-meat humidity verified that the sensor has a promising approach for monitoring human body dehydration. Furthermore, multiple resonant frequencies can be designed to provide a more accurate identification parameters in a multi-dimensional vector data space. The double-resonance sensor can be used as a wearable biomedical sensor for monitoring human-body hydration loss, and potentially used for identification of abnormal or cancerous tissues based on their dielectric properties.

CHAPTER 3

WEARABLE MEDICAL SENSOR WITH WIRELESS BODY AREA NETWORK FOR INTRAOPERATIVE NEUROMONITORING

3.1 Introduction

Intraoperative neuromonitoring (IONM) system is commonly used to monitor the neural responses of a patient body during general spine and cranial procedures [173, 174]. Transcranial motor evoked potential (TcMEP) is an electrical signal of muscular action caused by transcranial brain stimulation [175, 176]. The TcMEP has become the most popular method to monitor the functional integrity of the motor system during surgery [175] and was applied to perform intraoperative monitoring over 25 years [177]. During the scoliosis correction surgeries at the Texas Scottish Rite Hospital for Children, an IONM system (Cadwell Industries, Inc.) is used to monitor the TcMEP signals during the surgical procedure to prevent injuries of the spinal column. To acquire a TcMEP signal [178], the stimulus pulse trains were applied to the patient's scalp through the pairs of Electroencephalography (EEG) electrode. The Cadwell TCS-1 stimulator (Cadwell Industries, Inc.) was used to generate the stimulus pulse trains. Each pulse width was 200 microseconds, the frequency was 350 *Hz*, and intensity was 400 *V*. Typically, 20 pairs of needle electrodes inserted into the limbs of a patient were used to record the TcMEP signals by the IONM system. When TcMEP signals from the limbs weaken or disappeared, the spinal column may be injured and the surgery has to be suspended until the signals restore. The practical TcMEP signal amplitude is smaller [175]. Depending on the positions of the needle electrode in the limbs, the practical TcMEP amplitude of peak to peak is from 100 *uV* up to 6 *mV* within large environment noises. Hence, the amplifier and filter hardware have to be integrated into the IONM system to amplify the signals and eliminate the noises. In the operating room, typically, 40 expensive lengthy wires are connected from the limbs of a patient to the IONM system. The wires crowd in the surgical area and are susceptible to electromagnetic interference (EMI) from power lines and high-power electronics such as thermal units and life support

equipment [179, 180]. Hence, complex digital signal processing is used in the IONM system to reduce the EMI noise and enhance signal readability for doctors. In order to improve the IONM system, a wireless communication system (Sichuan NeoSource BioTektronics inc.) was used to acquire the TcMEP signals with isolating the critical TcMEP signals from high-level EMI in the operating room.

Most of the wireless communications are implemented by Bluetooth, WiFi, ZigBee and wireless body area network (WBAN) following with the IEEE standards and protocols [5], according to the operating frequency, bandwidth and data rates. Comparing to other wireless devices, WBAN has the advantages of lower transmitter power, lower power consumption, and lower hardware cost [5]. The international WBAN standard is IEEE 802.15.6, which refers to the interconnecting devices used in close proximity around the body [6]. Commercially WBAN devices have found success owing to the increasing interest and functionality needs [7, 10]. Continuous and unhindered monitoring through WBAN communication becomes attractive for biomedical applications [10, 2, 9, 46].

In the chapter, a new WBAN is presented to acquire the TcMEP signals with compact size, low cost, high sample rate, and isolating critical TcMEP signals from high-level EMI in the operating room. The WBAN has four wireless modules which were placed at the limbs of a patient. In order to obtain enough TcMEP amplitudes for a normal measurement, usually, the stimulation pulse has to be larger than 200 V and less than 750 V for protecting the patient's nervous system. The effectiveness and reliability of four wireless modules have been evaluated by recording the TcMEP signals in the presence of high-level EMI found in the operating room [179, 180]. However, the hardware and software of the new WBAN system are different from the IONM system. Hence, the TcMEP waveforms recorded by the compact wireless modules are different from the complex IONM system. Because the TcMEP waveforms recorded by the IONM system has been considered to be the current gold standard by the medical community, the wireless recording must be converted to an equivalent IONM waveform for doctors. Although various signal conditioning methods are used, the IONM and the wireless module may be approximated as linear systems. Consequently, the linear system identification technique can be

employed to find a transfer function between the two systems. Using the found transfer function, the signals acquired by the WBAN can be converted to be fully acceptable waveforms by the doctors in the hospital.

3.2 Design of Wireless Module

Cooperated with Sichuan NeoSource BioTektronics inc., the wireless module (NEOSCBIO) was designed and improved as a wearable device for Intraoperative Neuromonitoring. The dimension of the module is 55 $mm \times 35\ mm \times 15\ mm$ and weight is only 30 g as shown in Figure 3.1(a). The system block diagram of wireless communication is shown in Figure 3.2. The wireless module includes a two-stage amplifier, an ultra-low-power Arm 32-bit microcontroller (STM32L433CC, STMicroelectronics) with a 12-bit as well as 12-kHz sampling rate analog-to-digital conversion, and a 3.7 V rechargeable lithium-ion battery. The battery life of 10 hours after it is fully recharged, which can meet the time of a complete scoliosis correction surgery. Wireless communication of the module was implemented by a 2.4-GHz transceiver (nRF24L01, Nordic Semi.), a built-in antenna, and a receiver of wireless USB dongle as shown in Figure 3.1(b). The USB dongle was connected to a host computer for recording data, while the real-time waveforms can display on the host computer with a graphical user interface. Wireless communication distance of the wearable module is over 10 m, which was measured in the operating room at the Texas Scottish Rite Hospital for Children. The wireless communication distance can meet the Intraoperative Neuromonitoring. The input ports of the wireless module were connected to two needle electrodes (Medtronic 945DSN1299) to acquire TcMEP signals in the muscles.

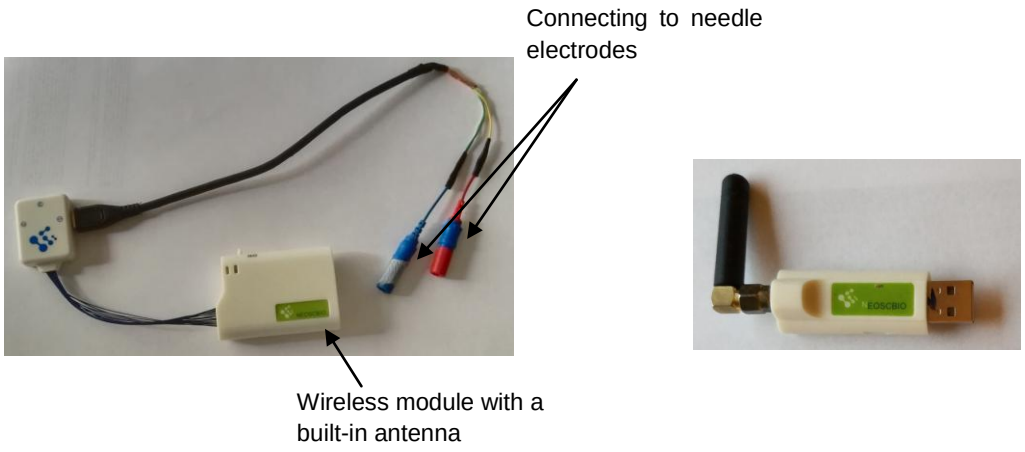

Figure 3.1. (a) Wireless module with 30 *g* weight and 55 *mm* × 35 *mm* × 15 *mm* dimension. (b) Wireless USB dongle.

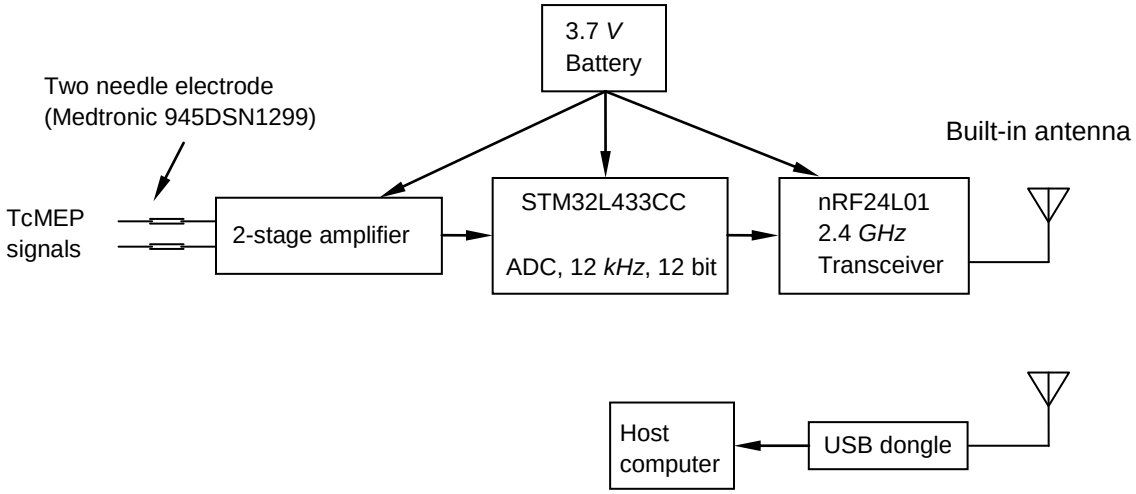

Figure 3.2. System block diagram of the wireless devices.

Due to the TcMEP signal is weak, a two-stage amplifier was designed to match the 3.3 *V* analog-to-digital converter of the microcontroller. The first stage uses an INA333 instrumentation amplifier with high common mode rejection ratio (CMRR of 100 *dB*) for reducing the common noises presented at both the recording and the reference electrodes. The amplifier has a high input impedance of approximately 100 *GΩ* and low input bias current of 200 *pA*. The second stage uses an OPA4330 amplifier with low offset voltage 50 *μV* and 35 *μA* of quiescent current.

Because the TcMEP amplitudes at hand, leg, and foot are different, the gains of the amplifiers were set as different values for accurately measuring at the various locations. In practice, the maximum TcMEP signal was about 6 *mV* at the abductor pollicis brevis muscle (at hand). Because the maximum output voltage of the amplifier must be less than 3.3 *V*, the total gain of the two-stage amplifier was designed as 500 with 10% gain margin for measuring the TcMEP at the hand muscle. The maximum TcMEP signal was about 1.5 *mV* at the tibialis anterior (at leg), the soleus (at leg), and the abductor hallucis (at foot). Because the maximum output voltage of the amplifier must be less than 3.3 *V*, the total gain was designed as 2000 with 10% gain margin for measuring the TcMEP at the leg and foot muscles.

When the input noise and device noise are considered, the gains and the noises of the two-stage amplifier can be described [188] in Figure 3.3.

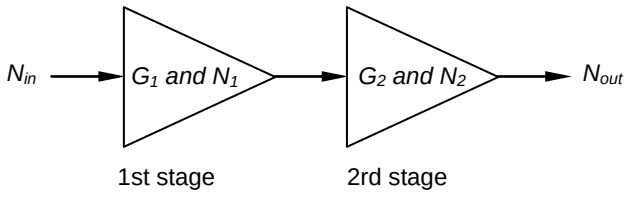

Figure 3.3. Noises in the two-stage amplifier. N_{in} is input noise, N_{out} is output noise, N_1 is device noise of the first-stage amplifier, N_2 is device noise of the second-stage amplifier, G_1 is gain of the first-stage amplifier, and G_2 is gain of the second-stage amplifier.

As shown in Figure 3.3, the output noise can be expressed by the input noise, the device noises, and the amplifier gains as follows.

$$N_{out} = N_{in}G_1G_2 + N_1G_2 + N_2 \quad (3.1)$$

where N_{in} is input noise, N_{out} is output noise, N_1 is device noise of the first-stage amplifier, N_2 is device noise of the second-stage amplifier, G_1 is gain of the first-stage amplifier, and G_2 is gain of the second-stage amplifier.

When total gain G_1G_2 is a constant K, Eq.(3.1) becomes,

$$N_{out} = N_{in}K + N_1K/G_1 + N_2 \quad (3.2)$$

Eq.(3.2) explains that the first-stage amplifier should have a higher gain G_1 [188] in order to reduce the second noise item N_1K/G_1 in Eq.(3.2).

In order to reduce the device noise, the gain G_1 is designed as 100, the gain G_2 is designed as 5, and the total gain G_1G_2 equals 500 for measuring the TcMEP signals of hand muscle. The gain G_1 is designed as 100, the gain G_2 is designed as 20, and the total gain G_1G_2 equals 2000 for measuring the TcMEP signals of hand muscle of leg and foot muscles.

3.3 IONM System and Wireless System

In order to obtain the frequency response of IONM system, a linear-swept-frequency signal of 0−1000 *Hz* and 1 *mV* was inputted into the IONM system and the IONM output waveform was recorded. Using the IONM recordings, the frequency response of the IONM system was determined by the linear continuous-time frequency-response estimation method

[189, 190]. The magnitude and the phase of the frequency-response waveforms are shown in Figure 3.4 and the frequency-response function FR_{IONM} is given in Eq.(3.3).

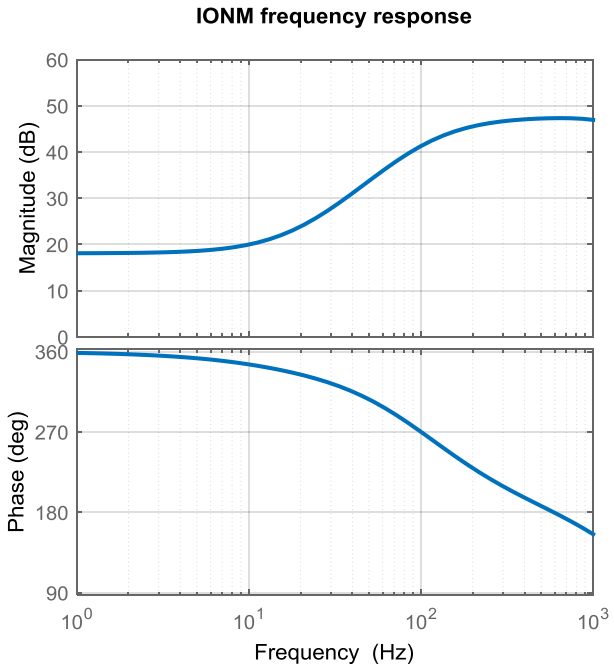

Figure 3.4. Magnitude and phase of the frequency response of the IONM system.

$$FR_{IONM} = \frac{-1.685e^{6}(j\omega)^{3}-1.959e^{10}(j\omega)^{2}-j3.782e^{11}\omega+3.076e^{14}}{(j\omega)^{4}+1.559e^{4}(j\omega)^{3}+1.01e^{8}(j\omega)^{2}+j1.166e^{11}\omega+3.834e^{13}} \quad (3.3)$$

In order to obtain the frequency response of the wireless system, the linear-swept-frequency signal was inputted into the wireless system and the output waveform of the wireless system was recorded. The magnitude and the phase of the frequency-response waveforms by the wireless system with the gain as 500 (54 *dB*) are shown in Figure 3.5 and the frequency-response function $FR_{Wireless}$ is given in Eq.(3.4).

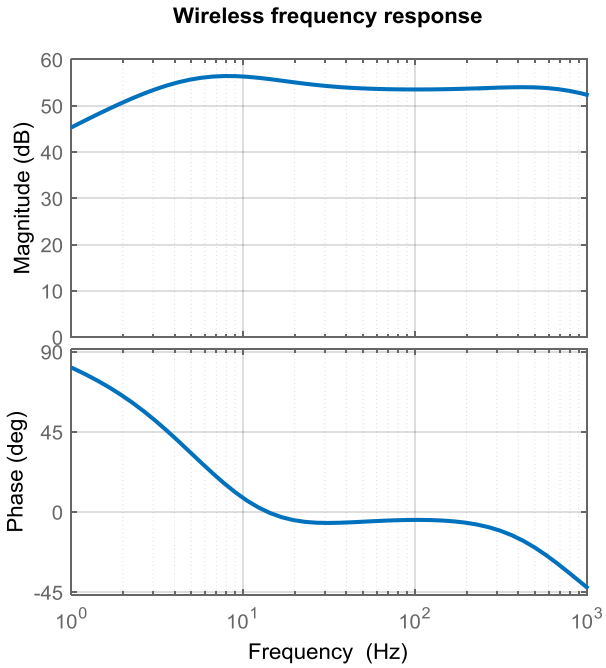

Figure 3.5. Magnitude and phase of the frequency response of the wireless system.

$$FR_{Wireless} = \frac{3.595e^{6}(j\omega)^{3}+8.896e^{9}(j\omega)^{2}+j1.029e^{12}\omega-6.1826e^{11}}{(j\omega)^{4}+8681(j\omega)^{3}+1.91e^{7}(j\omega)^{2}+j1.689e^{9}\omega+3.469e^{10}} \quad (3.4)$$

Due to the difference between the hardware and software configurations, the IONM system and the new wireless system have different frequency responses as shown in Figure 3.4 and Figure 3.5, respectively. The different frequency-response functions are also expressed in Eq.(3.3) and (3.4), respectively. However, only the IONM recording is acceptable by the doctors. Hence, the wireless recording has to be converted to the acceptable waveform using a new transfer function between the IONM system and the wireless measuring system.

3.4. Measuring, Converting, and Evaluating the Wireless Recordings

The IONM system and the wireless system for recording the TcMEP signals are shown in Figure 3.6. To compare the performances of the wireless system with the IONM system under the

same measurement conditions, the two systems were connected to the same needle electrodes (Medtronic 945DSN1299) to acquire the TcMEP signals through an analog signal splitter. The analog signal splitter outputs the same signals into the IONM system and the wireless system. H_1 is the transfer function of IONM system, H_2 is the transfer function of the wireless system, y_1 is the IONM recording, and y_2 is the wireless recording.

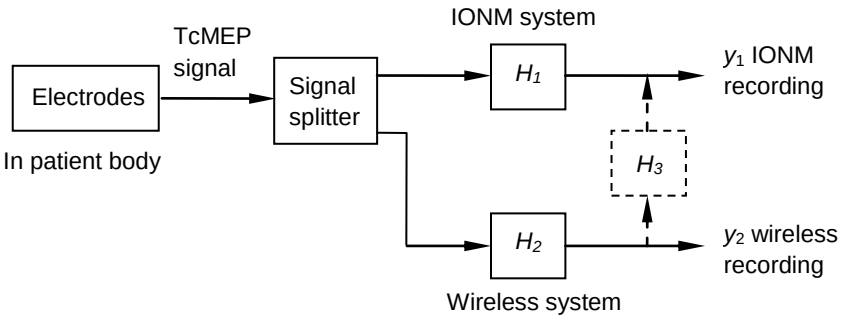

Figure 3.6. IONM system and wireless system for recording the TcMEP signals from the electrodes.

To convert the acquired wireless signal to an equivalent IONM waveform, a conversion system H_3 was constructed as shown in Figure 3.6. In order to find the transfer function of the system H_3, the wireless recording y_2 was used as the input of the system H_3 and the IONM recording y_1 was used as the output of the system H_3. The linear continuous-time transfer-function estimation method was employed and using time-domain data. The state-variable filters (SVF) and the generalized Poisson moment functions (GPMF) were used for the transfer-function estimation [189, 190]. The IONM recordings and the wireless recordings were obtained by inputting the same linear-swept-frequency signal as described in section 3.3. The wireless recording was used as the system input. The IONM recording was used as the system output. Due to the IONM and the wireless systems can be approximated to linear systems, a transfer function of the system can be found by the linear transfer-function estimation method. Using the found transfer function, the wireless recording y_2 can be converted to an equivalent IONM output y_{c1} and be acceptable by the doctors. The estimated transfer function H_3 is as follows.

$$H_3 = \frac{-197.8s^4+2.799e^4s^3+7.434e^7s^2+4.564e^7s+4.385e^8}{s^5+439.7s^4+1.602e^5s^3+2.316e^7s^2+1.153e^9s+1.602e^{10}} \quad (3.5)$$

Magnitude and phase of the transfer-function H_3 are shown in Figure 3.7.

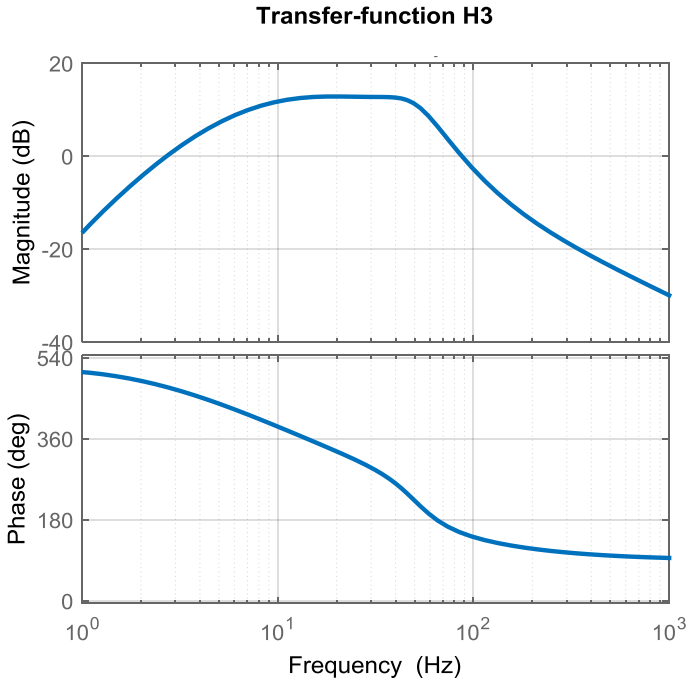

Figure 3.7. Magnitude and phase of the transfer-function H_3, where the wireless recording was used as input of the system H_3 and the IONM recording was used as the output of the system H_3.

The Wireless recording is converted by the transfer function and the converted result is evaluated as shown in Figure 3.8, where H_3 is the transfer function, y_2 is the wireless recordings, y_{c1} is the converted result, and y_1 the IONM recording which is the reference for evaluating the converted result.

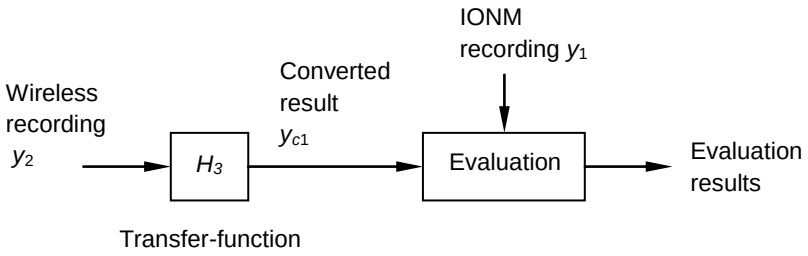

Figure 3.8. The wireless recording is converted and is evaluated.

In order to evaluate the conversion results, three statistical methods were employed to evaluate the converted results. They are the goodness of fit, Pearson's correlation, and root mean square errors, respectively.

A. Goodness of Fit

The first evaluation method is the goodness of fit [191]. The goodness of fit is a statistical method which is employed to measure the discrepancy between the converted results and the IONM recordings.

$$Fit = 1 - \frac{\sqrt{\sum_{n=1}^{N}[y_{c1}(n) - y_1(n)]^2}}{\sqrt{\sum_{n=1}^{N}(y_1(n) - mean(y_1))^2}} \tag{3.6}$$

where

$$mean(y_1) = \frac{1}{N}\sum_{n=1}^{N} y_1(n)$$

n is sample number, yc_1 is the converted result of the wireless recording, y_1 is the IONM recording, and *fit* is evaluation value.

B. Pearson's correlation

Pearson's correlation coefficient [192] is the most commonly used to measure the linear correlation between two variables. Pearson's correlation coefficient is defined as the covariance of the two variables divided by the product of their standard deviations as follows.

$$\rho = \frac{cov(y_{c1},y_1)}{\sigma_{yc1}\sigma_{y1}} \tag{3.7}$$

where ρ is Pearson correlation coefficient, *cov* is the covariance, y_{c1} is the converted result of the wireless recording, y_1 is the IONM recording, σ_{yc1} is the standard deviation of y_{c1}, and σ_{y1} is the standard deviation of y_1,.

The formula for ρ can be expressed in term of sample as follows.

$$\rho = \frac{\sum_{n=1}^{N}\{[(y_{c1}(n)-mean(y_{c1}(n))][(y_1(n)-mean(y_1(n))]\}}{\sqrt{\sum_{n=1}^{N}[(y_{c1}(n)-mean(y_{c1})]^2}\sqrt{\sum_{n=1}^{N}[(y_1(n)-mean(y_1)]^2}} \tag{3.8}$$

where

$$mean(y_x) = \frac{1}{N}\sum_{n=1}^{N} y_x(n)$$

ρ is Pearson correlation coefficient, *n* is sample number, y_{c1} is the converted result of the wireless recording, and y_1 is the IONM recording.

C. Root Mean Squared Error

The root mean square error (RMSE) is frequently used to measure the difference between two signals [193]. In the chapter, RMSE is used to evaluate the converted result of the wireless results with the following definitions.

$$RMSE = \sqrt{\frac{\sum_{n=1}^{N}[u\_y_{c1}(n) - u\_y_1(n)]^2}{N}} \quad (3.9)$$

where

$$u\_y_{c1}(n) = \frac{y_{c1}(n)}{\max(y_{c1})}$$

$$u\_y_1(n) = \frac{y_1(n)}{\max(y_1)}$$

RMSE is the root mean squared error, u_y_{c1} is unitized data of the converted result of the wireless recording, u_y_1 is unitized IONM recording, and n is sample number.

A completed flow chart of the system identification, the data conversion, and the result evaluations is shown in Figure 3.9.

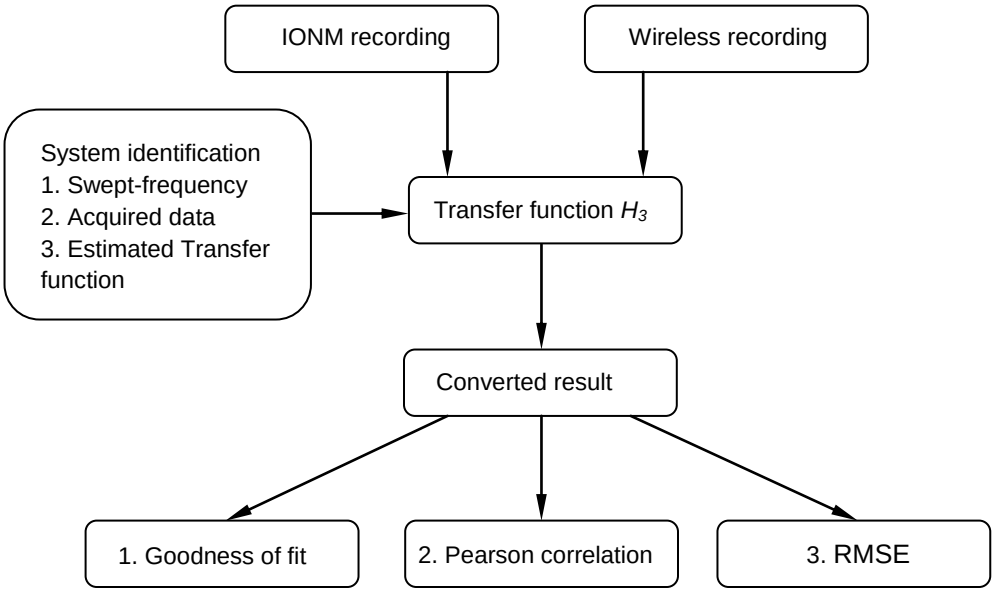

Figure 3.9. Flow chart of the system identification, the data conversion, and the result evaluations.

In the flow chart, the transfer function H_3 was obtained by the system identification method. Using the found transfer functions H_3, the wireless recordings can be converted to be fully acceptable waveforms by the doctors in the hospital. The goodness of fit, Pearson's correlation, and the root mean square errors were employed to evaluate the converted results.

3.5. Wireless Body Area Network for Intraoperative Neuromonitoring

The new wireless body area network (WBAN) was used to record the TcMEP signals from the patients who accepted the surgeries of the scoliosis correction at the Texas Scottish Rite Hospital for Children in the past two years.

The WBAN has four wireless modules which were placed at limbs of a patient. Four pairs of needle electrodes were inserted into the patient's abductor pollicis brevis muscle (at hand), tibialis anterior muscle (at leg), soleus muscle (at leg), and abductor hallucis muscle (at foot), respectively, as shown in Figure 3.10.

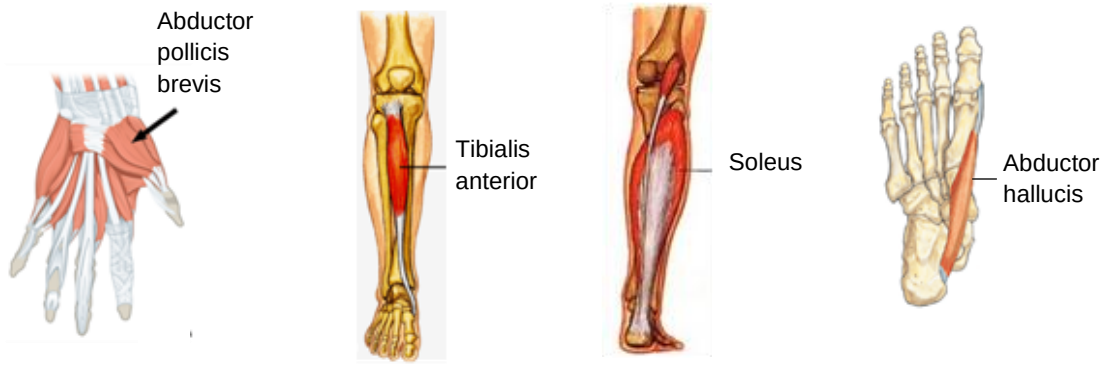

Figure 3.10. Abductor pollicis brevis muscle (at hand), tibialis anterior muscle (at leg), soleus muscle (at leg), and abductor hallucis muscle (at foot).

Four pairs of needle electrodes in the patient's abductor pollicis brevis muscle, tibialis anterior muscle, soleus muscle, and abductor hallucis muscle were connected to the input ports

of the four wireless modules in the WBAN. Acquired signals were wirelessly transmitted to the USB dongle of the host computer. 9 continuous stimulus pulses with 400V intensity were applied to the patient's scalp through the Electroencephalography (EEG) electrodes. Subsequently, the TcMEP signals were detected by the needle electrodes and were wirelessly recorded by the host computer. The wireless body area networks are shown in Figure 3.11.

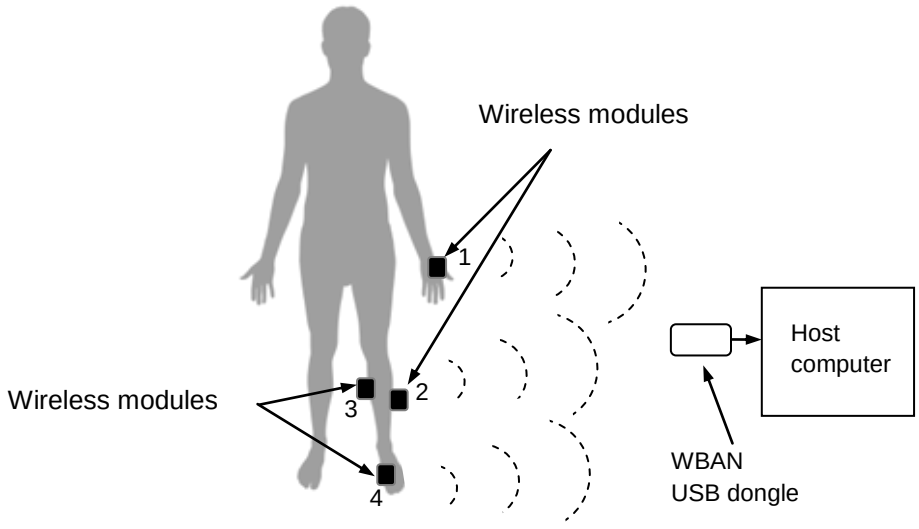

Figure 3.11. Four wireless modules in the WBAN were placed on the four measurement points which are 1. Abductor pollicis brevis muscle, 2. Tibialis anterior muscle, 3. Soleus muscle, and 4. Abductor hallucis muscle. The WBAN USB dongle received the WBAN signals.

The WBAN can isolate the critical TcMEP signals from high-level EMI in the operating room. The maximum communication range of the WBAN is over 10 *m* and battery life is over 10 hours. For further applications, more wireless measurement modules can be added into the WBAN.

In the next section, the WBAN recordings were converted to the equivalent IONM waveforms and were evaluated by the three statistical methods. The converted WBAN recording was also compared with the WBAN raw data.

3.6. Converting WBAN Recording and Evaluations

In order to evaluate the converted WBAN recording by the obtained transfer-function H_3 in Eq.(3.5), the clinical TcMEP signals from 20 patients were simultaneously recorded by the IONM system and the WBAN system. All 20 patients accepted the surgeries of the scoliosis correction at the Texas Scottish Rite Hospital for Children.

A. Converting and Evaluating WBAN Recording from the abductor pollicis brevis muscle

An IONM recording from the abductor pollicis brevis muscle is shown in Figure 3.12(a) and the recording time was 0.1 second with 6400 sample/second. Raw data of the WBAN recording from abductor pollicis brevis muscle is shown in Figure 3.12(b) and the recording time is 0.1 second with 12000 sample/second. As shown in Figure 3.12(a), after the 9 continuous stimulus pulses, the TcMEP signals occur with 4000uV amplitude in the IONM recording.

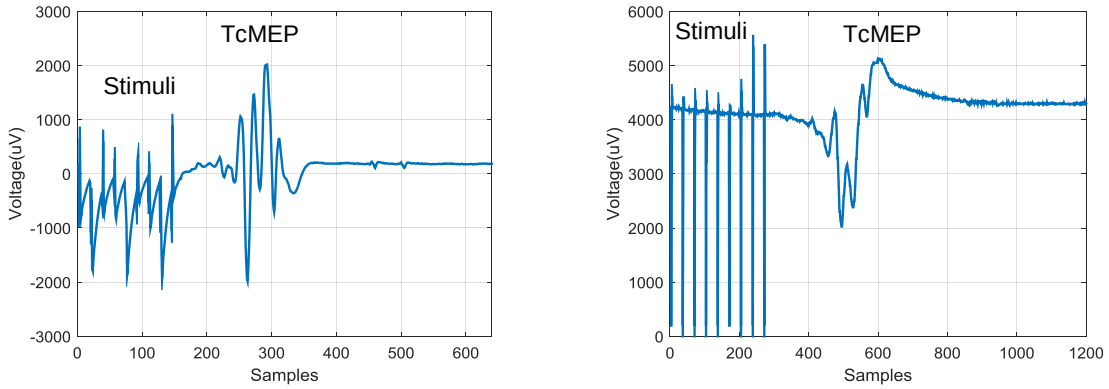

(a) (b)

Figure 3.12. Data were from the abductor pollicis brevis muscle. (a) IONM recording and (b) Raw data of WBAN recording.

The stimulus pulse trains and the dc component of the WBAN recording were removed as well as the IONM recoding was resampled to 12000 sample/second as the same as the WBAN recording. The processing results are shown in Figure 3.13(a). Then, the WBAN recording was converted by the transfer-function H_3 in Eq.(3.5). The converted result and the IONM recording are plotted in Figure 3.13(b).

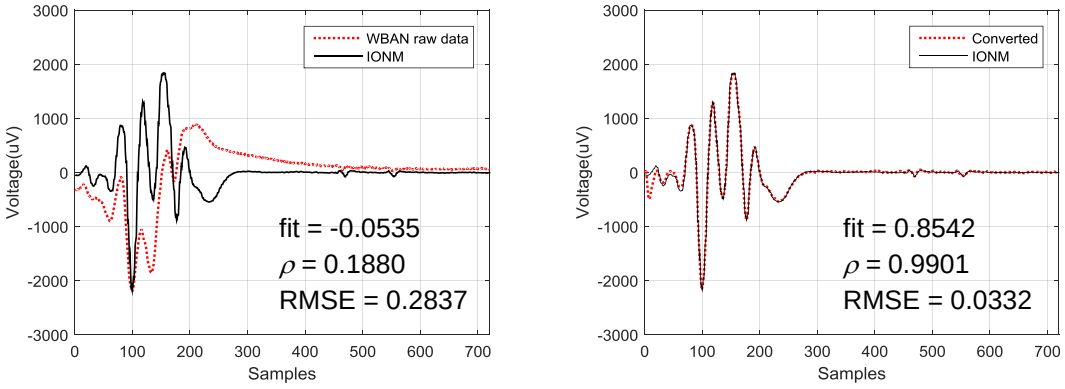

(a) (b)

Figure 3.13. Data were from the abductor pollicis brevis muscle. (a) The dc component and the 9 continuous stimulus pulses of the WBAN recording were removed and plotted with the IONM recoding. (b) The converted WBAN recording and the IONM recording.

Using the goodness of fit method, the converted WBAN recording is evaluated as 0.8542, while the raw data of WBAN recording is evaluated as -0.0535. The fit value increases about 0.91. Using the Pearson correlation method, the converted WBAN recording is evaluated as 0.9901, while the raw data of WBAN recording is evaluated as 0.1880. The correlation coefficient increases about 0.80. Using the by RMSE method, the converted WBAN recording is evaluated as 0.0332, while the raw data of WBAN recording is evaluated as 0.2837. The root mean square error decreases about 0.25. Above three evaluation results show the converted WBAN recording has a much higher similarity with the IONM recording from the abductor pollicis brevis muscle.

B. Converting and Evaluating WBAN Recording from the tibialis anterior muscle

An IONM recording from the tibialis anterior muscle is shown in Figure 3.14(a) and the recording time was 0.1 second with 6400 sample/second. Raw data of the WBAN recording from tibialis anterior muscle is shown in Figure 3.14(b) and the recording time was 0.1 second with 12000 sample/second. As shown in Figure 3.14(a), after the 9 continuous stimulus pulses, the TcMEP signals occur with 1100uV amplitude in the IONM recording.

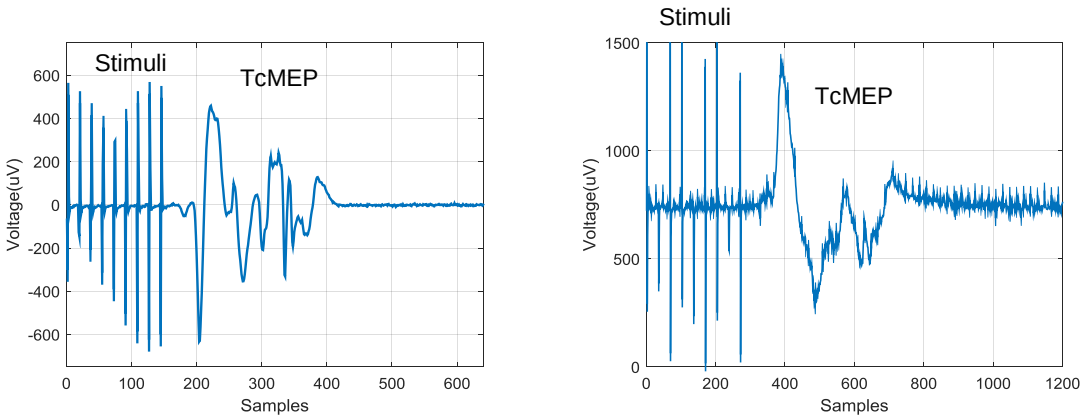

(a) (b)

Figure 3.14. Data were from the tibialis anterior muscle. (a) IONM recording and (b) Raw data of WBAN recording.

The stimulus pulse trains and the dc component of the WBAN recording were removed as well as the IONM recording was resampled to 12000 sample/second as the same as the WBAN recording. The processing results are shown in Figure 3.15(a). Then, the WBAN recording was converted by the transfer-function H_3 in Eq.(3.5). The converted result and the IONM recording are plotted in Figure 3.15(b).

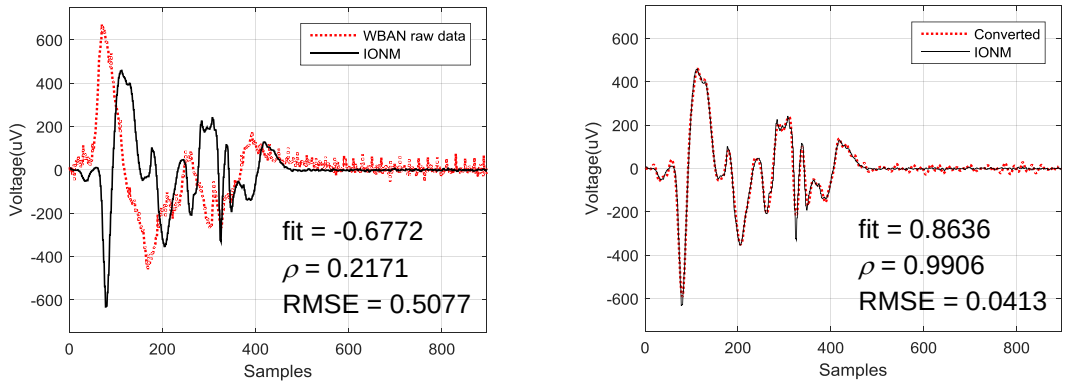

(a) (b)

Figure 3.15. Data were from the tibialis anterior muscle. (a) The dc component and the 9 continuous stimulus pulses of the WBAN recording were removed and plotted with the IONM recoding. (b) The converted WBAN recording and the IONM recording.

Using the goodness of fit method, the converted WBAN recording is evaluated as 0.8636, while the raw data of WBAN recording is evaluated as -0.6772. The fit value increases about 1.54. Using the Pearson correlation method, the converted WBAN recording is evaluated as 0.9906, while the raw data of WBAN recording is evaluated as 0.2171. The correlation coefficient increases about 0.77. Using the by RMSE method, the converted WBAN recording is evaluated as 0.0413, while the raw data of WBAN recording is evaluated as 0.5077. The root mean square error decreases about 0.47. Above three evaluation results show the converted WBAN recording has a much higher similarity with the IONM recording from the tibialis anterior muscle.

C. Converting and Evaluating WBAN Recording from the soleus muscle

An IONM recording from the soleus muscle is shown in Figure 3.16(a) and the recording time was 0.1 second with 6400 sample/second. Raw data of the WBAN recording from tibialis anterior muscle is shown in Figure 3.16(b) and the recording time was 0.1 second with 12000 sample/second. As shown in Figure 3.16(a), after the 9 continuous stimulus pulses, the TcMEP signals occur with 880uV amplitude in the IONM recording.

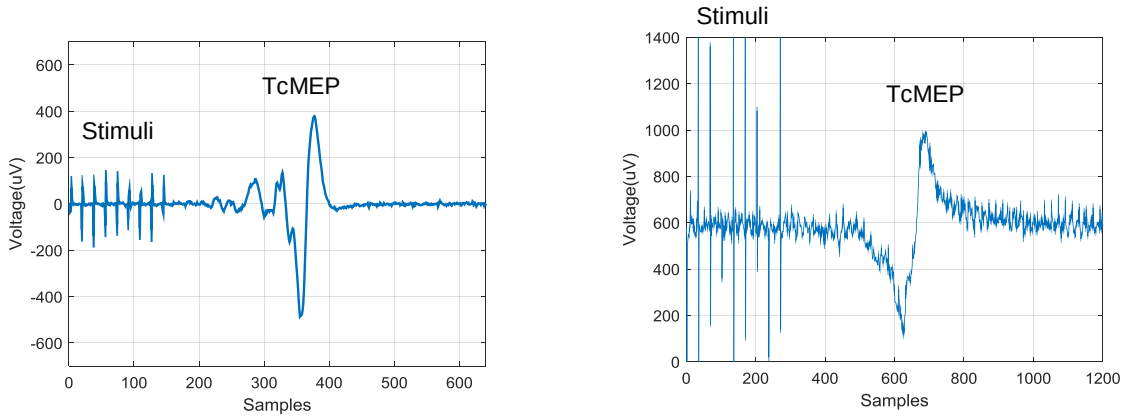

(a) (b)

Figure 3.16. Data were from the soleus muscle. (a) IONM recording and (b) Raw data of WBAN recording.

The stimulus pulse trains and the dc component of the WBAN recording were removed as well as the IONM recoding was resampled to 12000 sample/second as the same as the WBAN recording. The processing results are shown in Figure 3.17(a). Then, the WBAN recording was converted by the transfer-function H_3 in Eq.(3.5). The converted result and the IONM recording are plotted in Figure 3.17(b).

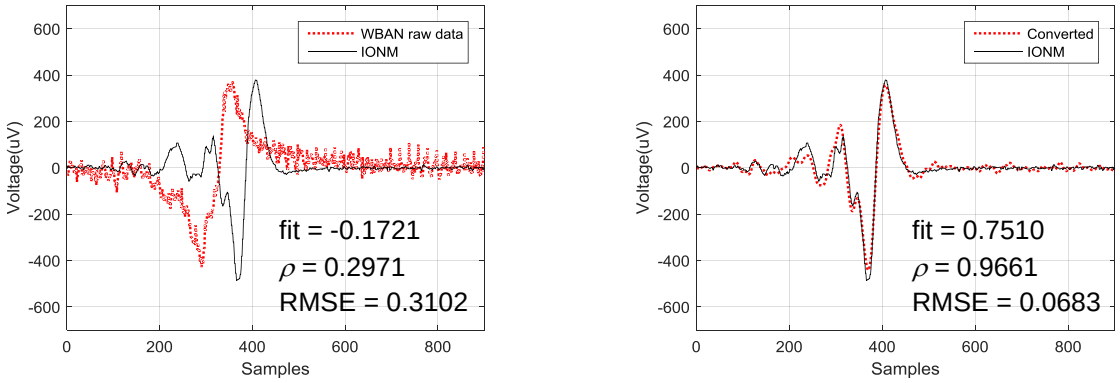

(a) (b)

Figure 3.17. Data were from the soleus muscle. (a) The dc component and the 9 continuous stimulus pulses of the WBAN recording were removed and plotted with the IONM recoding. (b) The converted WBAN recording and the IONM recording.

Using the goodness of fit method, the converted WBAN recording is evaluated as 0.7510, while the raw data of WBAN recording is evaluated as -0.1721. The fit value increases about 0.92. Using the Pearson correlation method, the converted WBAN recording is evaluated as 0.9661, while the raw data of WBAN recording is evaluated as 0.2971. The correlation coefficient increases about 0.67. Using the by RMSE method, the converted WBAN recording is evaluated as 0.0683, while the raw data of WBAN recording is evaluated as 0.3102. The root mean square error decreases about 0.24. Above three evaluation results show the converted WBAN recording has a much higher similarity with the IONM recording from the soleus muscle.

D. Converting and Evaluating WBAN Recording from the abductor hallucis muscle

An IONM recording from the abductor hallucis muscle is shown in Figure 3.18(a) and the recording time was 0.1 second with 6400 sample/second. Raw data of the WBAN recording from tibialis anterior muscle is shown in Figure 3.18(b) and the recording time was 0.1 second with 12000 sample/second. As shown in Figure 3.18(a), after the 9 continuous stimulus pulses, the TcMEP signals occur with 600uV amplitude in the IONM recording.

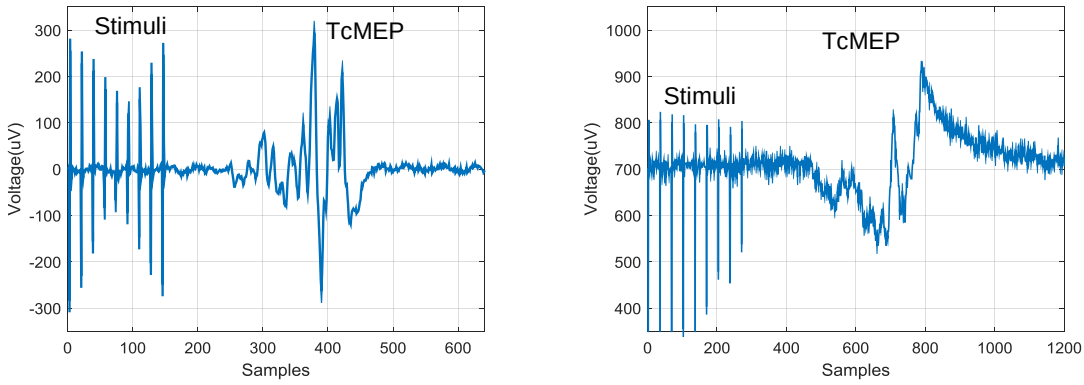

(a) (b)

Figure 3.18. Data were from the abductor hallucis muscle. (a) IONM recording and (b) Raw data of WBAN recording.

The stimulus pulse trains and the dc component of the WBAN recording were removed as well as the IONM recoding was resampled to 12000 sample/second as the same as the

WBAN recording. The processing results are shown in Figure 3.19(a). Then, the WBAN recording was converted by the transfer-function H_3 in Eq.(3.5). The converted result and the IONM recording are plotted in Figure 3.19(b).

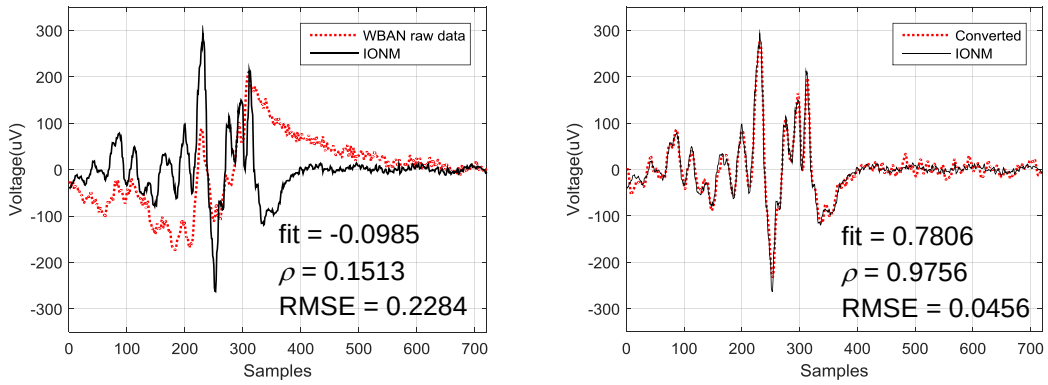

(a) (b)

Figure 3.19. Data were from the abductor hallucis muscle. (a) The dc component and the 9 continuous stimulus pulses of the WBAN recording were removed and plotted with the IONM recoding. (b) The converted WBAN recording and the IONM recording.

Using the goodness of fit method, the converted WBAN recording is evaluated as 0.7806, while the raw data of WBAN recording is evaluated as -0.0985. The fit value increases about 0.88. Using the Pearson correlation method, the converted WBAN recording is evaluated as 0.9756, while the raw data of WBAN recording is evaluated as 0.1513. The correlation coefficient increases about 0.82. Using the by RMSE method, the converted WBAN recording is evaluated as 0.0456, while the raw data of WBAN recording is evaluated as 0.2284. The root mean square error decreases about 0.18. Above three evaluation results show the converted WBAN recording has a much higher similarity with the IONM recording the abductor hallucis muscle.

E. Converting and Evaluating the 19 WBAN Recordings

Figure 3.20(a) and (b) show a complete TcMEP set which consists of the 19 IONM clinical recordings and the 19 WBAN clinical recordings from the abductor pollicis brevis muscle

of one patient in an idiopathic scoliosis correction surgery during 2.5-hour period at the Texas Scottish Rite Hospital for Children. The 19 WBAN clinical recordings were converted to the equivalent IONM waveforms as shown in Figure 3.20(c), where the solid lines express the IONM recordings and the dotted lines express the converted WBAN recordings.

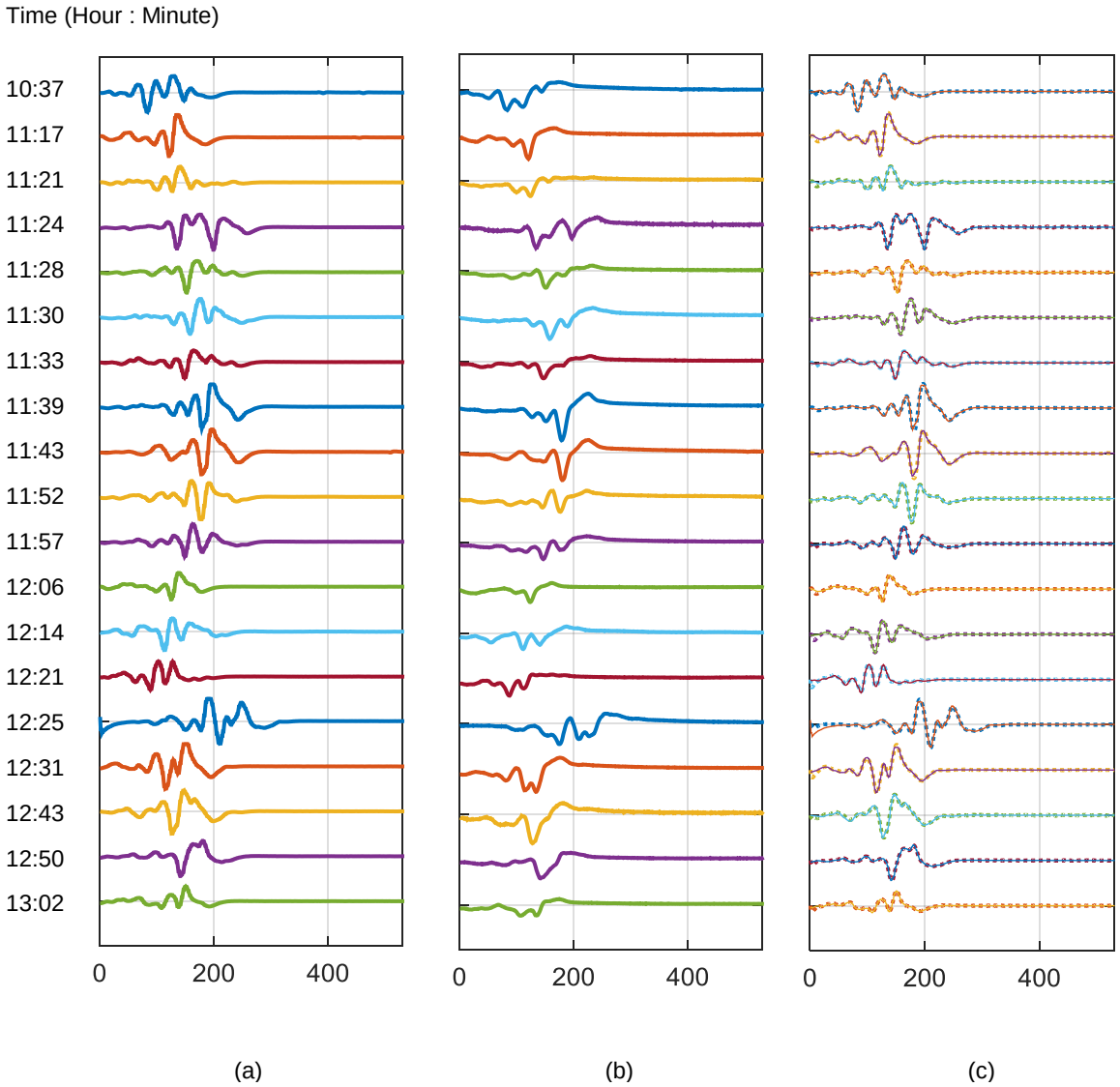

Figure 3.20. Data were from the abductor pollicis brevis muscle during 2.5-hour surgery period. (a) The IONM recordings. (b) The WBAN recordings. (c) The converted WBAN recordings (dotted line) and the IONM recordings (solid line).

In order to demonstrate the data conversion details, the first five IONM recordings and original WBAN recordings from the abductor pollicis brevis muscle are shown in Figure 3.21(a) while the converted WBAN recordings and the IONM recordings are shown in Figure 3.21(b).

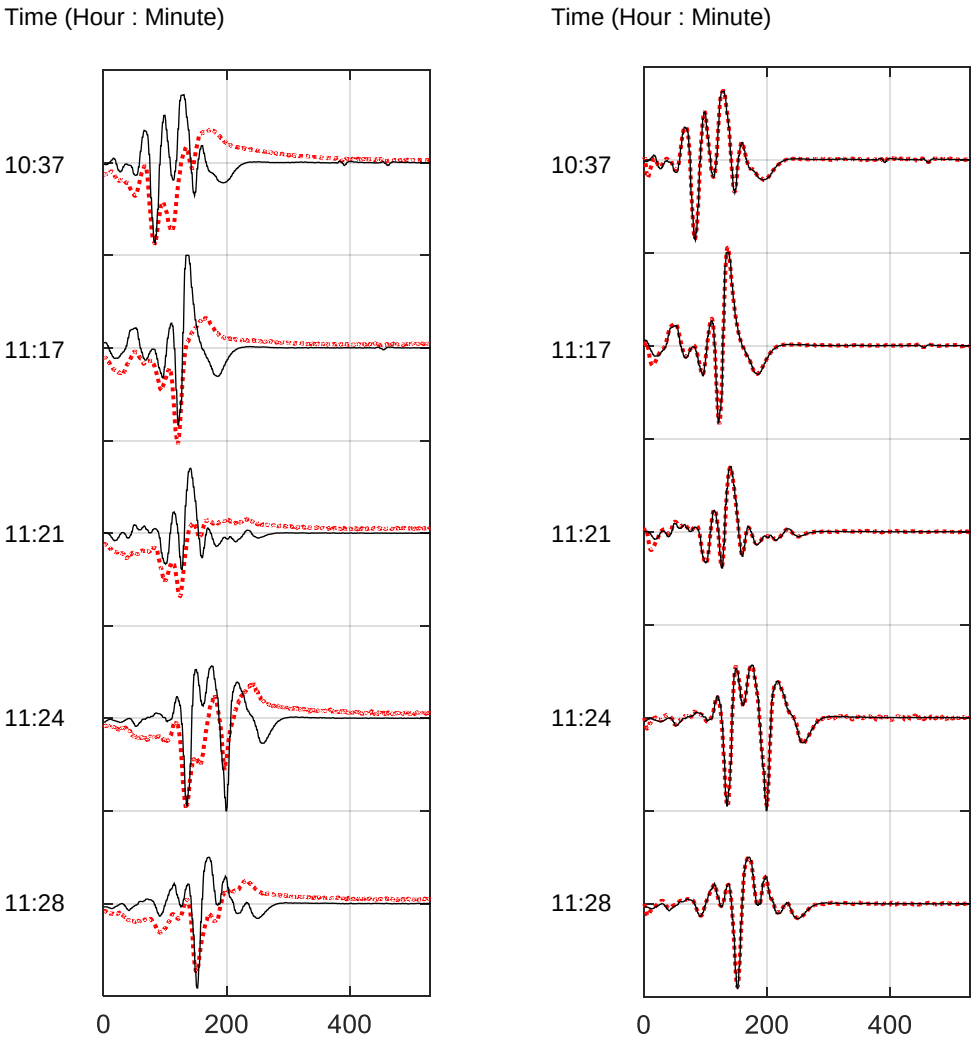

Figure 3.21. Data were from the abductor pollicis brevis muscle. (a) The first five WBAN recordings (dotted line) and IONM recordings (solid line). (b) The first five converted WBAN recordings (dotted line) and the IONM recordings (solid line).

Figure 3.22(a) and (b) show a complete TcMEP set which consists of the 19 IONM clinical recordings and the 19 WBAN clinical recordings from the abductor hallucis muscle of one patient in an idiopathic scoliosis correction surgery during 2.5-hour period at the Scottish Rite Hospital for Children. The 19 WBAN clinical recordings were converted to the equivalent IONM waveforms as shown in Figure 3.22(c), where the solid lines express the IONM recordings and the dotted lines express the converted WBAN recordings.

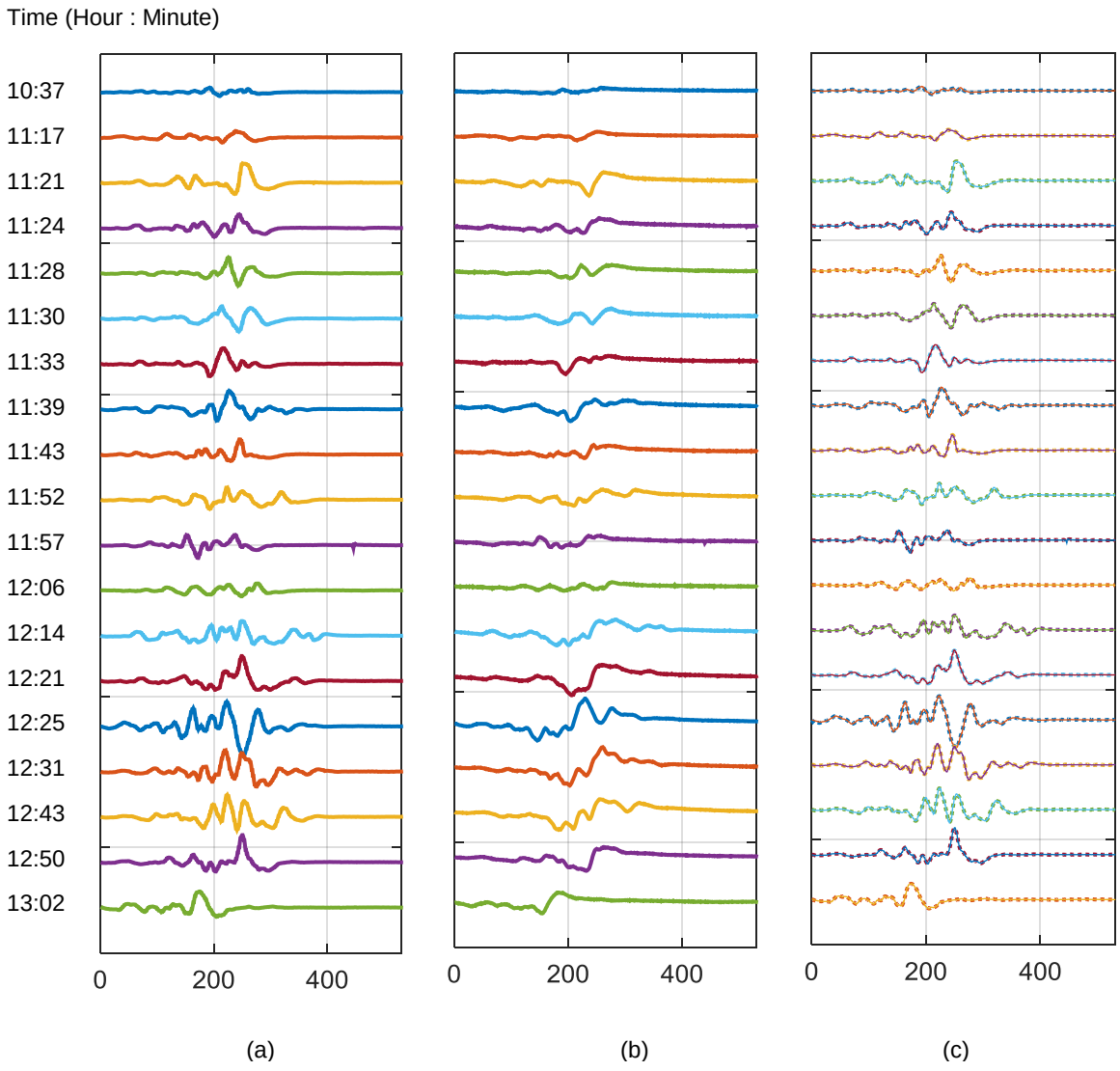

Figure 3.22. Data were from the abductor hallucis muscle during 2.5-hour surgery period. (a) The IONM recordings. (b) The WBAN recordings. (c) The converted WBAN recordings (dotted line) and the IONM recordings (solid line).

In order to demonstrate the data conversion details, the first five IONM recordings and original WBAN recordings from the abductor hallucis muscle are shown in Figure 3.23(a) and the converted WBAN recordings and the IONM recordings are shown in Figure 3.23(b).

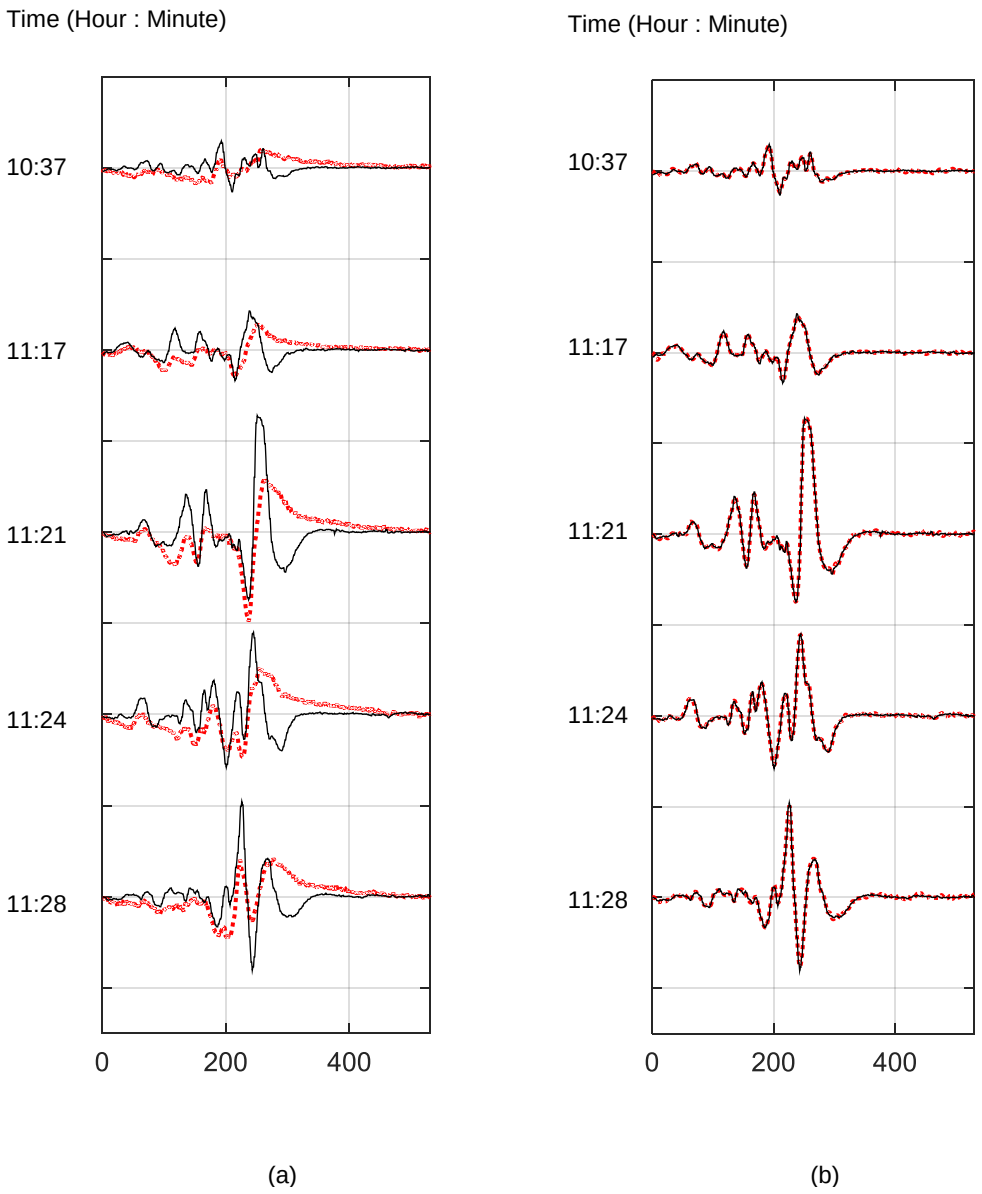

Figure 3.23. Data were from the abductor hallucis muscle. (a) The first five WBAN recordings (dotted line) and IONM recordings (solid line). (b) The first five converted WBAN recordings (dotted line) and the IONM recordings (solid line).

The converted results of the 19 WBAN recordings as shown in Figure 3.20.(c) and Figure 3.22.(c) were evaluated by the goodness of fit, Pearson correlation, and RMSE methods, respectively. The evaluation results are listed in Table 3.1. The maximum value, minimum value, average value, and standard deviation are also calculated.

Table 3.1. The evaluation results, maximum value, minimum value, average value, and standard deviation.

Converted recording	Record Time (Hour : Minute)	Abductor pollicis brevis (at hand)			Abductor hallucis (at foot)		
		Fit	ρ	RMSE	Fit	ρ	RMSE
Sample 1	10:37	0.8542	0.9901	0.0332	0.7806	0.9756	0.0456
Sample 2	11:17	0.8385	0.9881	0.0283	0.8431	0.9876	0.0366
Sample 3	11:21	0.7958	0.9808	0.0332	0.9011	0.9951	0.0204
Sample 4	11:24	0.8406	0.9894	0.0520	0.8750	0.9922	0.0242
Sample 5	11:28	0.8681	0.9921	0.0332	0.8672	0.9911	0.0228
Sample 6	11:30	0.8671	0.9691	0.0469	0.9066	0.9957	0.0234
Sample 7	11:33	0.8469	0.9893	0.0332	0.9074	0.9957	0.0173
Sample 8	11:39	0.6274	0.9750	0.0762	0.9145	0.9964	0.0164
Sample 9	11:43	0.7197	0.9818	0.0600	0.8672	0.9916	0.0206
Sample 10	11:52	0.8752	0.9925	0.0283	0.8968	0.9947	0.0238
Sample 11	11:57	0.8553	0.9900	0.0245	0.8748	0.9924	0.0308
Sample 12	12:06	0.8116	0.9847	0.0346	0.8780	0.9926	0.0286
Sample 13	12:14	0.7858	0.9788	0.0520	0.9050	0.9957	0.0242
Sample 14	12:21	0.7209	0.9649	0.0557	0.9256	0.9973	0.0134
Sample 15	12:25	0.7322	0.9650	0.0574	0.9092	0.9959	0.0253
Sample 16	12:31	0.7762	0.9829	0.0480	0.8905	0.9940	0.0254
Sample 17	12:43	0.7352	0.9812	0.0583	0.9103	0.9961	0.0198
Sample 18	12:50	0.8640	0.9927	0.0316	0.9131	0.9962	0.0132
Sample 19	13:02	0.7767	0.9777	0.0361	0.9233	0.9971	0.0168
Maximum value		0.8752	0.9927	0.0762	0.9256	0.9973	0.0456
Minimum value		0.6274	0.9649	0.0245	0.7806	0.9756	0.0132
Average value		0.7995	0.9824	0.0433	0.8889	0.9933	0.0236
Standard deviation		0.0679	0.0089	0.0141	0.0342	0.0050	0.0079

Note: Fit is Goodness of fit; ρ is Pearson correlation; and RMSE is root mean square error.

Employing the goodness of fit method, the average evaluation value of the 19 converted WBAN recordings from abductor pollicis brevis muscle is 0.7995, while the average evaluation value from abductor hallucis muscle is 0.8889. Employing the Pearson correlation method, the average evaluation value of the 19 converted WBAN recordings from abductor pollicis brevis muscle is 0.9824, while the average evaluation value from abductor hallucis muscle is 0.9933. Employing the RMSE method, the average evaluation value of the 19 converted WBAN recordings from abductor pollicis brevis muscle is 0.0433, while the average evaluation value from abductor hallucis muscle is 0.0236.

As listed in Table 3.1, the evaluation results show that the converted WBAN recordings can be equivalent to the IONM recordings. Comparing the three evaluation methods, when the recordings were from the abductor pollicis brevis muscle, the Pearson correlation method can give the minimum standard deviation (0.0089) to compare with the goodness of fit (0.0679) and RMSE methods (0.0141). When the recordings were from the abductor hallucis muscle, the Pearson correlation method can give the minimum standard deviation (0.0050) to compare with the goodness of fit (0.0342) and RMSE methods (0.0079). The comparisons show that the Pearson correlation method has the stabilizing performance for evaluating the converted recordings.

In next section, the converted results of WBAN recordings are compared with the raw data, which can show that the discrepancies between the converted WBAN recordings and the IONM recordings are greatly decreased after used the transfer function conversion.

F. Comparing the Converted Data with the Raw Data by the goodness of fit method

The 19 raw data of WBAN recordings are evaluated by the three statistical methods and are compared with the 19 converted WBAN recordings. Using the goodness of fit method, the evaluation value of the converted WBAN data from the abductor pollicis brevis muscle and the evaluation value of the raw data of WBAN recording are plotted in Figure 3.24. The evaluation value of the raw data is the red bar and the evaluation value of the converted data is the blue bar in the figure.

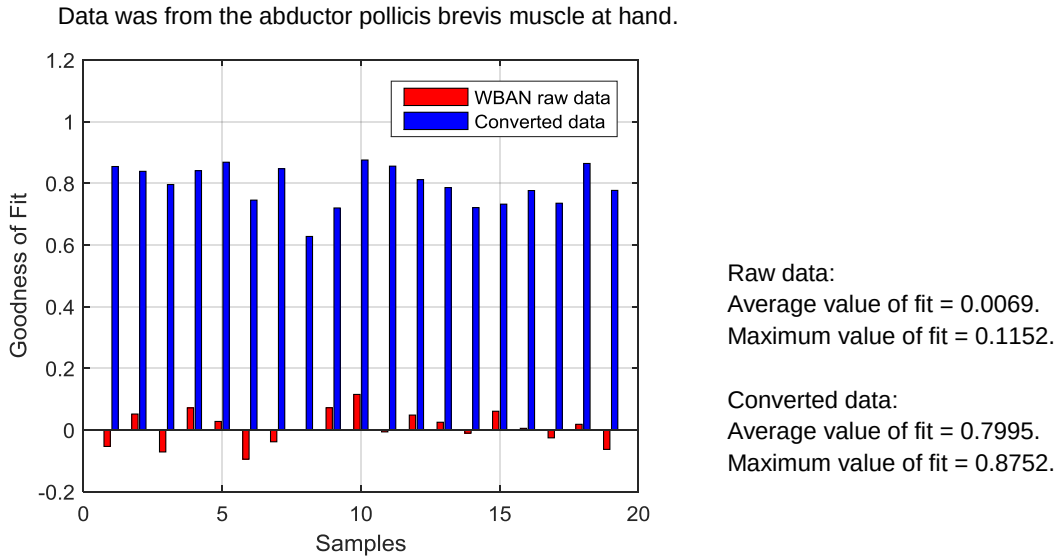

Figure 3.24. Data were from the abductor pollicis brevis muscle. The goodness of fit method was used to evaluate the converted data and the raw data of WBAN recording. The evaluation value of the converted data is the blue bar and the evaluation value of the raw data of WBAN recording is the red bar.

In Figure 3.24, using the goodness of fit method, the average evaluation value of the 19 raw data of the WBAN recording from the abductor pollicis brevis muscle is 0.0069 and the average evaluation value of the converted data increases to 0.7995. The maximum evaluation value of the 19 raw data of the WBAN recording is 0.1152 and the maximum evaluation value of the converted data increases to 0.8752.

Using the goodness of fit method, the evaluation values of the converted data from the abductor hallucis muscle and the evaluation values of the raw data of WBAN recording are plotted in Figure 3.25. The evaluation value of the converted data is the blue bar and the evaluation value of the raw data of WBAN recording is the red bar in the figures.

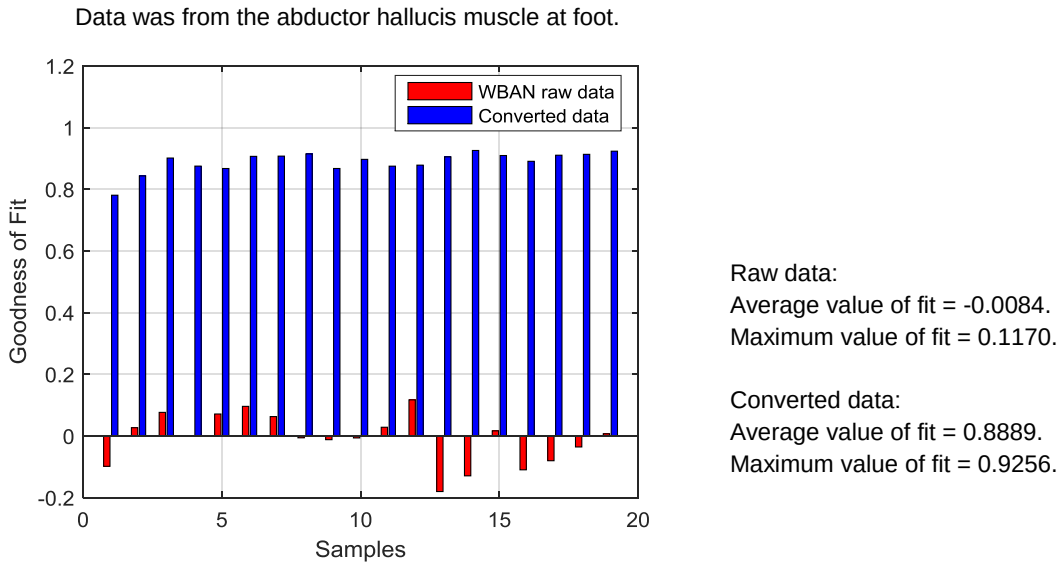

Figure 3.25. Data were from the abductor hallucis muscle. The goodness of fit method was used to evaluate the converted results and the raw data of WBAN recording. The evaluation value of the converted data is the blue bar and the evaluation value of the raw data of WBAN recording is the red bar.

In Figure 3.25, using the goodness of fit method, the average evaluation value of the 19 raw data of the WBAN recording from the abductor hallucis muscle is -0.0084 and the average evaluation value of the converted data increases to 0.8889. The maximum evaluation value of the 19 raw data of the WBAN recording is 0.1170 and the maximum evaluation value of the converted data increases to 0.9256.

G. Comparing the Converted Data with the Raw Data by the Pearson correlation method

Using the Pearson correlation method, the evaluation values of the converted data from the abductor pollicis brevis muscle and the evaluation values of the raw data of WBAN recording are plotted in Figure 3.26. The evaluation value of the converted data is the blue bar and the evaluation value of the raw data of WBAN recording is the red bar in the figure.

Data was from the abductor pollicis brevis muscle at hand.

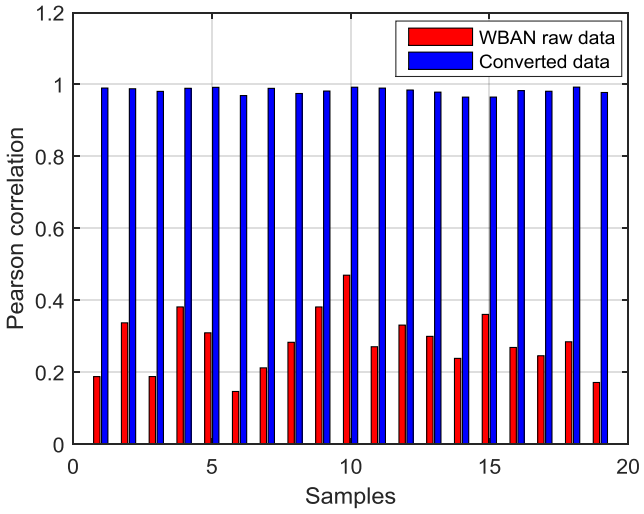

Raw data:
Average value of ρ = 0.2828.
Maximum value of ρ = 0.4700.

Converted data:
Average value of ρ = 0.9824.
Maximum value of ρ = 0.9927.

Figure 3.26. Data were from the abductor pollicis brevis muscle. The Pearson correlation method was used to evaluate the converted results and the raw data of WBAN recording. The evaluation value of the converted data is the blue bar and the evaluation value of the raw data of WBAN recording is the red bar.

In Figure 3.26, using the Pearson correlation method, the average correlation coefficient of the 19 raw data of the WBAN recording from the abductor pollicis brevis muscle is 0.2828 and the average correlation coefficient of the converted data increases to 0.9824. The maximum Pearson correlation coefficient of the 19 raw data of the WBAN recording is 0.4700 and the maximum Pearson correlation coefficient of the converted data increases to 0.9927.

Using the Pearson correlation method, the evaluation values of the converted data from the abductor hallucis muscle and the evaluation values of the raw data of WBAN recording are plotted in Figure 3.27. The evaluation value of the converted data is the blue bar and the evaluation value of the raw data of WBAN recording is the red bar in the figure.

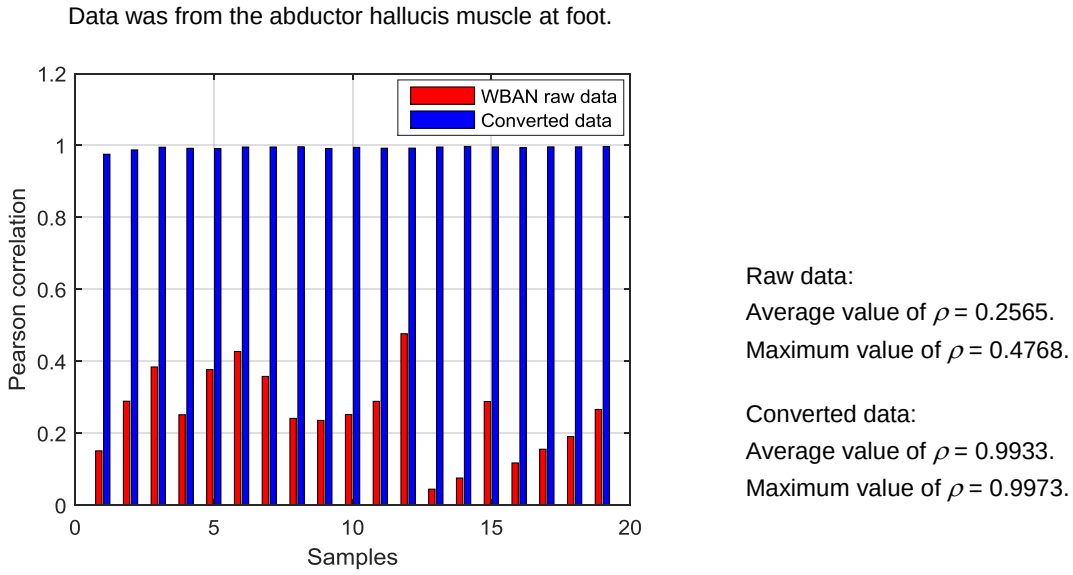

Figure 3.27. Data were from the abductor hallucis muscle. The Pearson correlation method was used to evaluate the converted results and the raw data of WBAN recording. The evaluation value of the converted data is the blue bar and the evaluation value of the raw data of WBAN recording is the red bar.

In Figure 3.27, using the Pearson correlation method, the average correlation coefficient of the 19 raw data of WBAN recording from the abductor hallucis muscle is 0.2565 and the average correlation coefficient of the converted data increases to 0.9933. The maximum Pearson correlation coefficient of the 19 raw data of WBAN recording is 0.4768 and the maximum Pearson correlation coefficient of the converted data increases to 0.9973.

H. Comparing the Converted Data with the Raw Data by the RMSE method

Using the RMSE method, the evaluation values of the converted data from the abductor pollicis brevis muscle and the evaluation values of the raw data of WBAN recording are plotted in Figure 3.28. The evaluation value of the converted data is the blue bar and the evaluation value of the raw data of WBAN recording is the red bar in the figure.

Data was from the abductor pollicis brevis muscle at hand.

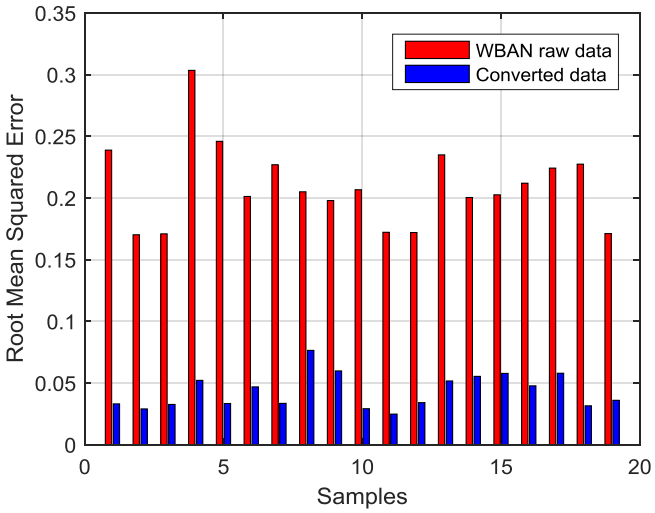

Raw data:
Average value of RMSE = 0.2096.
Maximum value of RMSE = 0.3034.

Converted data:
Average value of RMSE = 0.0433.
Maximum value of RMSE = 0.0764.

Figure 3.28. Data were from the abductor pollicis brevis muscle. The RMSE method was used to evaluate the converted data and the raw data of WBAN recording. The evaluation value of the converted data is the blue bar and the evaluation value of the raw data of WBAN recording is the red bar.

In Figure 3.28, using RMSE method, the average RMSE of the 19 raw data of WBAN recording from the abductor pollicis brevis muscle is 0.2096 and the average RMSE of the converted data reduces to 0.0433. The maximum RMSE of the 19 raw data of WBAN recording is 0.3034 and the average RMSE of the converted data reduces to 0.0764.

Using the RMSE method, the evaluation values of the converted data from the abductor hallucis muscle and the evaluation values of the raw data of WBAN recording are plotted in Figure 3.29. The evaluation value of the converted data is the blue bar and the evaluation value of the raw data of WBAN recording is the red bar in the figure.

Data was from the abductor hallucis muscle at foot.

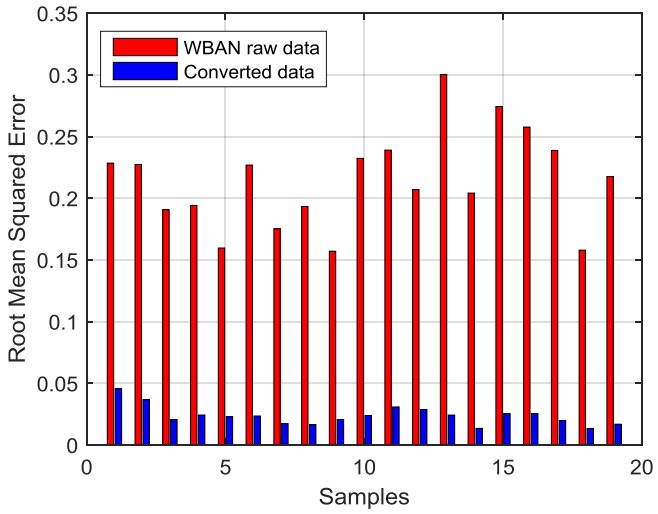

Raw data:
Average value of RMSE = 0.2148.
Maximum value of RMSE = 0.3002.

Converted data:
Average value of RMSE = 0.0456.
Maximum value of RMSE = 0.0236.

Figure 3.29. Data were from the abductor hallucis muscle. The RMSE method was used to evaluate the converted results and the raw data of WBAN recording. The evaluation value of the converted data is the blue bar and the evaluation value of the raw data of WBAN recording is the red bar.

In Figure 3.29, using RMSE method, the average RMSE of the 19 raw data of WBAN recording from the abductor hallucis muscle is 0.2148 and the average RMSE of the converted data reduces to 0.0456. The maximum RMSE of the 19 raw data of WBAN recording is 0.3002 and the average RMSE of the converted data reduces to 0.0236.

After used the transfer function to convert the raw WBAN recordings, the discrepancies between the converted WBAN recordings and the IONM recordings are greatly decreased, which has been verified by a lot of samples with the three evaluation methods, as shown from Figure 3.24 to Figure 3.29.

3.7 Conclusions

Using four wireless modules, a new wireless body area network (WBAN) was developed for Intraoperative Neuromonitoring (IONM) and has the advantages of small size, 30 *g* weight, low cost, high sample rate, maximum communication range over 10 *m*, battery life over 10 hours, and isolating the weak TcMEP signals from the high-level electromagnetic interference in the operating room. Due to the differences in the IONM system and the WBAN system, the WBAN recordings are different from the IONM recordings. In order to convert the WBAN recordings to the acceptable signals by the doctors, the transfer function was identified and was used to convert the WBAN recordings into the equivalent IONM waveforms. The converted results were evaluated by three statistical methods, respectively. The comparisons of evaluation values show that the Pearson correlation method has a smaller standard deviation than the goodness of fit and RMSE methods. Therefore, Pearson correlation method has stabilizing performance and more suitable for evaluating the converted WBAN recording. The evaluation results demonstrate that the new WBAN may be used for the Intraoperative Neuromonitoring.

APPENDIX

Publications

[1] W. Y. Shi and J. -C. Chiao, “Neural network based real-time heart sound monitor using a wireless wearable wrist sensor,” *Springer, Analog Integrated Circuits and Signal Processing*, Volume 94, Issue 3, pp. 383 - 393, 2018.

[2] W. Y. Shi and J. -C. Chiao, “Contactless hand tremor detector based on an inductive sensor,” *Springer, Analog Integrated Circuits and Signal Processing*, Volume 94, Issue 3, pp. 395 - 403, 2018.

[3] W. Y. Shi and J.-C. Chiao, “A Double-Resonant Sensor for Identifying Biological Tissues,” *IEEE Sensors*, New Delhi, India. Oct. 28 - 31, 2018.

[4] W. Y. Shi, P. Rampy, S. Sparagana, D. Sucato and J.-C. Chiao, “Validation of a Wireless Intraoperative Neuro-monitoring System,” *Biomedical Engineering Society Annual Meeting*, Atlanta, Georgia, Oct. 17 - 20, 2018.

[5] W. Y. Shi and J.-C. Chiao, “Report of a Split-ring Sensor Array for Solution Identification,” *Biomedical Engineering Society Annual Meeting*, Atlanta, Georgia, Oct. 17-20, 2018.

[6] W. Y. Shi and J. -C. Chiao, “Contactless hand tremor detector based on an inductive sensor,” *IEEE Dallas Circuits and Systems Conference*, Arlington, TX, pp. 1 - 4, 2016.

[7] W. Y. Shi and J. -C. Chiao, “Neural network based real-time heart sound monitor using a wireless wearable wrist sensor,” *IEEE Dallas Circuits and Systems Conference*, Arlington, TX, pp. 1 - 4, 2016.

[8] W. Y. Shi, Jeffrey Mays, and J. -C. Chiao, “Wireless stethoscope for recording heart and lung sound,” *IEEE Topical Conference on Biomedical Wireless Technologies*, Networks, and Sensing Systems, pp.1 - 4, 2016.

[9] W. Y. Shi and Chiao, J. -C., “A contactless detector for tremors,” *IEEE international microwave workshop series on RF and wireless technologies for biomedical and healthcare applications*, pp. 195 - 196, 2015.

[10] W. Y.Shi, J. Mays, and J. -C. Chiao, “A wireless stethoscope,” *IEEE International Microwave Workshop Series on RF and Wireless Technologies for Biomedical and Healthcare Applications,* pp. 197 - 198, 2015.

[11] W. Y. Shi, C. Nguyen, J.-C. Chiao, “Wireless Recording of Arterial Pulses,” *BMES Annual Meeting*, San Antonio, TX. October 22 - 25, 2014.

REFERENCES

[1] A. Nag, S. C. Mukhopadhyay, and J. Kosel, “Wearable Flexible Sensors: A Review,” *IEEE Sensors Journal*, vol. 17, no. 13, pp.3949 - 3960, 2017.

[2] S.C. Mukhopadhyay, “Wearable sensors for human activity monitoring: A review,” *IEEE sensors journal*, vol. 15, no. 3, pp.1321-1330, 2015.

[3] S. Patel, H. Park, P. Bonato, et al., “A review of wearable sensors and systems with application in rehabilitation,” *Journal of neuroengineering and rehabilitation*, vol. 9, no.1, pp. 1 - 17, 2012.

[4] J. Yao, and S. Warren, “Applying the ISO/IEEE 11073 standards to wearable home health monitoring systems,” *Journal of clinical monitoring and computing*, vol. 19, no. 6, pp. 427 - 436, 2005.

[5] J. M. Tjensvold, “Comparison of the IEEE 802.11, 802.15. 1, 802.15. 4 and 802.15. 6 wireless standards,” *IEEE*, September, vol. 18, pp. 1 - 7, 2007.

[6] K. S. Kwak, S. Ullah and N. Ullah, “An overview of IEEE 802.15. 6 standard,” *Applied Sciences in Biomedical and Communication Technologies (ISABEL), 3rd International Symposium*. 2010.

[7] C. C. Poon, B. P. Lo, M. R. Yuce, et al., “Body sensor networks: In the era of big data and beyond. Biomedical Engineering,” *IEEE reviews in biomedical engineering*, vol. 8, pp. 4 - 16, 2015.

[8] T. G. Pickering, D. Shimbo, and D. Haas, “Ambulatory blood-pressure monitoring,” *N. Engl. J. Med*. Vol. 354, no. 22, pp. 2368 - 2374. 2006.

[9] X. Teng, Y. Zhang, C. C. Poon, et al., “Wearable medical systems for p-health,” *IEEE reviews in Biomedical engineering*, vol. 1, pp. 62 - 74. 2008.

[10] M. Chan, D. Estève, J. Fourniols, et al., “Smart wearable systems: Current status and future challenges,” *Artif. Intell. Med*., vol. 56, no. 3, pp. 137 - 156. 2012.

[11] CC3200 SimpleLink™ Wi-Fi® and Internet-of-Things Solution, a Single-Chip Wireless MCU, Texas Instruments Inc., JUNE 2014. datasheet SWAS032F.

[12] CC2640 SimpleLink™ Bluetooth® Smart Wireless MCU, Texas Instruments Inc., OCTOBER 2015, datasheet SWRS176B.

[13] CC2630 SimpleLink™ 6LoWPAN, ZigBee® Wireless MCU, Texas Instruments Inc., OCTOBER 2015, datasheet SWRS177B.

[14] CC2500, Low-Cost Low-Power 2.4 GHz RF Transceiver (Rev. B), Texas Instruments, Inc., May 2009, datasheet SWRS040C.

[15] CC1101 low-power sub-1 GHz RF transceiver, Texas Instruments, Inc., 2017, datasheet SWRS061I.

[16] N. A. Bhatti, M. H. Alizai, A. A. Syed, et al., “Energy harvesting and wireless transfer in sensor network applications: Concepts and experiences,” *ACM Transactions on Sensor Networks (TOSN)*, vol. 12, no. 3, pp. 1 - 40, 2016.

[17] S. Ulukus, A. Yener, E. Erkip, O. Simeone, M. Zorzi, P. Grover, and K. Huang, "Energy Harvesting Wireless Communications: A Review of Recent Advances," *IEEE Journal on Selected Areas in Communications*, vol. 33, no. 3, pp. 360 - 381, 2015.

[18] F. Akhtar and M.H. Rehmani,"Energy Harvesting for Self-Sustainable Wireless Body Area Networks," *IEEE IT Professional*, vol. 19, no. 2, pp. 32 - 40, 2017.

[19] F. Samad, M. F. Karim, V. Paulose, et al., “A curved electromagnetic energy harvesting system for wearable electronics,” *IEEE Sensors Journal* vol. 16, no. 7, pp. 1969 - 1974, 2016.

[20] G. De Pasquale, S. Kim, and D. De Pasquale, “GoldFinger: Wireless human-machine interface with dedicated software and biomechanical energy harvesting system,” *IEEE/ASME Transactions on Mechatronics*, vol. 21, no. 1, pp. 565 - 575, 2016.

[21] L. Xie and M. Cai, “An in-shoe harvester with motion magnification for scavenging energy from human foot strike. Mechatronics,” *IEEE/ASME Transactions on Mechatronics*, vol. 20, no. 6, pp. 3264 - 3268, 2015.

[22] N. Cui, J. Liu, L. Gu, et al., “Wearable triboelectric generator for powering the portable electronic devices,” *ACS Applied Materials & Interfaces*, vol. 7, no. 33, pp. 18225 - 18230, 2015.

[23] V. Misra, A. Bozkurt, B. Calhoun, et al., “Flexible technologies for self-powered wearable health and environmental sensing,” *Proceedings of the IEEE*, vol. 103, no. 4, pp. 665 - 681, 2015.

[24] V. Leonov, “Thermoelectric energy harvesting of human body heat for wearable sensors,” *IEEE Sensors Journal*, vol. 13, no.6, pp. 2284 - 2291, 2013.

[25] X. Fan, J. Chen, J. Yang, et al., “Ultrathin, rollable, paper-based triboelectric nanogenerator for acoustic energy harvesting and self-powered sound recording,” *ACS Nano*, vol. 9, no. 4, pp. 4236 - 4243, 2015.

[26] J. Bito, J. G. Hester, and M. M. Tentzeris, “Ambient RF energy harvesting from a two-way talk radio for flexible wearable wireless sensor devices utilizing inkjet printing technologies,” *IEEE Transactions on Microwave Theory and Techniques,* vol. 63, no. 12, pp. 4533 - 4543. 2015.

[27] V. Talla, S. Pellerano, H. Xu, et al., “Wi-Fi RF energy harvesting for battery-free wearable radio platforms,” *IEEE International Conference on RFID (RFID)*, pp. 47 - 54, 2015.

[28] J. Gummeson, B. Priyantha, and J. Liu, “An energy harvesting wearable ring platform for gestureinput on surfaces,” *Proceedings of the 12th annual international conference on Mobile systems, applications, and services. ACM*, pp. 162 - 175, 2014,

[29] H. J. Visser, A. C. F. Reniers, and J. A. C. Theeuwes, “Ambient RF energy scavenging: GSM and WLAN power density measurements,” *Microwave Conference, EuMC 2008*. *38th European*, pp. 721 - 724, 2008.

[30] G. Monti, F. Congedo, D. De Donno, et al, “Monopole-based rectenna for microwave energy harvesting of UHF RFID systems,” *Progress in Electromagnetics Research C*, vol. 31, pp. 109 - 121, 2012.

[31] Q. Brogan, T. O'Connor, and D. S. Ha, “Solar and thermal energy harvesting with a wearable jacket,” *IEEE International Symposium on Circuits and Systems (ISCAS)*, pp. 1412 - 1415, 2014.

[32] D. Patron, W. Mongan, T. P. Kurzweg, et al., “On the use of knitted antennas and inductively coupled RFID tags for wearable applications,” *IEEE transactions on biomedical circuits and systems*, vol. 10, no. 6, pp. 1047 - 1057, 2016.

[33] M. A. Yokus and J. S. Jur, “Fabric-based wearable dry electrodes for body surface biopotential recording,” *IEEE Transactions on Biomedical Engineering*, vol. 63, no. 2, pp. 423 - 430, 2016.

[34] D. Pani, A. Dessi, J. Saenz-Cogollo, et al., “Fully textile, PEDOT: PSS based electrodes for wearable ECG monitoring systems,” *IEEE Transactions on Biomedical Engineering* vol. 63, no. 3, pp. 540 - 549, 2016.

[35] D. Da He and C. G. Sodini, “A 58 nW ECG ASIC with motion-tolerant heartbeat timing extraction for wearable cardiovascular monitoring,” IEEE Transactions on Biomedical Circuits and Systems, vol. 9, no. 3, pp. 370 - 376, 2015.

[36] S. Izumi, K. Yamashita, M. Nakano, et al., “A wearable healthcare system with a 13.7 A noise tolerant ECG processor,” *IEEE Transactions on Biomedical Circuits and Systems*, vol. 9, no. 5, pp. 733 - 742, 2015.

[37] J. Ojarand, S. Pille, M. Min, et al. “Magnetic induction sensor for the respiration monitoring,” Proc. of 10th Int. Conf. on Bioelectromagnetism (icBEM), Tallinn, Estonia.: pp. 1 - 4, 2015.

[38] X. Zhang and Y. Lian, “A 300-mV 220-nW event-driven ADC with real-time QRS detection for wearable ECG sensors,” *IEEE Transactions on Biomedical Circuits and Systems*, vol. 8, no. 6, pp. 834 - 843, 2014.

[39] K. M. Thotahewa, J. Redoute, and M. R. Yuce, “A low-power wearable dual-band wireless body area network system: Development and experimental evaluation,” *IEEE Transactions on Microwave Theory and Techniques*, vol. 62, no. 11, pp. 2802 - 2811, 2014.

[40] C. Ieong, P. Mak, C. Lam, et al., “A 0.83-QRS detection processor using quadratic spline wavelet transform for wireless ECG acquisition in 0.35-CMOS,” IEEE Transactions on Biomedical Circuits and Systems, vol. 6, no. 6, pp. 586 - 595, 2012.

[41] E. Nemati, M. J. Deen, and T. Mondal, “A wireless wearable ECG sensor for long-term applications. *IEEE Communications Magazine*, vol. 50, no. 1, pp. 36 - 43, 2012.

[42] R. S. Dilmaghani, H. Bobarshad, M. Ghavami, et al., “Wireless sensor networks for monitoring physiological signals of multiple patients,” *IEEE Transactions on Biomedical Circuits and Systems*, vol. 5, no. 4, pp. 347 - 356, 2011.

[43] T. Vuorela, V. Seppa, J. Vanhala, et al., “Design, and implementation of a portable long-term physiological signal recorder,” *IEEE Transactions on Information Technology in Biomedicine*, vol. 14, no. 3, pp. 718 - 725, 2010.

[44] Z. Jin, J. Oresko, S. Huang, and A. C. Cheng, “HeartToGo: A personalized medicine technology for cardiovascular disease prevention and detection,” *Life Science Systems and Applications Workshop, LiSSA 2009, IEEE/NIH*, pp. 80 - 83, 2009.

[45] S. Chen, H. Lee, C. Chen, et al., “Wireless body sensor network with adaptive low-power design for biometrics and healthcare applications,” *IEEE Systems Journal*, vol. 3, no. 4, pp. 398 - 409, 2009.

[46] E. Monton, J. F. Hernandez, J. M. Blasco, et al., “Body area network for wireless patient monitoring,” *IET Communications*, vol. 2, no. 2, pp. 215 - 222, 2008.

[47] M. Di Rienzo, F. Rizzo, P. Meriggi, et al., “MagIC: A textile system for vital signs monitoring. advancement in design and embedded intelligence for daily life applications,” *29th Annual International Conference of the IEEE Engineering in Medicine and Biology Society*, pp. 3958 - 3961, 2007.

[48] T. Pawar, S. Chaudhuri, and S. P. Duttagupta, “Body movement activity recognition for ambulatory cardiac monitoring,” *IEEE Transactions on Biomedical Engineering*, vol. 54, no. 5, pp. 874 - 882, 2007.

[49] J. R. C. Chien and C. C. Tai, “A new wireless-type physiological signal measuring system using a PDA and the bluetooth technology,” *Biomedical Engineering: Applications, Basis and Communications*, vol. 17, no. 05, pp. 229 - 235, 2005.

[50] F. Knight, A. Schwirtz, F. Psomadelis, et al., “The design of the SensVest,” *Personal and Ubiquitous Computing*, vol. 9, no. 1, pp. 6 - 19, 2005.

[51] E. Jovanov, A. O. Lords, D. Raskovic, et al., “Stress monitoring using a distributed wireless intelligent sensor system,” *IEEE Engineering in Medicine and Biology Magazine*, vol. 22, no. 3, pp. 49 - 55, 2003.

[52] A. Sa-ngasoongsong and S. T. Bukkapatnam, “Wireless transmission of sensor signals for phonocardiology applications,” *IEEE Sensors 2010 Conference*, pp. 1975 - 1978, 2010.

[53] S. Mandal, L. Turicchia, and R. Sarpeshkar, “A low-power, battery-free tag for body sensor networks,” *IEEE Pervasive Computing*, vol. 9, no. 1, pp. 71 - 77, 2010.

[54] G. Lu, F. Yang, X. Jing, et al., “Contact-free measurement of heartbeat signal via a doppler radar using adaptive filtering,” *IEEE Image Analysis and Signal Processing (IASP)*, pp. 89 - 92, 2010.

[55] A. Lanata, E. P. Scilingo, and D. De Rossi, “A multimodal transducer for cardiopulmonary activity monitoring in emergency,” *IEEE Transactions on Information Technology in Biomedicine*, vol. 14, no. 3, pp. 817 - 825, 2010.

[56] Z. Popovic, P. Momenroodaki, and R. Scheeler, “Toward wearable wireless thermometers for internal body temperature measurements,” *IEEE Communications Magazine*, vol. 52, no. 10, pp. 118 - 125, 2014.

[57] Y. L. Zheng, X. R. Ding, C. C. Y. Poon, et al., “Unobtrusive sensing and wearable devices for health informatics,” *IEEE Transactions on Biomedical Engineering*, vol. 61, no. 5, pp. 1538 - 1554, 2014.

[58] S. Salman, Z. Wang, E. Colebeck, et al., “Pulmonary edema monitoring sensor with integrated body-area network for remote medical sensing,” *IEEE Transactions on Antennas and Propagation*, vol. 62, no. 5, pp. 2787 - 2794, 2014.

[59] D. Curone, E. L. Secco, A. Tognetti, et al., “Smart garments for emergency operators: The ProeTEX project. Information Technology in Biomedicine,” *IEEE Transactions on Information Technology in Biomedicine*, vol. 14, no. 3, pp. 694 - 701, 2010.

[60] S. Xiao, A. Dhamdhere, V. Sivaraman, et al., “Transmission power control in body area sensor networks for healthcare monitoring. Selected Areas in Communications,” *IEEE Journal on Selected Areas in Communications*, vol. 27, no. 1, pp. 37 - 48, 2009.

[61] E. I. Gaura, J. Brusey, J. Kemp, et al., “Increasing safety of bomb disposal missions: A body sensor network approach,” *IEEE Transactions on Systems, Man, and Cybernetics, Part C (Applications and Reviews)*, vol. 39, no. 6, pp. 621 - 636, 2009.

[62] J. Luprano, “European projects on smart fabrics, interactive textiles: Sharing opportunities and challenges,” *Workshop Wearable Technol. Intel. Textiles, Helsinki, Finland*, 2006.

[63] R. D. Labati, V. Piuri, R. Sassi, et al., “Adaptive ECG biometric recognition: A study on re-enrollment methods for QRS signals,” *IEEE International Symposium on Computational Intelligence in Biometrics and Identity Management (CIBIM)*, pp. 30 - 37, 2014.

[64] S. Safie, N. Haris, A. Zainal, et al., "Pulse active harmonic (PAH) features for ECG biometric authentication,” *IEEE First International Conference on Artificial Intelligence, Modelling & Simulation*, pp. 255 - 260, 2013.

[65] A. Kaul, A. Arora and S. Chauhan, “ECG based human authentication using synthetic ECG template,” *IEEE Signal Processing, Computing and Control (ISPCC)*, pp. 1 - 4, 2012.

[66] D. P. Coutinho, A. L. Fred and M. A. Figueiredo, “ECG-based continuous authentication system using adaptive string matching,” *Biosignals*, pp. 354 - 359, 2011.

[67] R. Abbasi-Kesbi, H. Memarzadeh-Tehran, and M. J. Deen, “Technique to estimate human reaction time based on visual perception,” *Healthcare Technology Letters*, vol. 4, no. 2, pp. 73 - 77, 2017.

[68] W. Y. Shi and J. -C. Chiao, “Neural network based real-time heart sound monitor using a wireless wearable wrist sensor,” *Springer, Analog Integrated Circuits and Signal Processing*, Volume 94, Issue 3, pp. 383 - 393, 2018.

[69] H. Motoyama, T. Inoue, and J. Ozawa, "Estimation of Wrist Angle Using EMG and Hand Movement Direction," *IEEE Consumer Electronics (ICCE)*, pp. 265 - 266, 2016.

[70] N. Friedman, J. B. Rowe, D. J. Reinkensmeyer, et al., “The manumeter: A wearable device for monitoring daily use of the wrist and fingers,” *IEEE journal of biomedical and health informatics*, vol. 18, no. 6, pp. 1804 - 1812, 2014.

[71] Y. J. An, G. H. Yun, S. W. Kim, et al., “Wrist pulse detection system based on changes in the near-field reflection coefficient of a resonator,” *IEEE Microwave and Wireless Components Letters*, vol. 24, no. 10, pp. 719 - 721, 2014.

[72] G. Pang and C. Ma. “A neo-reflective wrist pulse oximeter,” *IEEE access*, vol. 2, pp. 1562 - 1567, 2014.

[73] eZ430-Chronos™ Development Tool User's Guide, Texas Instruments, Inc., July 2015, datasheet, SLAU292G.

[74] D. G. Guo, F. E. H. Tay, L. Xu, et al., “Characterization and fabrication of novel micromachined electrode for BSN-based vital signs monitoring system.” *IEEE 6th International Conference on Wearable and Implantable Body Sensor Networks (BSN)*, pp. 125 - 130, 2009.

[75] A. Volmer and R. Orglmeister, “Wireless body sensor network for low-power motion-tolerant syncronized vital sign measurement,” *IEEE 30th Annual International Conference in Medicine and Biology Society*, pp. 3422 - 3425, 2008.

[76] W. Y.Chung, S. C.Lee, and S. H.Toh, “WSN based mobile u-healthcare system with ECG, blood pressure measurement function,” *IEEE 30th Annual International Conference in Medicine and Biology Society*, pp. 1533 - 1536, 2008.

[77] R. J. Buford, E. C. Green, and M. J. McClung. “A microwave frequency sensor for non-invasive blood-glucose measurement,” *IEEE Sensors Applications Symposium (SAS)*, pp. 4 - 7. 2008, .

[78] E. M. Tapia, S. S. Intille, L. Lopez, et al.. "The design of a portable kit of wireless sensors for naturalistic data collection," *Pervasive Computing*, pp. 117 - 134, 2006. .

[79] U. Anliker, J. A. Ward, P. Lukowicz, et al., “AMON: A wearable multiparameter medical monitoring and alert system,” *IEEE Transactions on information technology in Biomedicine*, vol. 8, no. 4, pp. 415 - 427, 2004.

[80] Z. Cohen, and S. Haxha, “Optical Based Sensor Prototype for Continuous Monitoring of the Blood Pressure,” *IEEE Sensors Journal*, vol. 17, no. 13, pp. 4258 - 4268, 2017.

[81] A. Joshi, S. Ravindran, and A. Miller, "EKG-Based Heart-Rate Monitor Implementation on the LaunchPad Using MSP430G2xx," *Application Report*, *Texas Instruments*, SLAA486A–March, 2011.

[82] Y. C. Wu, P. F. Chen, Z. H. Hu, et al., “A mobile health monitoring system using RFID ring-type pulse sensor,” *DASC'09*, *Eighth IEEE International Conference on Dependable, Autonomic and Secure Computing*, pp. 317 - 322, 2009.

[83] I.-H. Jang, H.-G. Yeom and K.-B. Sim, "Ring sensor and heart rate monitoring system for sensor network applications," IEEE Electronics Letters, vol. 44, no. 24, pp. 1393 - 1394, 2008.

[84] N. Oliver and F. Flores-Mangas, “HealthGear: A real-time wearable system for monitoring and analyzing physiological signals,” *IEEE International Workshop On Wearable and Implantable Body Sensor Networks*, *(BSN'06)*, pp. 1 - 4, 2006.

[85] V. Shnayder, B. Chen, K. Lorincz, et al., “Sensor networks for medical care,” *SenSys*. 2005.

[86] C. W. Mundt, K. N. Montgomery, U. E. Udoh, et al., “A multiparameter wearable physiologic monitoring system for space and terrestrial applications. Information Technology in Biomedicine,” *IEEE Transactions on Information Technology in Biomedicine*, vol. 9, no. 3 pp. 382 - 391, 2005.

[87] M. Borghetti, E. Sardini, and M. Serpelloni, “Sensorized glove for measuring hand finger flexion for rehabilitation purposes. Instrumentation and Measurement,” *IEEE Transactions on Instrumentation and Measurement* vol. 62, no. 12, pp. 3308 - 3314, 2013.

[88] K. Niazmand, K. Tonn, A. Kalaras, et al., “Quantitative evaluation of parkinson's disease using sensor based smart glove,” *IEEE International Symposium on Computer-Based Medical Systems*, pp. 1 - 8, 2011, .

[89] S. C. K. Lam, K. L. Wong, K. O. Wong, et al., “A smartphone-centric platform for personal health monitoring using wireless wearable biosensors,” *IEEE 7th International Conference on Information, Communications and Signal Processing*, pp. 1 - 7, 2009.

[90] L. K. Simone, N. Sundarrajan, X. Luo, et al., “A low cost instrumented glove for extended monitoring and functional hand assessment,” *Journal of neuroscience methods*, vol. 160, no. 2, pp. 335 - 348, 2007.

[91] F. Lorussi, E. P. Scilingo, M. Tesconi, et al., “Strain sensing fabric for hand posture and gesture monitoring,” *IEEE Transactions on Information Technology in Biomedicine*, vol. 9, no.. 3, pp. 372 - 381, 2005.

[92] A. Prochazka, M. Gauthier, M. Wieler, et al., “The bionic glove: An electrical stimulator garment that provides controlled grasp and hand opening in quadriplegia,” *Archives of physical medicine and rehabilitation*, vol. 78, no. 6, pp. 608 - 614, 1997.

[93] I. Jauregi, H. Solar, A. Beriain, et al, “UHF RFID temperature sensor assisted with body-heat dissipation energy harvesting,” *IEEE Sensors Journal*, vol. 17, no. 5, pp. 1471 - 1478, 2016.

[94] G. Matzeu, L. Florea, and D. Diamond, “Advances in wearable chemical sensor design for monitoring biological fluids,” *Sensors and Actuators B: Chemical*, vol. 211, pp. 403 - 418, 2015.

[95] T. Giorgino, P. Tormene, F. Lorussi, et al., “Sensor evaluation for wearable strain gauges in neurological rehabilitation,” *IEEE Transactions on Neural Systems and Rehabilitation Engineering*, vol.17, no. 4, pp. 409 - 415, 2009.

[96] H. Miwa, S. Sasahara, and T. Matsui, “Roll-over detection and sleep quality measurement using a wearable sensor,” *IEEE 29th Annual International Conference on Engineering in Medicine and Biology Society*, pp. 1507 - 1510, 2007, .

[97] W. J. Yi, S. Niu, T. Gonnot, et al., “System architecture of intelligent personal communication node for body sensor network,” IEEE Instrumentation and Measurement Technology Conference (I2MTC), pp. 1717 - 1720, 2013..

[98] L. Mo, S. Liu, R. X. Gao, et al., “Freedson. Wireless design of a multisensor system for physical activity monitoring,” *IEEE Transactions on Biomedical Engineering*, vol. 59, no. 11, pp. 3230 - 3237, 2012.

[99] L. M. Borges, A. Rente, F. J. Velez, et al., “Overview of progress in smart-clothing project for health monitoring and sport applications,” *IEEE First International Symposium on Applied Sciences on Biomedical and Communication Technologies*, pp. 1 - 6, 2008, .

[100] M. Akay, M. Sekine, T. Tamura, et al., “Unconstrained monitoring of body motion during walking,” *IEEE Engineering in Medicine and Biology Magazine*, vol. 22, no. 3, pp. 104 - 109, 2003.

[101] J. W. Matiko, Y. Wei, R. Torah, et al, “Wearable EEG headband using printed electrodes and powered by energy harvesting for emotion monitoring in ambient assisted living,” *Smart Materials and Structures*, vol. 24, no. 12, pp. 1 - 11, 2015.

[102] A. Gruebler and K. Suzuki. “Design of a wearable device for reading positive expressions from facial emg signals,” *IEEE Transactions on Affective Computing*, vol. 5, no. 3, pp. 227 - 237, 2014.

[103] C. T. Lin, C. H. Chuang, C. S. Huang, et al., “Wireless and wearable EEG system for evaluating driver vigilance,” *IEEE Transactions on biomedical circuits and systems*, vol. 8, no. 2, pp. 165 - 176, 2014.

[104] M. Duvinage, T. Castermans, M. Petieau, et al., “Performance of the emotiv epoc headset for P300-based applications,” *Biomedical engineering online*, vol. 12, no. 1, pp. 1 - 15, 2013.

[105] J. Kim, X. Huo, J. Minocha, et al., “Evaluation of a smartphone platform as a wireless interface between tongue drive system and electric-powered wheelchairs,” *IEEE transactions on biomedical engineering*, vol. 59, no. 6, pp. 1787 - 1796, 2012.

[106] R. Chávez-Santiago, K. E. Nolan, O. Holland, et al., “Cognitive radio for medical body area networks using ultra wideband. Wireless Communications,” *IEEE Wireless Communications*, vol. 19, no. 4, pp. 74 - 81, 2012.

[107] A. Riera, S. Dunne, I. Cester, et al., “Starfast: A wire-less wearable EEG/ECG biometric system based on the enobio sensor,” *International workshop on wearable micro and nanosystems for personalised health*, 2008.

[108] C. D. Katsis, G. Ganiatsas, and D. I. Fotiadis, “An integrated telemedicine platform for the assessment of affective physiological states,” *Diagnostic Pathology*, vol. 1, no. 1, pp. 1 - 9, 2006.

[109] T. Nakamura, V. Goverdovsky, M. J. Morrell, et al. “Automatic sleep monitoring using ear-EEG,” *IEEE Journal of Translational Engineering in Health and Medicine*, vol. 5, 2017.

[110] D. Da He, E. S. Winokur, and C. G. Sodini, “An ear-worn vital signs monitor,” *IEEE Transactions on Biomedical Engineering*, vol. 62, no. 11, pp. 2547 - 2552, 2015.

[111] D. Kollmann, W. K. Hogan, C. Steidl, et al., “VCSEL based, wearable, continuously monitoring pulse oximeter,” *IEEE 35th Annual International Conference on Engineering in Medicine and Biology Society (EMBC)*, pp. 4156 - 4159, 2013.

[112] K. Li and S. Warren, “A wireless reflectance pulse oximeter with digital baseline control for unfiltered photoplethysmograms,” *IEEE transactions on biomedical circuits and systems*, vol. 6, no. 3, pp. 269 - 278, 2012.

[113] J. A. C. Patterson, D. C. McIlwraith, and G. Z. Yang, “A flexible, low noise reflective PPG sensor platform for ear-worn heart rate monitoring. Presented at Wearable and Implantable Body Sensor Networks,” *IEEE Sixth International Workshop in Wearable and Implantable Body Sensor Networks*, pp. 286 - 291, 2009.

[114] O. Aziz, L. Atallah, B. Lo, et al., “A pervasive body sensor network for measuring postoperative recovery at home,” *Surgical innovation*, vol. 14, no. 2, pp. 83 - 90, 2007.

[115] A. Qusba, A. K. RamRakhyani, J. So, et al., “On the design of microfluidic implant coil for flexible telemetry system,” *IEEE Sensors Journal*, vol. 14, no. 4, pp. 1074 - 1080, 2014.

[116] Y. C. Huang, G. T. Yeh, T. S. Yang, et al., “A contact lens sensor system with a micro-capacitor for wireless intraocular pressure monitoring,” *IEEE in SENSORS*, pp. 1 - 4, 2013.

[117] H. W. Cheng, B. M. Jeng, C.Y. Chen, et al., “The rectenna design on contact lens for wireless powering of the active intraocular pressure monitoring system,” *IEEE 35th Annual International Conference at Engineering in Medicine and Biology Society*, pp. 3447 - 3450, 2013.

[118] Y. T. Liao, H. Yao, A. Lingley, et al., “A 3-μW glucose sensor for wireless contact-lens tear glucose monitoring,” *IEEE Journal Of Solid-State Circuits*, vol. 47, no. 1, pp. 335 - 344, 2012.

[119] Y. Miura, T. Hachida and M. Kimura, “Artificial retina using thin-film transistors driven by wireless power supply,” *IEEE Sensors Journal*, vol 11, no. 7, pp. 1564 - 1567, 2011.

[120] J. M. Fontana, M. Farooq, and E. Sazonov, “Automatic ingestion monitor: A novel wearable device for monitoring of ingestive behavior,” *IEEE Transactions on Biomedical Engineering*, vol. 61, no. 6, pp. 1772 - 1779, 2014.

[121] G. To and M. R. Mahfouz, “Quaternionic attitude estimation for robotic and human motion tracking using sequential monte carlo methods with von mises-fisher and nonuniform densities simulations,” *IEEE Transactions on Biomedical Engineering*, vol. 60, no. 11, pp. 3046 - 3059, 2013.

[122] D. Z. Stupar, J. S. Bajic, L. M. Manojlovic, et al., “Wearable low-cost system for human joint movements monitoring based on fiber-optic curvature sensor,” *IEEE Sensors Journal*, vol. 12, no.12, pp. 3424 - 3431, 2012.

[123] A. Milenković, C. Otto, and E. Jovanov, “Wireless sensor networks for personal health monitoring: Issues and an implementation,” *Computer communications*, vol. 29, no. 13, pp. 2521 - 2533, 2006.

[124] S. J. M. Bamberg, A. Y. Benbasat, D. M. Scarborough, et al., “Gait analysis using a shoe-integrated wireless sensor system,” *IEEE transactions on information technology in biomedicine*, vol. 12, no. 4 pp. 413 - 423, 2008.

[125] Y. Rimet, Y. Brusquet, D. Ronayette, et al., “Surveillance of infants at risk of apparent life threatening events (ALTE) with the BBA bootee: A wearable multiparameter monitor,” *IEEE 29th Annual International Conference at Engineering in Medicine and Biology Society*, pp. 4997 - 5000, 2007.

[126] A. Y. Benbasat, S. J. Morris, and J. A. Paradiso, “A wireless modular sensor architecture and its application in on-shoe gait analysis,” *IEEE Sensors*, vol. 2, pp. 1086 - 1091, 2003.

[127] Y. Chen, B. Lu, Y. Chen, et al., “Biocompatible and ultra-flexible inorganic strain sensors attached to skin for long-term vital signs monitoring,” *IEEE Electron Device Letters*, vol. 37, no. 4, pp. 496 - 499. 2016.

[128] P. Castillejo, J. Martinez, J. Rodríguez-Molina, et al., “Integration of wearable devices in a wireless sensor network for an E-health application,” *IEEE Wireless Communications*, vol. 20, no. 4, pp. 38 - 49, 2013.

[129] S. Lee and H. Yoo, “Low power and self-reconfigurable WBAN controller for continuous bio-signal monitoring system,” *IEEE transactions on biomedical circuits and systems*, vol. 7, no. 2, pp. 178 - 185, 2013.

[130] D. H. Kim, N. Lu, R. Ma, et al., “Epidermal electronics,” *Science*, vol. 333, no. 6044, pp. 838 - 843, 2011.

[131] S. Coyle, D. Morris, K. Lau, et al., “Textile-based wearable sensors for assisting sports performance,” *IEEE Sixth International Workshop Wearable and Implantable Body Sensor Networks*, pp. 307 - 311, 2009.

[132] R. G. Haahr, S. Duun, E. V. Thomsen, et al., “A wearable “electronic patch” for wireless continuous monitoring of chronically diseased patients,” *IEEE 5th International Summer School and Symposium on Medical Devices and Biosensors*, pp. 66 - 70, 2008.

[133] A. B. Dolgov and R. Zane, “Low-power wireless medical sensor platform,” *IEEE 28th Annual International Conference on Engineering in Medicine and Biology Society*, pp. 2067 - 2070, 2006.

[134] R. Farra, N. F. Sheppard Jr, L. McCabe, et al., “First-in-human testing of a wirelessly controlled drug delivery microchip,” *Science translational medicine*, vol. 4, no. 122, 2012.

[135] M. M. Ahmadi and G. A. Jullien, “A wireless-implantable microsystem for continuous blood glucose monitoring,” *IEEE Transactions on Biomedical Circuits and Systems*, vol. 3, no. 3, pp. 169 - 180, 2009.

[136] J. Wang and K. D. Wise, “A hybrid electrode array with built-in position sensors for an implantable MEMS-based cochlear prosthesis,” *Journal of Microelectromechanical systems*, vol. 17, no. 5, pp. 1187 - 1194, 2008.

[137] E. J. Gómez, M. H. Pérez, T. Vering, et al., “The INCA system: A further step towards a telemedical artificial pancreas,” *IEEE Transactions on Information Technology in Biomedicine*, vol. 12, no. 4, pp. 470 - 479, 2008.

[138] A. D. DeHennis and K. D. Wise, "A fully integrated multisite pressure sensor for wireless arterial flow characterization," IEEE Journal of Microelectromechanical Systems, vol. 15, no. 3, pp. 678 - 685, 2006.

[139] P. Valdastri, A. Menciassi, A. Arena, et al., “An implantable telemetry platform system for in vivo monitoring of physiological parameters,” *IEEE Transactions on Information Technology in Biomedicine*, vol. 8, no. 3, pp. 271 - 278, 2004.

[140] D. G. Adler and C. J. Gostout, “Wireless capsule endoscopy,” *Hospital Physician*, vol. 39, no. 5, pp. 14 - 22, 2003.

[141] A. Poscia, M. Mascini, D. Moscone, et al., “A microdialysis technique for continuous subcutaneous glucose monitoring in diabetic patients (part 1),” *Biosensors and bioelectronics*, vol. 18\, no. 7, pp. 891 - 898, 2003.

[142] R. D. Beach and F. Moussy, “Totally implantable real-time in vivo video telemetry monitoring system for implant biocompatibility studies,” *IEEE Transactions on Instrumentation and Measurement*, vol. 50, no. 3, pp. 716 - 723, 2001.

[143] J. T. Santini, M. J. Cima, and R. Langer, “A controlled-release microchip,” *Nature,* vol. 397, no. 6717, pp. 335 - 338. 1999.

[144] E. E. Coris, A. M. Ramirez , and D. J. Van Durme, “Heat illness in athletes,” *Sports Medicine*, vol. 34, no.1, pp.9 - 16, 2004

[145] X. Huang, W. H. Yeo, Y. Liu, *et al*., “Epidermal Differential Impedance Sensor for Conformal Skin Hydration Monitoring,” *Biointerphases*, vol. 7, no. 52, pp.1 - 20, 2012.

[146] M. Puentes, M. Maasch, M. Schubler, and J. Rolf, “Frequency Multiplexed 2-dimensional Sensor Array Based on Split-ring Resonators for Organic Tissue Analysis,” *IEEE Transactions on Microwave Theory and Techniques*, vol. 60, no. 6, pp. 1720 - 1727, 2012.

[147] S. R. Mohd Shah, J. Velander, P. Mathur, *et al.*, “Split-Ring Resonator Sensor Penetration Depth Assessment Using In Vivo Microwave Reflectivity and Ultrasound Measurements for Lower Extremity Trauma Rehabilitation,” *Sensors*, vol.18, no.2-636, pp.1 - 11, 2018.

[148] C. M. Boutry, H. Chandrahalim, P. Streit, *et al.*, “Characterization of Miniaturized RLC Resonators Made of Biodegradable Materials for Wireless Implant Applications,” *Sensors and Actuators A: Physical*, vol. 189, pp. 344 - 355, 2013.

[149] N. Miura, S. Shioya, D. Kurita, et al., “Time domain reflectometry: measurement of free water in normal lung and pulmonary edema,” *American Journal of Physiology-Lung Cellular and Molecular Physiology*, vol. 276, no.1, pp. L207-L212, 1999.

[150] S. Mashimo, N. Miura, and T. Umehara, ‘The structure of water determined by microwave dielectric study on water mixtures with glucose, polysaccharides, and L-ascorbic acid,” *The Journal of chemical physics*, vol. 97, no. 9, pp. 6759 - 6765, 1992.

[151] D. Kurup, W. Joseph, G. Vermeeren, *et al.*, “In-body Path Loss Model for Homogeneous Human Muscle, Brain, Fat and Skin,” *Antennas and Propagation (EuCAP), Proceedings of the Fourth European Conference on IEEE*, pp. 1 - 4, 2010.

[152] C. Reimann, M. Puentes, M. Maasch, *et al.*, “Planar Microwave Sensor for Theranostic Therapy of Organic Tissue Based on Oval Split Ring Resonators,” *Sensors*, vol. 16, no. 9-1450, pp. 1 - 13, 2016.

[153] H. Choi, J. Naylon, S. Luzio, et al., "Design and In Vitro Interference Test of Microwave Noninvasive Blood Glucose Monitoring Sensor," *IEEE Transactions on Microwave Theory and Techniques*, vol. 63, no.10, pp. 3016 - 3025, 2015.

[154] G. Ekinci, A. Calikoglu, S. N. Solak, et al., "Split-ring resonator-based sensors on flexible substrates for glaucoma monitoring," *Sensors and Actuators A: Physical*, vol. 268, pp. 32 - 37, 2017.

[155] M. Abidi, A. Elhawil, J. Stiens, R. Vounchx, J. Tahar, and F. Choubani, “Sensing liquid properties using split-ring resonator in mm-wave band,” *IECON 2010-36th Annual Conference on IEEE Industrial Electronics Society,* pp. 1298 - 1301, 2010.

[156] H. Torun, F. C. Top, G. Dundar, et al., “A split-ring resonator-based microwave sensor for biosensing,” *Optical MEMS and Nanophotonics (OMN), 2014 International Conference on. IEEE*, pp. 159 - 160, 2014.

[157] M. Mueh, C. Damm, “Spurious Material Detection on Functionalized Thin-Film Sensors using Multiresonant Split-Rings,” *2018 IEEE International Microwave Biomedical Conference (IMBioC)*, pp. 196 - 198, 2018.

[158] S. Gabriel, R. W. Lau, and C. Gabriel, “The Dielectric Properties of Biological Tissues: II. Measurements in the Frequency Range 10 Hz to 20 *GHz*,” *Physics in medicine & biology*, vol. 41, no. 11, pp. 2251 - 2269, 1996.

[159] R. Pethig, “Dielectric Properties of Body Tissues,” *Clinical Physics and Physiological Measurement*, vol.8, suppl. 4A, pp. 5 - 12, 1987.

[160] F. T. Ulaby, E. Michielssen, and U.Ravaioli, *Fundamentals of Applied Electromagnetics* 6e. Prentice Hall, 2001.

[161] S. Zuffanelli, G. Zamora, P. Aguilà, et al., “On the radiation properties of split-ring resonators (SRRs) at the second resonance,” *IEEE Transactions on Microwave Theory and Techniques*, vol. 63, no. 7, pp. 2133 - 2141, 2015.

[162] L. H. Hsieh and K.Chang, "Equivalent lumped elements G, L, C, and unloaded Q's of closed- and open-loop ring resonators," *IEEE Transactions on Microwave Theory and Techniques*, vol. 50, no. 2, pp. 453 - 460, 2002.

[163] K. Chang, S. Martin, F. Wang, et al., “On the study of microstrip ring and varactor-tuned ring circuits,” *IEEE Transactions on Microwave Theory and Techniques*, vol. 35, no. 12, pp. 1288 - 1295, 1987.

[164] J. D. Baena, J. Bonache, F. Martin, *et al.*, “Equivalent-circuit Models for Split-ring Resonators and Complementary Split-ring Resonators Coupled to Planar Transmission Lines,” *IEEE transactions on microwave theory and techniques*, vol. 53, no. 4, pp. 1451 - 1461, 2005.

[165] J. Naqui, M . Durán-Sindreu, and F. Martín, “Modeling split-ring resonator (SRR) and complementary split-ring resonator (CSRR) loaded transmission lines exhibiting cross-polarization effects,” *IEEE Antennas and Wireless Propagation Letters*, vol. 12, pp. 178 - 181, 2013.

[166] D. Barrick, “Miniloop antenna operation and equivalent circuit,” *IEEE transactions on antennas and propagation*, vol.34, no.1, 111 - 114, 1986.

[167] O. Sydoruk, E. Tatartschuk, E. Shamonina, and L. Solymar, “Analytical formulation for the resonant frequency of split rings,” *Journal of applied physics*, vol. 105, no. 1, pp. 014903-1 – 014903-4, 2009.

[168] K. Ito, M. Takahashi, and K. Saito, "Small antennas used in the vicinity of human body," *IEICE Transactions on Communications*, vol.99, no.1, pp. 9 - 18, 2016.

[169] J. Krupka, K. Derzakowski, B. Riddle, and J. Baker-Jarvis, “A dielectric resonator for measurements of complex permittivity of low loss dielectric materials as a function of temperature,” *Measurement Science and Technology*, vol. 9, no. 10, pp. 1751 - 1756, 1998.

[170] S. O. Nelson, and P. G. Bartley, “Measuring frequency-and temperature-dependent permittivities of food materials,” *IEEE transactions on instrumentation and measurement*, vol. 51, no. 4, pp. 589 - 592, 2002.

[171] K. Berdel, J. G. Rivas, P. H. Bolívar, P. De Maagt, and H. Kurz, “Temperature dependence of the permittivity and loss tangent of high-permittivity materials at terahertz frequencies,” *IEEE transactions on microwave theory and techniques*, vol. 53, no. 4, pp. 1266 - 1271, 2005.

[172] S. Trabelsi, “Frequency and temperature dependence of dielectric properties of chicken meat,” *2012 IEEE International Instrumentation and Measurement Technology Conference Proceedings*, pp. 1515 - 1518. 2012.

[173] M. M. Stecker, “A review of intraoperative monitoring for spinal surgery,” *Surgical neurology international*, vol 3, no. Suppl 3, pp. S174 - S187, 2012.

[174] M. Sutter, A. Eggspuehler, D. Grob, D. Jeszenszky, A. Benini, F. Porchet, A. Mueller, and J. Dvorak, “The diagnostic value of multimodal intraoperative monitoring (MIOM) during spine surgery: a prospective study of 1,017 patients,” *European Spine Journal*, vo. 16, no.2, pp. 162 - 170, 2007.

[175] A. D. Legatt, R. G. Emerson, C. M. Epstein, D. B. MacDonald, V. Deletis, R. J. Bravo, and J. R. López, “ACNS guideline: transcranial electrical stimulation motor evoked potential monitoring,” *Journal of Clinical Neurophysiology*, vol. 33, no. 1, pp. 42 - 50, 2016.

[176] S. Tsutsui and H. Yamada, “Basic principles and recent trends of transcranial motor evoked potentials in intraoperative neurophysiologic monitoring,” *Neurologia medico-chirurgica*, vol. 56, no. 8, pp. 451 - 456, 2016.

[177] D. Burke, R. Hicks, J. Stephen, I. Woodforth, and M. Crawford, “Assessment of corticospinal and somatosensoty conduction simultaneously during scoliosis surgery,” *Electroencephalography and Clinical Neurophysiology/Evoked Potentials Section*, vol. 85, no. 6, pp. 388 - 396, 1992.

[178] V. Deletis, V. Isgum, and VE. Amassian, “Neurophysiological mechanisms underlying motor evoked potentials in anesthetized humans. Part 1. Recovery time of corticospinal tract direct

waves elicited by pairs of transcranial electrical stimuli," *Clinical neurophysiology*, vol. 112, no. 3, pp. 438 - 444, 2001.

[179] J. Mays, P. Rampy, D. Sucato, S. Sparagana, and J. -C. Chiao, "A WBAN system improves reliability of intraoperative monitoring recordings," *IEEE Topical Conference on Biomedical WBAN Technologies, Networks, and Sensing Systems (BioWBAN)*, pp. 5 - 7, 2016.

[180] J. Mays, P. Rampy, D. Sucato, S. Sparagana, and J. -C. Chiao, "A WBAN solution for intraoperative monitoring," *International Microwave Workshop Series on RF and WBAN Technologies for Biomedical and Healthcare Applications (IMWS-BIO)*, pp. 244 - 245, 2015.

[181] J. M. Tjensvold, "Comparison of the IEEE 802.11, 802.15. 1, 802.15. 4 and 802.15. 6 WBAN standards," *in IEEE*, September, vol. 18, pp. 1 - 7, 2007.

[182] K. S. Kwak, S. Ullah and N. Ullah, "An overview of IEEE 802.15. 6 standard," *Applied Sciences in Biomedical and Communication Technologies (ISABEL), 3rd International Symposium*, pp.1 - 6, 2010.

[183] C. C. Poon, B. P. Lo, M. R. Yuce, et al., "Body sensor networks: In the era of big data and beyond. Biomedical Engineering," *IEEE reviews in biomedical engineering*, vol. 8, pp. 4 - 16, 2015.

[184] M. Chan, D. EstèVe, J. Y. Fourniols, C. Escriba, and E. Campo, "Smart wearable systems: Current status and future challenges," *Artificial intelligence in medicine*, vol. 56, no. 3, pp. 137 - 156, 2012.

[185] S.C. Mukhopadhyay, "Wearable sensors for human activity monitoring: A review," *IEEE sensors journal*, vol. 15, no. 3, pp.1321 - 1330, 2015.

[186] X. Teng, Y. Zhang, C. C. Poon, et al., "Wearable medical systems for p-health," *IEEE reviews in Biomedical engineering*, vol. 1, pp. 62 - 74. 2008.

[187] E. Monton, J. F. Hernandez, J. M. Blasco, et al., "Body area network for WBAN patient monitoring," *IET Communications*, vol. 2, no. 2, pp. 215 - 222, 2008.

[188] W. K. Chen, The circuits and filters handbook. *CRC Press*, 2009.

[189] H. Garnier, M. Mensler, and A. Richard. “Continuous-time Model Identification From Sampled Data: Implementation Issues and Performance Evaluation.” *International Journal of Control*, vol. 76, Issue 13, pp. 1337 - 1357, 2003.

[190] L. Ljung, “Experiments With Identification of Continuous-Time Models.” *Proceedings of the 15th IFAC Symposium on System Identification*, vol, 42, no. 10, pp. 1175 - 1180, 2009.

[191] J. B. Kruskal, “Multidimensional scaling by optimizing goodness of fit to a nonmetric hypothesis,” *Psychometrika*, vol. 29, no. 1, pp.1 - 27, 1964.

[192] S. M. Stigler, “Francis Galton's account of the invention of correlation,” *Statistical Science*, vol. 4, no. 2, pp. 73 - 79, 1989.

[193] R. J. Hyndman, and A. B. Koehler, “Another look at measures of forecast accuracy,” *International journal of forecasting*, vol. 22, no. 4, pp. 679 - 688, 2006.